Computational Aeroacoustic Investigation of Co-rotating rotors for Urban Air Mobility

MSc Thesis

Shubham

Technische Universiteit Delft

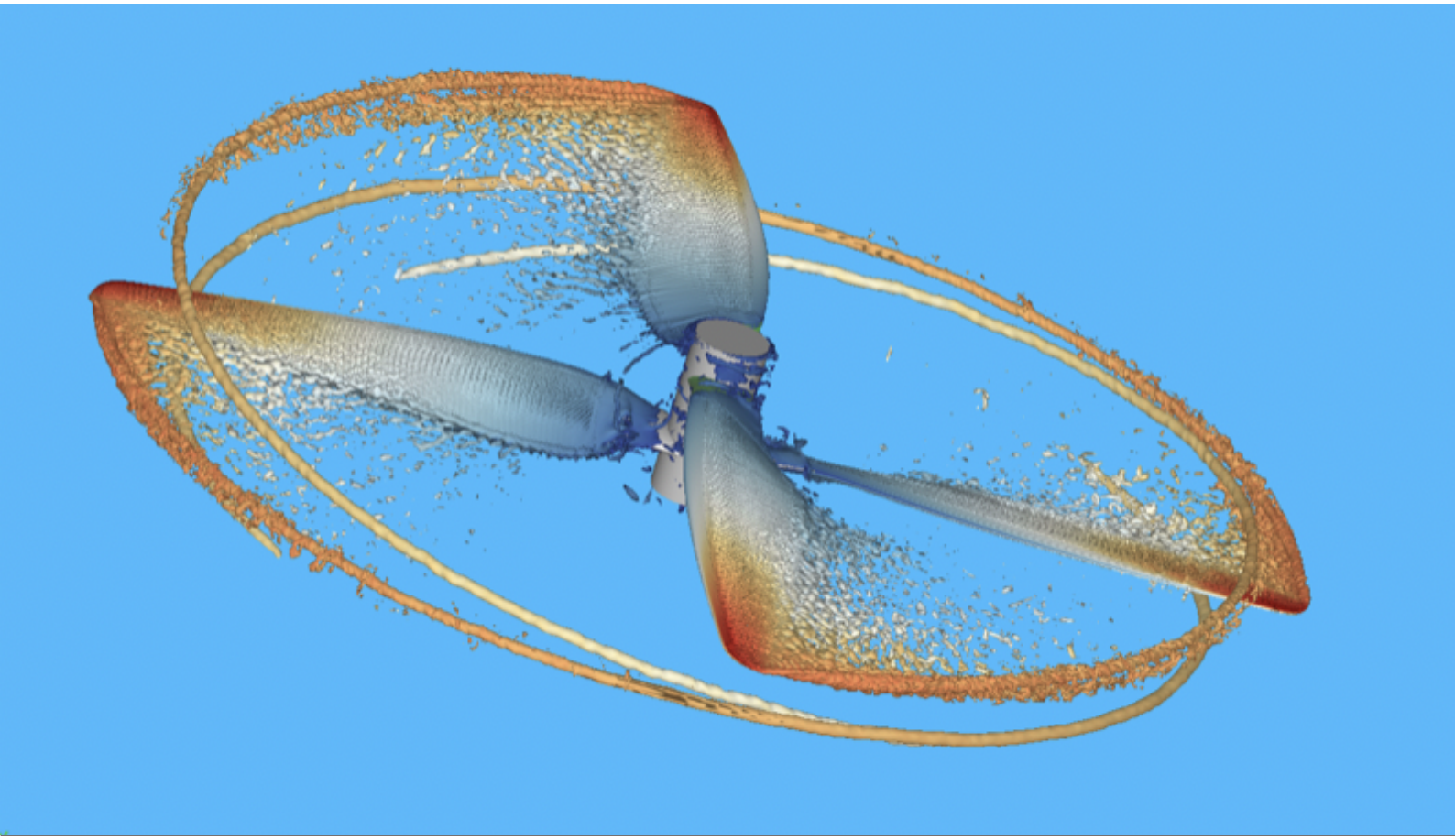

TU Delft Delft University of Technology

Challenge the future

Computational Aeroacoustic Investigation of Co-rotating rotors for Urban Air Mobility

by

Shubham

to obtain the degree of
Master of Science in Aerospace Engineering
at the Delft University of Technology,
to be defended publicly on Friday January 31st, 2020.

Student number:	4723104	
Project duration:	April 16th, 2019 – Jan 31st, 2020	
Research Group:	Aeroacoustics Group, Wind Energy Track	
Thesis committee:	Dr. F. Avallone,	TU Delft, supervisor
	E. Grande,	TU Delft, supervisor
	Prof. dr. D. Casalino,	TU Delft, chair
	Dr. T. Sinnige,	TU Delft

An electronic version of this thesis is available at `http://repository.tudelft.nl/`.

TU Delft

Summary

Rotor noise is one of the major issues that limits the applicability of an air vehicle in an urban environment. With the advent of *Urban Air Mobility* and its requirement for a quieter aircraft with higher efficiency (due to current problems with batteries), the need to optimize the rotor for aerodynamics and aeroacoustics has become even more important. The unconventional configurations, such as *co-rotating rotor*, is one of the alternatives that offer such potential and in this study, a computational investigation has been performed to understand the flow physics of such rotors.

The previous studies by various authors showed the lack of knowledge on fundamental flow physics of co-rotating rotors, which has been limiting its development and applicability to various domains. As a result, research objectives were formulated and Dassault Systèmes PowerFLOW was employed for computational simulations, which uses Lattice Boltzmann-Very Large Eddy Simulation (LB-VLES) approach for flow field calculations and Ffowcs-Williams and Hawkings (FWH) analogy for far-field aeroacoustic post-processing. The study was divided into 3 different phases - *Grid Resolution*, *Flow Physics*, and *Quantification and Baseline* study.

In the *grid resolution study*, the configuration with 84^o azimuthal and 1.1 in (2.79 cm) axial separation was studied for different resolutions to check mesh convergence. A final resolution was then decided for further phases. The *flow physics study* comprised running two new configurations - change of azimuthal separation to 12^o and change of axial separation to 1.3 in (3.30 cm). Results were also validated against published experimental results. Three major flow phenomena were found: *Inflow*, *Circulation* and *Blade-Vortex Interaction (BVI)* effect. While the first two effects are potential effects, *BVI* is due to the finite length of rotor blades, similar to an aircraft wing.

Inflow effect is the result of mutual interaction of streamtubes of both rotors. *Circulation effect* takes place in case of close vicinity of lower blade to the upper blade and acts similar to a flap for the latter. *BVI* is caused by the interaction between rotor blades and the tip vortices produced from each blade, which adversely affects the spanwise angle of attack distribution on the blade. The results show that *thrust* decreases by 4.25 % as azimuthal separation decreases by 72^o, while thrust increases by just 0.73 % when axial separation increases by 18.18%. A combination of all the above-mentioned phenomena is responsible for this behaviour.

In terms of far-field *noise*, increasing azimuthal separation decreases noise which is mainly caused due to destructive interference of pressure signal between the upper and lower rotor. Maximum reduction in noise achieved is 14 dB at the rotor plane, for a separation increase of 72^o. On the other hand, increasing axial separation increases noise due to increase in loading noise from the thrust produced. Noise increases by 1 dB at the rotor place for a thrust increase of 0.73 %. A comparison between co-rotating rotor with 12^o azimuthal separation and a 2-bladed isolated rotor, both producing the same thrust, reveals that latter has lower noise by 2 dB at the rotor plane. This is attributed to lower phase angle difference between the upper and lower blades of the former. This also suggests that, for lower noise, higher azimuthal separation is beneficial.

In the *quantification study phase*, all the flow phenomena in a co-rotating rotor were quantified by comparing the thrust value of each rotor to an isolated 2-bladed rotor. The values suggest that *BVI* is the most important of all phenomena which is responsible for adverse performance of the rotor as compared to a baseline rotor. In case of low azimuthal separation, *inflow effect* plays a big role too. The findings also suggest that the *circulation effect* can offer great potential in improving the co-rotating rotor performance to better than all other configurations.

Acknowledgements

If I rewind the clock 2 years back, I remember myself coming to a new country (Netherlands) with big hopes and aspirations of learning about a new subject (aerospace engineering) and experiencing a whole different culture. Today, I can definitely say that this journey encompasses the most fruitful years of my life, both in professional and personal scenarios, filled with all types of emotions and successfully passing through some of the biggest challenges I faced in my life. The journey was made possible by a number of people without whom it would have been very difficult to reach the stage I am currently standing at.

First of all, I would like to thank all of my friends who have been with me through every stage of the journey. A special thanks to the *Aerodynamics Boys - Athreya, Sid, Nikhilesh, Kushal, Jatinder, Chakshu, Abhinand, Nikhil, Sampath, Prayash, Siddhant, Ankith, Umberto, Gerardo* and *Achilleas*. You guys have been just amazing. The time spent during the master courses, assignments, thesis, the long discussions we had about any topic either be it technical or non-technical, weekend meet-up for playing games, etc. Friends from other master track - *Shrutika, Ashvij, Rajath, Abhas, Rajarshi, Snigdha, Abhishek*; friends from other faculties - *Gayatri, Surbhi, Bhavya* and *Shubhonil*; all you guys have been part of my family away from home and made my Delft journey more exciting and something to cherish.

My friends in Braunschweig and Munich - *Cylia, Ngoc, Karna, Claudia, Olha* and *Alena*; the life in Germany during internships became more enjoyable because of all of you and helped me forget the wrath of German bureaucracy! For the DLR internship, I would like to thank *Gunther Wilke* and *Philipp Kunze* for giving me the opportunity to work at one of the best places for aerodynamics research. For the GE Aviation internship, *Paolo Vanacore* gave me an opportunity to experience the corporate culture in an aerospace company, which would be really helpful in the coming future.

At TU Delft, I would like to first mention *Leo Veldhuis* and *Carlos Simao Ferreira* because of whom I developed interest in propeller aerodynamics and aeroacoustics and then decided to take up master thesis in the same topic. For my current master thesis study, I would like to thank *Damiano Casalino* and *Francesco Avallone* for giving me an amazing opportunity to explore the world of propellers, especially applied to Urban Air Mobility vehicles. The past 9 months have been one of the most intense months, in terms of technical learning and personal development. It has helped me to decide the journey I wish to follow in the future. Furthermore, thanks to *APC Propellers* for providing the propeller geometry and *Charles Tinney* for providing the experimental results for validation. A special thanks to *Edoardo Grande* for bearing with me all these months, and helping me out with PowerFLOW and other technical difficulties. I hope you will perform some experiments on co-rotating rotors and we can publish some good articles in the future!

Back in India, I would like to thank my friends who did not break the friendship even though I did not meet them for more than 2 years - *Raushan, Sudarshan, Ravi, Shubham Singh, Dontu, Vivek, Sumit, Anurag, Arnob, Rishabh, Navneet, Sudhanshu, Neha, Oshin, Aparna, Priyansha*

Finally, I would like to thank my *parents* for providing me an emotional and financial support during the whole journey, without whom I would not have even thought about starting the journey. I really hope that your contribution and faith in me will prove to be worth in the future.

Thank you everyone! Bedankt! Grazie a tutti! Vielen Dank!

Shubham
Delft, January 2020

Contents

List of Figures

List of Tables

List of Abbreviations

AoA	Angle of Attack
AR	Aspect Ratio
BC	Boundary Condition
BEMT	Blade Element Momentum Theory
BPF	Blade Passage Frequency
CAA	Computational Aeroacoustics
CAD	Computer Aided Design
CFD	Computational Fluid Dynamics
CS	Constant Speed
FFT	Fast-Fourier Transform
FOM	Figure Of Merit
FWH	Ffowcs-Williams and Hawkings
LBM	Lattice Boltzmann Methods
MATLAB	MATrix LABoratory
NASA	National Aeronautics and Space Administration
OASPL	OverAll Sound Pressure Level
PAV	Personal Air Vehicles
RAF	Relative Air Flow
Re	Reynolds number
RPM	Rotations Per Minute
rps	rotations per second
SPL	Sound Pressure Level
UAM	Urban Air Mobility
UAV	Unmanned Air Vehicles
UK	United Kingdom
USA	United States of America
VLES	Very Large Eddy Simulation
VP	Variable Pitch
VR	Variable Resolution region
VTOL	Vertical TakeOff and Landing

List of Symbols

Latin lower case

Symbol	Unit	Description
c	m/sec	Speed of sound
n	Hz	Rotations per second
p'	Pa	Pressure perturbations
r	m	Radial location
r_min	m	Relative minimum radius of trip
r_max	m	Relative maximum radius of trip
rH	m	Radius of hub
rT	m	Radius of blade tip
t	sec	Time
u_0	m/sec	Forward flight velocity
v	m/sec	Velocity vector
w	[-]	Particle collision weights
y	m	Distance from the wall
y^+	[-]	Dimensionless wall distance

Latin upper case

Symbol	Unit	Description
A	m^2	Propeller swept area
C_P	[-]	Power coefficient
C_Q	[-]	Torque coefficient
C_T	[-]	Thrust coefficient
D	m	Propeller/Rotor diameter
J	[-]	Advance ratio
M_r	[-]	Relative Mach number
N	[-]	Total number of voxels in a particular VR region
P	Pa	RMS of pressure perturbations
P_{in}	Watt	Input power
P_{ref}	Pa	Reference pressure level
Q	Nm	Torque

R	m	Propeller/Rotor radius
T	N	Thrust
T_{ij}	N/m^2	Lighthill's stress tensor
T_p	sec	Rotor rotation period

Greek symbols

Symbol	**Unit**	**Description**
ρ	kg/m^3	Fluid density
ρ'	kg/m^3	Density perturbations
ω	Hz	Rotations per second
η	[-]	Propeller efficiency
$\Delta\phi$	^{o}	Azimuthal separation
Δz	m	Axial separation
λ	m	Wavelength of trip
λ_2	1/sec^2	Isosurface criterion
α	^{o}	Angle of Attack
σ	[-]	Rotor solidity
Γ	m^2/sec	Circulation around a vortex

1 Introduction

1.1. Background

In the past two decades, one of the most significant changes in the aerospace industry is the emerging markets for Unmanned Air Vehicles (UAV) and Personal Air Vehicles (PAV) (Figure 1.1). They are poised to be a game-changer for various applications such as civil (healthcare, mining, agriculture, etc), military (reconnaissance, training, etc) and research purposes (oceanology, atmospheric studies, etc). A new application is Urban Air Mobility (UAM) where PAVs in the form air taxis will be operating in an urban environment, changing urban transportation and mobility experience. Since such vehicles will be an all-electric aircraft and operate in an urban environment, it involves the propulsion system to be more efficient and have low noise signature. Thus, a combined study of aerodynamics and aeroacoustics has become imperative in such contexts.

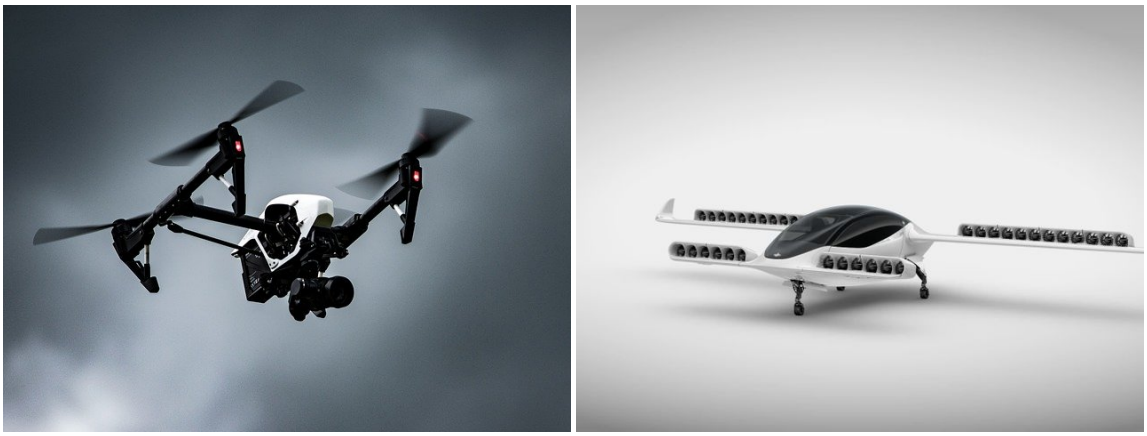

(a) Unmanned Air Vehicle (b) Personal Air Vehicle

Figure 1.1: Example for UAV and PAV
Source: DJI and Lilium

Rotors have always been a preferred choice for UAVs due to their simplistic and reliable design (apart from being more efficient) as compared to a turbofan or turbojet. Additionally, it provides a seamless transition between hover and forward flight, providing the vehicle with more manoeuvrability. Therefore, it naturally becomes the preferred choice of propulsion system to harness electric power in case of a PAV. Rotors (either open or ducted) can exist in various configurations such as co-axial, co-planar, tandem, etc. wherein co-rotating and contra-rotating are two types of co-axial

rotors. Each configuration is suited to specific applications and requirements from customers, for example, a rotor designed for heavy lift helicopters will be different from a rotor designed for small UAVs. Although, designing a complete rotor system follows a multi-disciplinary design process (*fluids, structures, controls*, etc.), in this study we will be focusing only on aerodynamic and aeroacoustic analyses.

Co-rotating rotor is an unconventional co-axial rotor design in which both the upper and lower rotors, connected through the same shaft, rotate in the same direction. According to Mahendra [5], such rotor offers more design flexibility and has higher efficiency when specific co-rotating configurations are compared to its contra-rotating or co-planar counterpart. One of the main challenges is to reduce noise without affecting the aerodynamic performance and thus, the co-rotating configuration has the potential to fulfil such requirements with limited changes to rotor geometry and power distribution of the vehicle. During the present study, major focus is given on understanding the performance of co-rotating rotors, analyzing various flow parameters, and performing critical analyses of each of the results. The motivation is to understand the effect of each design parameter on rotor aerodynamics and aeroacoustics and propose a new design which will have improved characteristics.

1.2. Problem Statement

In the history of rotor development, the co-rotating configuration has not been explored in greater detail, as compared to contra-rotating or co-planar configurations. When multicopters started coming into use in greater numbers, the focus shifted towards optimizing the rotor configuration for higher efficiency and lower noise. This inspired the present study on co-rotating rotor to understand the flow physics and explore the possibility of reducing aerodynamic noise without adversely affecting (or if possible, increasing) its efficiency.

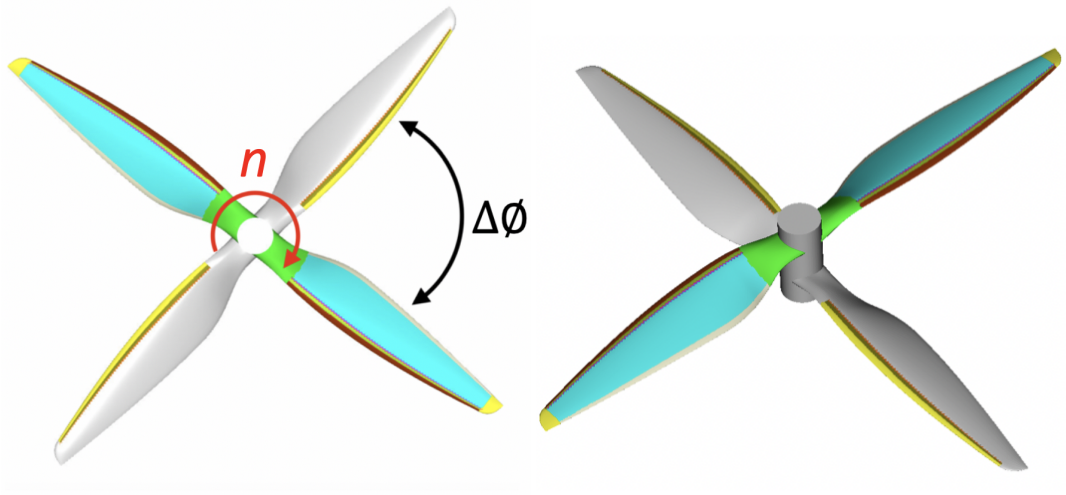

(a) Top view

(b) Orthogonal view; Δz is the axial separation between rotors

Figure 1.2: Co-rotating rotor geometry

Figure 1.2 shows the geometry of co-rotating rotor rotating at *n rotations per second (rps)*, where the two rotors are separated by an *azimuthal separation* $\Delta\phi$ and an *axial separation* Δz, both of which are variable parameters. The aim of the present study was to vary these geometrical parameters (amongst others) and study the effects of these parameters on the performance of the rotor. A major objective was to establish relations between these parameters and performance values ob-

tained so that the same result can be used to predict performance for other configurations. The effects of mesh resolution was also studied to decide the best computational setup for all the simulations. Another aim was to compare the co-rotating rotor with an isolated rotor configuration so as to quantify the flow phenomena taking place for the former. The final goal of the study was to propose a new configuration based on all the previous analyses, that can have potential aerodynamic and aeroacoustic improvements over all the previous configurations.

Chapter 3 presents the research objectives and the thesis plan in greater detail.

1.3. Approach

For solving any physical problem, there can be 3 different approaches:

- **Analytical**: The mathematical equations related to the problem are solved by applying appropriate physical conditions (such as initial and boundary conditions, etc.) and an exact solution is obtained. Such solutions are limited to simplified geometry and equations can be solved only after certain assumptions are taken. This limits the applicability of the approach and thus, requires other methods to solve a physical problem.

- **Experimental**: The physical setup for the problem is manufactured, either as a scaled down or full scale version. Then the experimental test is done either in a wind tunnel or in real flight environment. The advantage of this approach is that the values of physical parameters are obtained in a real test scenario, so it naturally makes an engineer trust the data obtained (except for experimental uncertainty and measurement noise present). The disadvantage is that manufacturing either scaled down or full scale models are expensive, so testing multiple configurations of the geometry increases the cost of the project.

- **Computational**: In this approach, initially a CAD model is prepared for the geometry around which the flow needs to be investigated. The model is discretized into grids containing numerous surface and volume elements. The mathematical equations pertaining to the physical problem are also discretized (using a numerical method of choice) and the obtained matrix is solved in the discretized domain. The values are obtained only at the mesh points and are interpolated at other points. Since the domain is discretized, the values obtained depend on the type of mesh used, number of mesh elements, numerical methods employed, etc., and not only on the physics of the problem. This is a disadvantage of this approach and a grid convergence study is imperative in every case. The advantage is that running simulations on a computer for multiple geometries is much cheaper (especially regarding money), as compared to performing an experiment.

For the present study, computational approach has been used for both aerodynamics (Computational Fluid Dynamics CFD) and aeroacoustics (Computational AeroAcoustics CAA). For the purpose, Dassault Systèmes PowerFLOW has been used. PowerFLOW uses Lattice-Boltzmann Very Large Eddy Simulation (LB-VLES) approach for solving the unsteady flow field in the domain. Lattice-Boltzmann Method (LBM) is preferred over traditional Navier-Stokes solver due to its computational efficiency and effectiveness in solving unsteady problems. This is due to the fact that it has low dispersion and dissipation properties [8] [25]. Flow field visualization was performed in the post-processing software PowerVIZ, wherein various aerodynamic parameters were analyzed for quantifying flow phenomena. For aeroacoustics post-processing, PowerACOUSTICS was used which employs Ffowcs Williams-Hawkings (FWH) analogy to perform far-field analysis to obtain pressure fluctuations at a point in the rotor flow field. Furthermore, MATLAB was used to calculate the noise generated through the help of its in-built Fast-Fourier Transform (FFT) algorithm. At

every stage possible, the results were compared with experimental results to validate the computational setup. A detailed description of the *Methodology* and *Setup* is given in Chapter 4 and Chapter 5 respectively.

1.4. Report outline

The report has been divided further in different chapters as follows:

- Chapter 2 presents the fundamentals of aeroacoustics and noise generation mechanisms for an open rotor.
- Chapter 3 presents the basic geometry and fundamental flow physics of a co-rotating rotor which affects both the aerodynamic and aeroacoustic characteristics, previous studies performed by various authors and the research objectives formulated.
- Chapter 4 presents the methodology employed for both aerodynamic and aeroacoustic analyses.
- Chapter 5 presents the computational setup and software used for the purpose, along with details of various configurations tested.
- Chapter 6 presents the results obtained for all configurations and the subsequent explanations for flow phenomenon observed.
- Finally, chapter 7 presents the conclusions of the study, the relevance of the results obtained and how the present work can be extended further into a full analysis of a co-rotating rotor.

2

Fundamentals of Aeroacoustics

In this chapter, the basics of aeroacoustics are discussed so that the reader gets familiar with the fundamental concepts before the results can be discussed. Initially, definition of sound, methods for its analysis such as fourier transform and important terms have been presented. Then, the linear wave equation and various analogies developed by Lighthill, Ffwocs-Williams and Hawkings, etc. are discussed. The chapter ends with some discussion about rotor noise and its analysis.

2.1. Fundamentals

2.1.1. Definition of sound

Sound is defined as pressure fluctuations travelling in a medium, either solid, liquid or gas, propagating as a longitudinal wave. The speed at which sound travels is a fixed value c which depends on the medium in which it propagates. Table 2.1 lists speed of sound for various media common in daily life. Figure 2.1 shows a typical longitudinal wave and the way sound propagates. Longitudinal wave is composed of compression (high pressure) and rarefaction (low pressure) regions alternatively. Due to the displacement of medium particles, both the compression and rarefaction regions traverse in the direction of particle displacement and as a consequence, the wave propagates. Thus the particles are displaced in the direction of wave propagation, which is different from a transverse wave where particle displacement is in the perpendicular direction.

Medium	Speed (m/s)
Air at 20^oC	343
Air at 0^oC	331.3
Water at 20^oC	1481
Rubber	60
Aluminium	6320
Copper	4600

Table 2.1: Sound speed for common media
Source: NDT Resource Center

Every sound wave has a particular frequency associated to it. Human ear can detect sound waves in a range of 20-20000 Hz. Some animals are able to detect sound outside this frequency range too.

Any kind of unwanted sound is termed as noise. Therefore noise, in most cases, is the by-product of a physical phenomenon of which the original purpose was not to generate noise. While analyzing

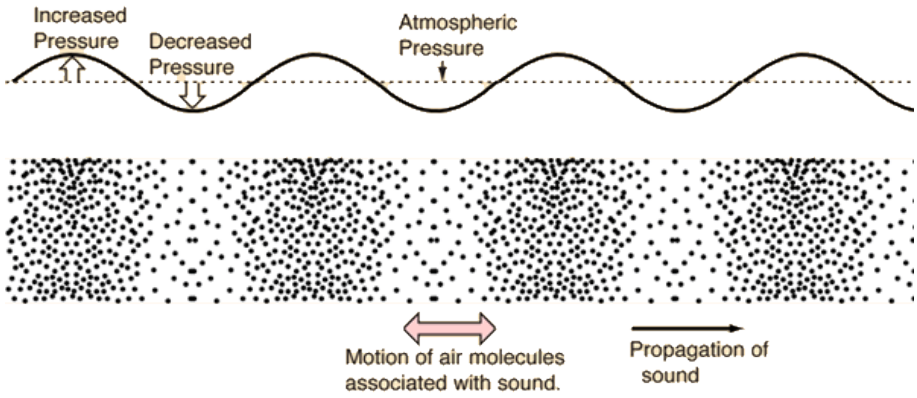

Figure 2.1: Sound as longitudinal wave
Source: Hyperphysics

noise, focus is mainly given to human hearing range and especially mid-frequency range (100-5000 Hz) where human ears are most sensitive.

2.1.2. Measurement of sound and its analysis

Sound can be measured by sampling the pressure perturbations in the medium. The fundamental unit used is Pascal (Pa). For humans, 2×10^{-5} Pa is the threshold of hearing and 200 Pa is the threshold of pain.

The most common physical quantity to measure sound is Sound Pressure Level (SPL) which is defined as:

$$\text{SPL} = 10 \cdot log \frac{P^2}{P_{\text{ref}}^2} \tag{2.1}$$

where, P is root mean square of pressure perturbations measured, P_{ref} is the reference pressure level and is usually defined as 2×10^{-5} Pa (threshold of hearing). The unit is decibel (dB).

Typically, a sound pressure signal consists of various frequencies and it is important to separate contributions of different frequencies. This is done using Fourier transform, which uses Fourier series to separate a signal into various cosine and sine terms. Each of these terms is associated to a particular frequency and the amplitude of these terms gives the contributions to the overall noise. A common algorithm for Fourier transform is the Fast Fourier Transform (FFT) which has been employed in the present study using MATLAB.

A common method to represent contributions of different frequencies is by plotting a sound spectra, as shown in Figure 2.2. Log scale is used to accommodate a large range of frequencies of interest which vary over several orders of magnitude. Thus by analyzing a noise spectra, energy contained in each frequency can be obtained. For humans, a separate quantity A-weighted SPL (dBA) takes preference over SPL as it takes into account the hearing range and response of human ear for a particular frequency. For the purpose, a weighting function is applied to each frequency where more weightage is given to frequencies for which the human ear is more responsive. Figure 2.3 compares the same signal not weighted and A-weighted [1]. Another quantity commonly used is Overall SPL (OASPL) which includes the contribution of a range of frequencies. This is obtained by integrating the energy contained in a spectra over the specified range of frequency.

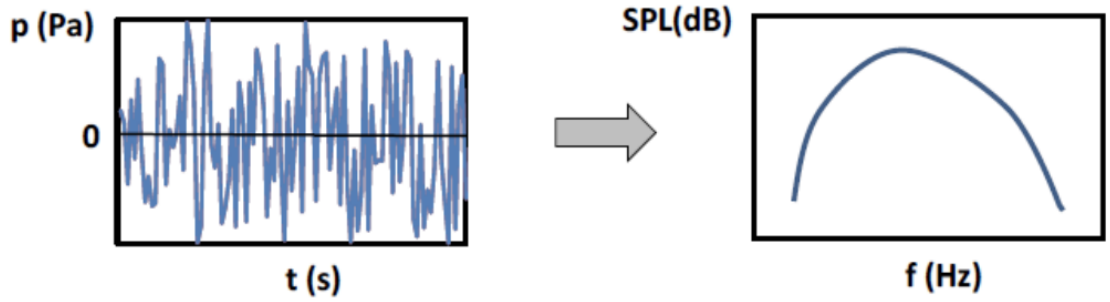

Figure 2.2: Fourier transform from pressure signal (left) to noise spectra (right)
Source: Adapted from Anselmi [1]

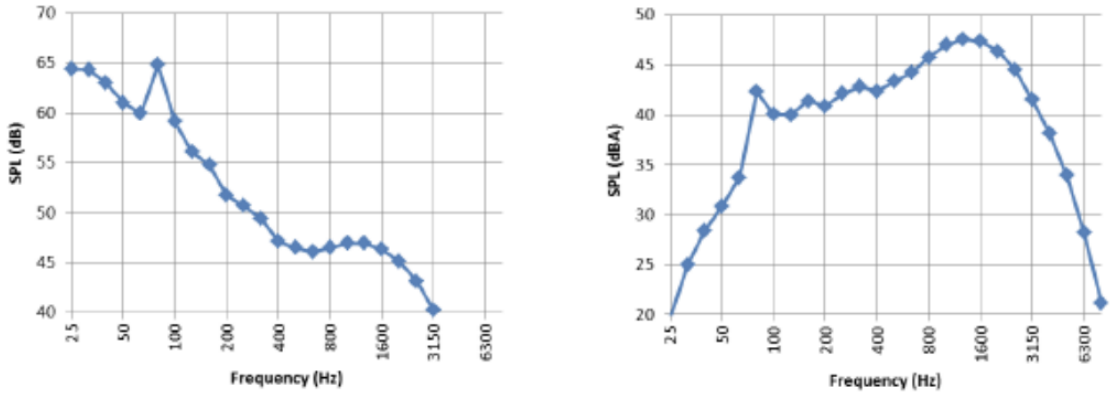

Figure 2.3: Noise spectra without weightage (left) and with A-weightage (right)
Source: Adapted from Anselmi [1]

2.2. Noise propagation and aeroacoustic analogies

2.2.1. Linear wave equation

In case of a stationary fluid, where there is no flow and time averaged properties are uniform throughout the domain of interest, the only source of pressure and velocity fluctuations are the acoustic waves (the acoustic wave source maybe present outside the domain of interest). It is assumed that the perturbations in the medium are much smaller than the mean value of the parameter (density, velocity, pressure, etc), thus, smaller linear perturbations are assumed. A relationship between density (ρ') and pressure (p') perturbations for a wave that propagates isentropically is given as:

$$p' = \rho' c^2 \qquad c^2 = \left(\frac{\partial p}{\partial \rho}\right) \tag{2.2}$$

where, c is the speed of sound, which is defined by the isentropic bulk modulus of the medium. To develop the linear acoustic wave equation, the assumption of small perturbations needs to be applied to continuity and momentum equation [17].

Continuity equation

The continuity equation is given as follows:

$$\frac{\partial \rho}{\partial t} + \frac{\partial (\rho v_i)}{\partial x_i} = 0 \tag{2.3}$$

Momentum equation

The momentum equation is given as follows:

$$\frac{\partial(\rho v_i)}{\partial t} + \frac{\partial(\rho v_i v_j + p_{ij})}{\partial x_j} = 0 \tag{2.4}$$

Linear acoustic wave equation

After applying the assumptions and neglecting non-linear terms in the momentum equation, the linear acoustic wave equation 2.5 is obtained by combining the continuity and momentum equations. It is a second order linear partial differential equation and the solution will depend on initial and boundary conditions of the problem.

$$\frac{1}{c_o^2}\frac{\partial^2 p'}{\partial t^2} - \frac{\partial^2 p'}{\partial x_i^2} = 0 \tag{2.5}$$

2.2.2. Lighthill's acoustic analogy

In the previous section, some assumptions were taken such as uniform stationary medium in which pressure perturbation was only caused by the linear acoustic wave equation. In real scenario, there are number of other factors which generate sound, one of them being turbulence in the flow. Generally, turbulence occurs in high Reynolds number flows where viscous effects are small and non-linear interactions are dominating. The assumptions related to linearization of equation of motions are thus not valid and there needs to be a separate approach for sound generation by an unconfined turbulent fluid flow.

Lighthill [22] [23] proposed an analogy between the sound generation by large velocity fluctuations inside the turbulent flow and acoustic wave which propagates to the acoustic far field in a stationary medium. The idea is to give an equation for propagation of sound waves and not to define the fluid motion in the turbulent flow. His analogy is based on the exact equations of fluid flow, so no assumptions are made related to the flow compressibility effects. The wave equation is obtained [17] as:

$$\frac{\partial^2 \rho'}{\partial t^2} - c_\infty^2 \frac{\partial^2 \rho'}{\partial x_i^2} = \frac{\partial^2 T_{ij}}{\partial x_i \partial x_j} \tag{2.6}$$

$$\text{where,} \qquad T_{ij} = \rho v_i v_j + (p - p_\infty) - (\rho - \rho_\infty) c_\infty^2 \delta_{ij} - \sigma_{ij} \tag{2.7}$$

The left hand side describes acoustic wave propagation in a uniform medium with sound speed c_∞, which is similar to the linear wave equation although using density as the dependent variable. The right hand side is referred to as a source term which contains all the effects that generate acoustic waves in the term T_{ij} which is known as the Lighthill's stress tensor. The modeling of turbulence and issues related to it are included in this term. Thus, the above inhomogeneous wave equation can also been seen as a wave equation in the presence of any source term, which was not present in the equation 2.5.

2.2.3. Curle's theorem

The Lighthill's equation is solved using the method of Green's function giving a solution which is valid everywhere outside the turbulent flow region where the medium is at rest and uniform. The limitation of Lighthill's analogy is that it considers the source of acoustic waves as only the turbulent flow. Curle [12] extended the Lighthill's concept to include the contribution from surfaces present in the flow. The solution is given [17] as:

$$\rho'(\mathbf{x},t)c_\infty^2 = \int_{-T}^{T}\int_S \left(\left(p_{ij} + \rho v_i v_j\right)\frac{\partial G}{\partial y_i} + G\frac{\partial\left(\rho v_j\right)}{\partial \tau}\right) n_j dS(\mathbf{y}) d\tau + \int_{-T}^{T}\int_V \left(\frac{\partial^2 G}{\partial y_i \partial y_j}\right) T_{ij}(\mathbf{y},\tau) dV(\mathbf{y}) d\tau \tag{2.8}$$

There are two major restrictions to Curle's method: the surfaces in the fluid should be stationary and the medium outside the flow should be at rest. The 4 major source terms for acoustic wave in equation 2.8 depend on:

1. force per unit area p_{ij} applied to the fluid by the surface
2. momentum flux $\rho v_i v_j$ across the surface
3. rate of change of mass flux ρv_j across the surface
4. contribution from volume sources from distribution of Lighthill's stress tensor T_{ij}

2.2.4. Ffowcs-Williams and Hawkings equation

Modern day applications for aeroacoustics also include rotors, propellers, etc. which has moving surfaces and thus cannot be addressed by earlier methods. Ffowcs-Williams and Hawkings (FWH) [15] gave a solution to Lighthill's equation that includes moving surfaces and convected turbulent flow. It uses the concept of generalized derivatives such as Heavyside step function $H_s(x)$ and solves using the method of Green's function as was done before. The FWH equation finally becomes [17]:

$$\begin{aligned}\rho'(\mathbf{x},t)c_\infty^2 H_s = &\frac{\partial^2}{\partial x_i \partial x_j}\int_{V_o}\left[\frac{T_{ij}}{4\pi r|1-M_r|}\right]_{\tau=\tau^*} dV(\mathbf{z}) \\ &- \frac{\partial}{\partial x_i}\int_{S_o}\left[\frac{\left(\rho v_i\left(v_j - V_j\right) + p_{ij}\right)n_j}{4\pi r|1-M_r|}\right]_{\tau=\tau^*} dS \\ &+ \frac{\partial}{\partial t}\int_{S_o}\left[\frac{\left(\rho v_j - \rho' V_j\right)n_j}{4\pi r|1-M_r|}\right]_{\tau=\tau^*} dS\end{aligned} \tag{2.9}$$

There are three terms which are significant:

1. *volume source* term named as quadrupole; the strength depends on T_{ij} and is the sound radiated both by turbulence and flow distortions
2. *surface loading* term named as dipole; the strength depends on surface loading p_{ij} and the term containing $(v_j - V_j)$ where, v_j is flow velocity at the surface and V_j is the surface velocity
3. *thickness noise* or volume displacement term named as monopole; the strength depends on $\rho V_j n_j$ which depends on surface velocity (in case of propeller: blade surface velocity) and the density at the observer

The FWH equation is solved by substituting all the source terms which are obtained from a flow field simulation of the problem. The integrands are evaluated at emission time $\tau = \tau^* = t - r(\tau^*)/c_\infty$, therefore, if the source is moving then the emission and observed time history for the observer are displaced with respect to each other. The time differentials can be shifted between the observed time and source time by using:

$$\frac{\partial}{\partial t} = \frac{\partial \tau^*}{\partial t}\frac{\partial}{\partial \tau} = \frac{1}{1-M_r}\frac{\partial}{\partial \tau} \tag{2.10}$$

where, t is the observed time at the observer and τ is the source time at the noise source location. The equation can be solved both by using the observed or emission time approach and the choice depends on the suitability of the problem. The practical implementation of FWH, especially in Dassault Systèmes PowerFLOW, will be discussed in Section 4.2.

2.3. Rotor noise

The term rotor and propeller, although used interchangeably, are associated with different configurations. Rotor is a general term used to refer to any rotating object. With respect to aircraft, it is mainly associated with helicopter rotors or vertical take-off systems. Propeller is used to refer to rotors used in forward flight regime such as in turboprop aircraft. In this report, both the terms mean the same as the focus was on analyzing hover configurations.

The main purpose of a rotor is to generate thrust. In the process, it also produces unwanted noise due to fluid interactions happening with the rotor blades. Rotor noise is a major problem in various applications. Propeller-driven aircraft is greatly affected by such problems especially for cabin and passengers sitting inside. Ship propellers need to produce little noise to lower shipboard noise and noise produced in the far field, especially for military ships. Wind turbines and helicopter rotors face similar problems of noise generation. Therefore while designing a rotor, lowering noise is amongst the many design objectives which puts constraint on various design parameters.

In each of the examples above, the sources of noise generation are the same but relative importance for each source vary between different applications. For low speed flights, *surface loading noise* given by second term in equation 2.9 is dominant. Thus, both steady and unsteady loading on rotor blades act as a source of noise with the latter generally contributing more than the former. As Mach number increases, first (*quadrupole noise*) and third (*thickness noise*) terms in equation 2.9 also become important especially in case of supersonic propellers.

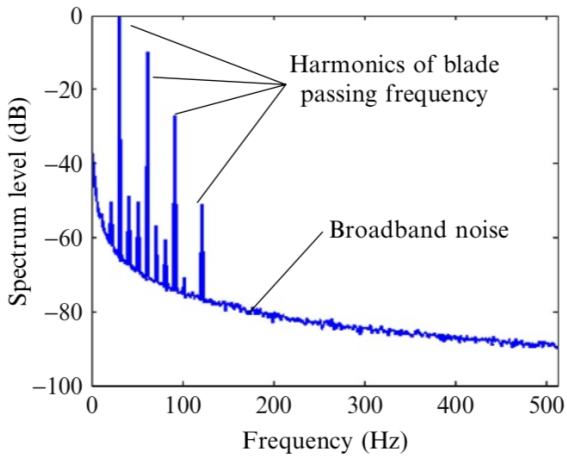

Figure 2.4: An example of a rotor noise spectra
Source: Devenport [17]

When a noise spectra is observed for a rotor, as shown in Figure 2.4, two distinct types of noise can be observed: 1) *tonal* 2) *broadband. Tonal* noise is the result of sources that repeat themselves periodically at a specific period, in case of rotor which is, the period of rotation. This can be due to either thickness or loading noise. An example of a pressure signal which gives tonal contribution is shown in Figure 2.5 (A) and (B). The peak for tonal noise (highest energy content) is observed at Blade Passage Frequency (BPF) which is given as:

$$\text{BPF} = rps \cdot b \tag{2.11}$$

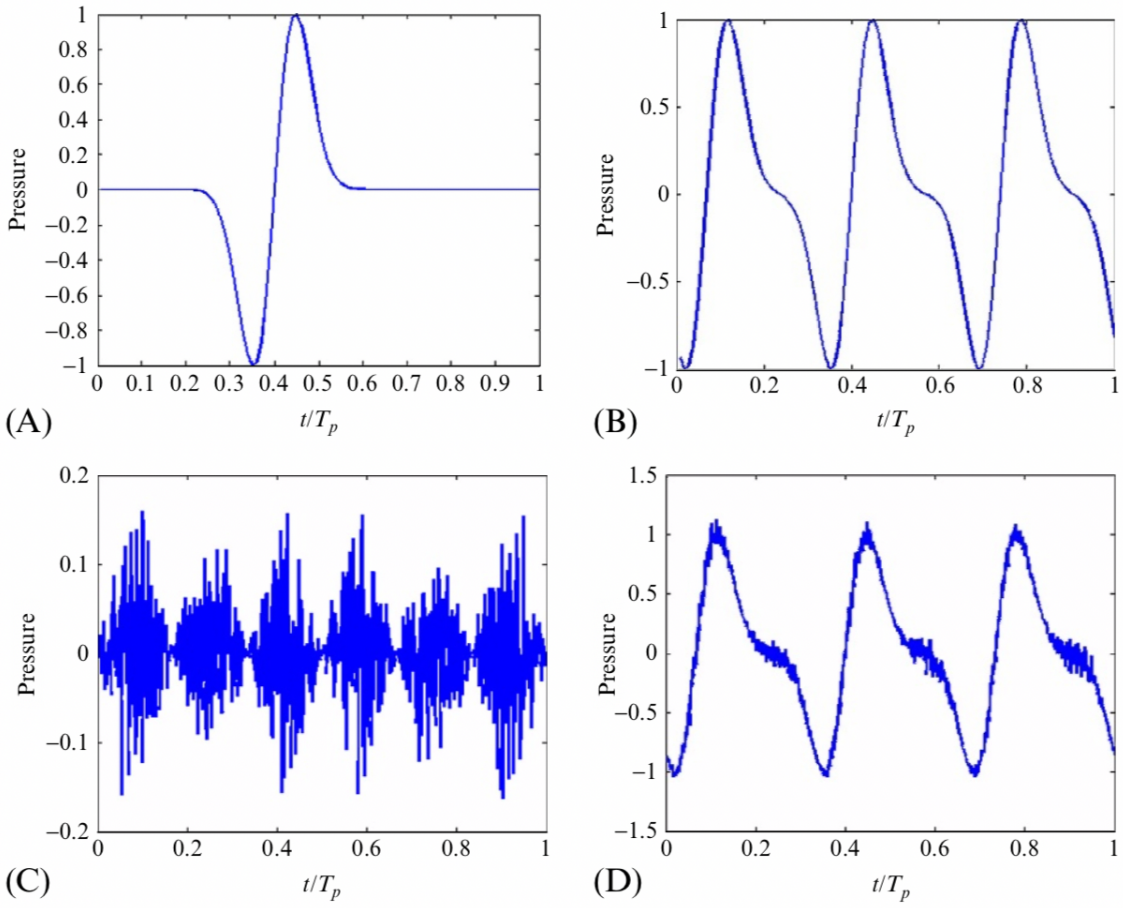

Figure 2.5: (A) Pressure signal from a single blade (B) Pressure signal from a 3-bladed rotor (C) Pressure signal for a broadband rotor noise (D) Pressure signal of a rotor combining tonal and broadband contribution; y-axis (Pressure) is non-dimensional
Source: Devenport [17]

where, *rps* is rotations per second and *b* is number of rotor blades. Further peaks are observed at multiples of BPF with decreasing intensity.

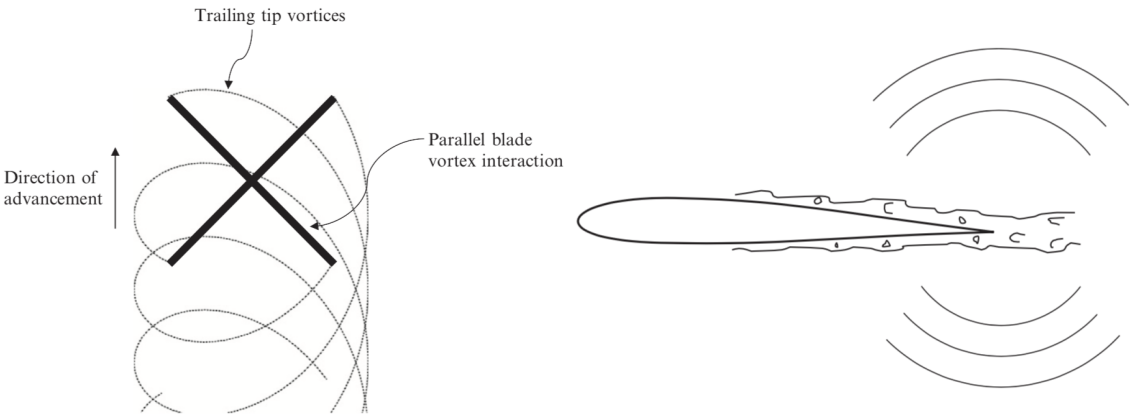

(a) Blade Vortex Interaction (BVI) (b) Trailing edge noise

Figure 2.6: An example of blade vortex interaction and an airfoil depicting trailing edge noise
Source: Devenport [17]

Broadband noise is characterized by random, non-periodic signal and contains a mix of various continuously distributed frequencies, which can be due to various sources [24]. One reason can be unsteady loading on blade surface which can be due to Blade Vortex Interaction (BVI) as shown in Figure 2.6 (a), turbulent inflow on rotor blades or trailing edge noise generated due to turbulent boundary layer interaction with the trailing edge (Figure 2.6 (b)). Another reason can be shock formation around the blade tip in case local Mach number increases more than 1, which acts as a quadrupole noise source. An example of a pressure signal which gives broadband contribution is shown in Figure 2.5 (C).

In case of a *personal air vehicle*, the rotor will operate in a low Mach number condition. Therefore, as mentioned earlier, most important noise contribution comes from *loading noise* which will be generated due to force fluctuations on the rotor blade. In the present study, an investigation has been performed to mitigate such noise generation mechanisms and the potential role that can be played by the co-rotating rotor for such purpose.

3

Co-rotating rotors

3.1. Historical background

3.1.1. Rotors

Rotors/Propellers have a very long history originating from early windmill designs in the 13th century in Europe and China. Major changes came after the development of propeller theories around 19th century with William Rankine proposing axial momentum theory in 1865 [21] and blade element theory by William Froude in 1878 [21]. Various theories were proposed thereafter but these two theories continue to be widely popular till today. Wright Brothers in their Wright Flyer I (Figure 3.1 (a)) used two propellers driven by a gasoline engine, to mark the beginning of the aeronautical era in 1903. Their propellers had an efficiency of 81% (according to NASA Wind Tunnel tests [18]) and this shows the simplistic nature of a propeller design. This is for the same reason propeller is a preferred choice in many aircrafts (for low speed flights) compared to turbofan or turbojet engine (which is mainly employed for high speed flights).

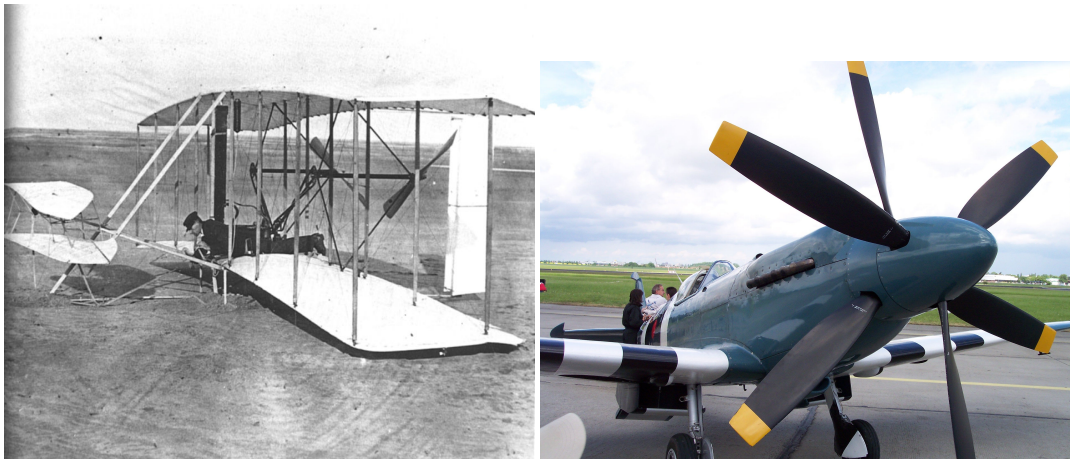

(a) Wright Flyer I by Wright Brothers

(b) Supermarine Spitfire with 6 contra-rotating blades, and a hub in front

Figure 3.1: Rotorcrafts of 20th century
Source: *www.wright-brothers.org* and *Stahlkocher*

Propeller research in the 20th century expanded rapidly and was driven by various factors. World War I and II were major factors in the first half of 20th century while the second half comprised factors such as Cold War and race for control of oil-producing countries in the Middle East. Various

types of propeller concepts and configurations came up such as contra-rotating, tandem, etc. with each of them being employed for different applications. The Supermarine Spitfire (Figure 3.1 (b)) during World War II used contra-rotating propellers with 5-6 blades. 5-bladed props were more common than 6-bladed due to various issues in the latter such as higher flow interference between successive blades, increased weight and mechanical complexity (due to more number of blades), etc. In the present-day propellers, due to higher aerodynamic efficiency and use of composites, these problems have been mitigated with 6-bladed props being in use in a multitude of aircrafts.

Propeller research in the late 20th century and beginning of 21st century progressed quickly owing to the development of a new generation of aircrafts, both in civil and military areas. Various other factors played role such as electrification, infrastructure, transportation, cities, etc. with electrification being one of the major focus to reduce the impact of fossil fuels. It involves either replacement of gasoline engines with batteries in the present aircrafts or introduction of a new series of electric aircrafts. Currently, since power density for batteries is less than gasoline fuels, a lot of focus is given on efficiency of a rotorcraft which in turn requires efficient propeller designs. Thus, unconventional configurations such as *co-rotating rotor* has come into focus which have not been explored in-depth up till the present day. Having a potential to improve the efficiency of rotorcrafts, was the main motivation behind choosing such rotor configuration for the present study.

3.1.2. Urban Air Vehicles

The concept of small-scaled air vehicles started coming up in the late 20th century. Initially, the application was mainly focussed on military areas such as surveillance or attack drones but realizing the potential of such vehicles, it quickly grew its application towards civilian areas especially in the 21st century. The most common type of such air vehicles is a *multicopter*, with 4-8 rotors on each aircraft and which can be used in Vertical TakeOff and Landing (VTOL) mode. Another recent concept is *Urban Air Mobility* (UAM) where small scaled personal air vehicles will be utilized to transport people and goods in urban areas, thus avoiding congestion on the vehicular road traffic and improving the quality of life experienced by the city residents. All of these air vehicles operate in low Mach number conditions, and therefore, rotor being more efficient in such flow conditions is a preferred choice. Example of UAM vehicles are shown in Figure 1.1.

The concept of UAM incorporates developing an electric vehicle for the urban environment. This requires the vehicle design to be highly efficient and produce less noise. Rotors form an important component of such vehicles and thus, requirements of efficiency and noise ultimately become the driving factor for the design of a rotor. Due to this reason, exploring unconventional rotor configurations become increasingly important. *Co-rotating rotor* is one such configuration which offers promising improvements in both performance and acoustics, according to some of the research work already conducted [5] [37]. A detailed look into the fundamental flow physics of such rotors and the previous studies performed by different authors will be discussed in the next few sections.

3.2. Flow physics of co-rotating rotor

Basics of thrust generation

The basic function of a rotor is to convert engine torque to axial thrust or propwash. When a cross-section of a propeller blade is analyzed, the shape observed is that of a typical airfoil. Thus, propeller blades are basically a wing rotating about an axis called center of rotation. The center is covered in front by a non-aerodynamic part called hub as shown in Figure 3.1 (b). The blades experience similar forces of lift and drag as a wing during forward flight. Incoming airflow is called relative airflow (RAF) (shown in Figure 3.2 (a)) and outgoing airflow is called propwash. During rotation, blades push air backward and in opposite reaction, the air pushes the propeller forward. This is the basic phenomenon of thrust generation.

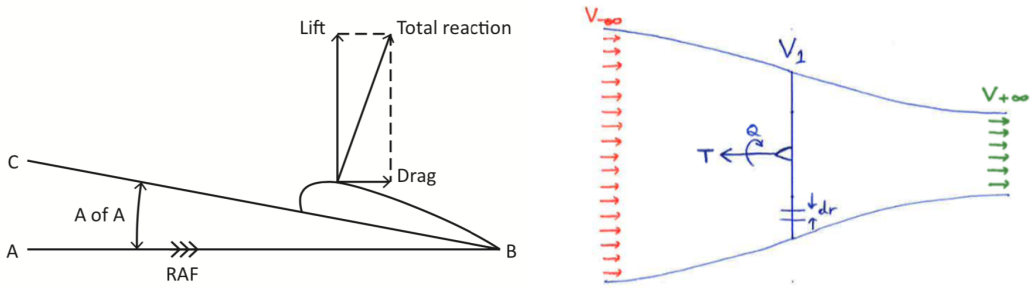

(a) Velocity experienced by a rotor blade airfoil (b) Propeller streamtube

Figure 3.2: Rotor blade cross-section and propeller streamtube formed when thrust in being generated
Source: Hitchens [18]

When a propeller is producing thrust, the surrounding flowfield is changed due to the interaction of propeller blades with the flow media. The flow that comes out of propeller is called wake. Figure 3.2 (b) shows a diagrammatic representation where the incoming air comes from left side ($V_{-\infty}$) and the wake is on right side ($V_{+\infty}$) whereas V_1 is the propeller. The two blue streamlines passing through the ends of propeller depict the path taken by the flow and is called as *streamtube*. Thus, the *streamtube* encloses the flow which is processed by the propeller.

The co-rotating rotor can be visualized as a superposition of two *streamtubes* of the two rotors, separated by an axial distance. Therefore, each rotor is acting in the streamtube of the other rotor which induces mutual interaction between the rotors and therefore, affecting the performance and acoustic characteristics of both, as compared to an isolated propeller case. This is shown in Figure 3.3 where a diagrammatic visualization of each rotor's streamtube is done. The total thrust of the rotor is distributed between the upper and lower rotor. Since the upper rotor acts in a freestream flow and the lower rotor acts in a disturbed flow (wake of the upper rotor), the thrust contribution of former is more than the latter. This is reflected in the streamtube shape, where, upper rotor has more contraction than the lower rotor. This is true for any co-axial rotor such as the contra-rotating configuration (in which two rotors spin in opposite direction).

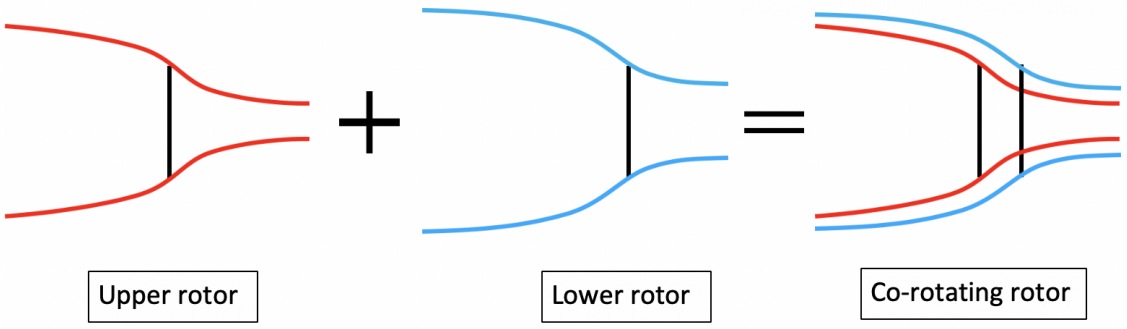

Figure 3.3: Individual streamtube of the upper (red) and lower rotor (blue), in a co-rotating rotor; black lines - rotor disc

The variation of *axial* or *azimuthal* separation in a co-rotating rotor changes the interaction between the rotors. This can either have a positive or a negative impact on each rotor. The purpose of this study was to investigate this interaction effect by understanding the behaviour of each rotor, and how the performance of the co-rotating rotor can be increased as a whole while having minimal impact on other parameters.

Blade-Vortex Interaction

Similar to a wing, vortices are produced in the wake of a propeller from each blade that either interact with other blades (Blade-Vortex Interaction) or are convected with the flow, as shown in Figure 3.4 (a). Vortices are shed from three regions: *trailing edge, hub*, and *tip*. These vortices create disturbance in the flow field, reduces efficiency and creates more drag. *Tip vortices* are much stronger than *trailing edge* and *hub vortices*, and are important factors affecting the performance of a rotor. In case of a co-rotating rotor, the lower rotor interacts with both the upper rotor (*rotor-rotor interaction*) and lower rotor vortices (*self interaction*). This adversely affects the performance of the lower rotor and thus, thrust contribution decreases. One of the important objectives of this study was to investigate the tip vortices behaviour as axial or azimuthal separation is changed and how the BVI can be avoided for an increase in performance of the co-rotating rotor.

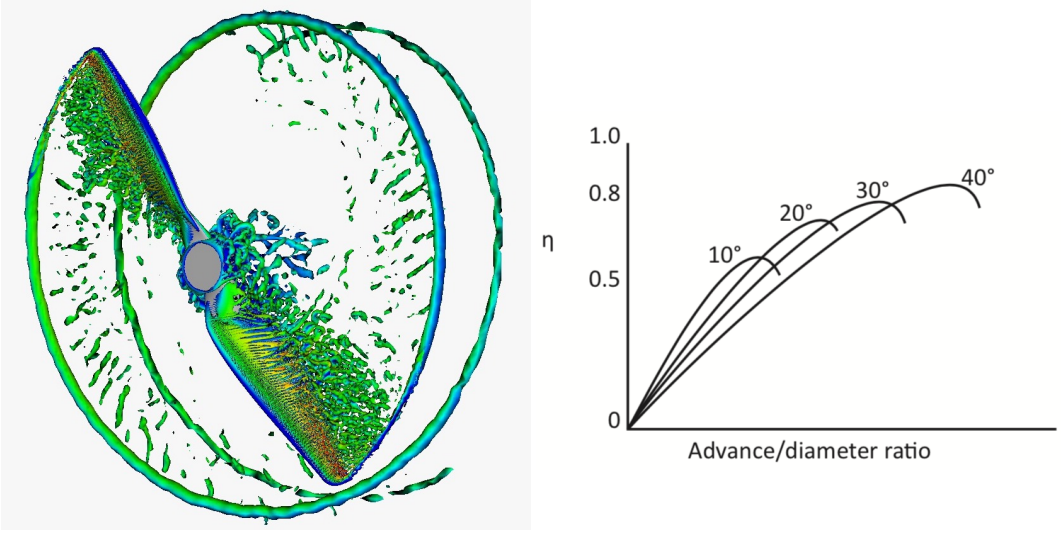

(a) Tip vortex trajectory

(b) Efficiency vs Advance/diameter ratio

Figure 3.4: Propeller tip vortex trajectory and its efficiency variation
Source: E. Grande, TU Delft and Hitchens [18]

Fundamental quantities

A quantity which measures how efficiently a thrust is generated is *propeller efficiency* (equation 3.1), which basically determines the amount of thrust produced for a particular amount of power supplied to the propeller. In other words, it is a measure of how efficiently a volume of fluid is displaced rearwards or how well a propeller can absorb the supplied engine power. Another term commonly used to define propeller performance is *Figure of Merit* (FOM) which is basically induced power divided by power available or, how much power is being utilized for accelerating the air. FOM value of 1 is the highest possible value than can be achieved theoretically. In case of any co-axial rotor, FOM is defined by equation 3.2.

$$\eta = \frac{T \cdot u_0}{P_{in}} \tag{3.1}$$

where, T is thrust generated, u_0 is flight velocity and P_{in} is power input to the propeller.

$$FOM = \frac{(T_u^{3/2} + T_l^{3/2})\sqrt{2\rho A}}{P_{in}} \tag{3.2}$$

where, T_u and T_l is thrust generated by upper and lower rotor respectively, A is propeller swept area, ρ is air density, and P_{in}=P_u+P_l where, P_u and P_l is power input to upper and lower rotor respectively.

The most common factors affecting propeller efficiency are *collective pitch* and *flight velocity*. *Collective pitch* is a term which refers to change in AoA of the rotor blade as a whole. Each blade section is twisted at a particular angle so that the AoA experienced by the blade is constant throughout the span. If the collective pitch is increased, thrust increases even though the rotational speed stays constant. *Collective pitch*, sometimes also referred to as *pitch*, is normally specified in degrees, where 0 degree corresponds to a baseline blade position. Figure 3.4 (b) shows a typical variation for efficiency of a propeller with *advance/diameter ratio J* (equation 3.3) and *pitch* angle.

$$J = \frac{u_0}{nD} \tag{3.3}$$

where, n is rotations per second and D is propeller diameter.

In the present study, since only hover cases have been investigated, the value for *advance/diameter ratio* will be very close to zero, and therefore will have very less efficiency values. The tip vortices remain very close to the rotor plane in case of hover, as compared to a forward flight case and this impacts the performance of the rotor, decreasing its efficiency. This is also the reason performing a computational simulation for a hover case is very challenging due to the need to resolve all the vortices close to the rotor.

Noise generation

Since both the upper and lower rotors are producing thrust, there will be noise contribution due to both the rotors at a particular location in the flowfield. Due to axial and azimuthal separation of the blades, the total noise will depend on the particular configuration of the co-rotating rotor. Figure 2.5 (D) in Chapter 2 showed that overall pressure fluctuations from a rotor are periodic fluctuations. Therefore, there is possibility of constructive or destructive interference between both the rotors and this will ultimately depend on the axial and azimuthal separation between the blades. As this separation varies, so will the total acoustic signature of the co-rotating rotor.

There will be additional BVI taking place between the upper and lower rotor (*rotor-rotor interaction*), which is not present in case of an isolated rotor. This further increases the unsteady force fluctuations on the rotor blades, and as a result, the broadband part of noise increases. The purpose of the study was also to investigate the possibility of reducing the total noise (both tonal and broadband) produced by a co-rotating rotor, by investigating different configurations, while minimally affecting its aerodynamic performance.

3.3. State of the art

In this section, all the relevant previous studies on the co-rotating rotor are discussed. The results are summarized into various subsections, with each of them comparing results from different authors, mentioning various agreements and disagreements and, if possible, explanation of results based on understanding of flow physics. The referred literature includes one of the first investigations by NASA in 1974 and 1976 till the recent studies in the 21st century.

Figure 3.5 (a) and (b) show two different azimuthal angle configurations. White rotor is on top of black rotor and rotation direction is anti-clockwise. Various authors represent azimuthal angle by various symbols such as $\Delta\psi$, $\Delta\phi$, $\Delta\theta$, etc. For positive azimuthal angles, the upper rotor is ahead of lower rotor and vice-versa. This convention is followed during the whole study.

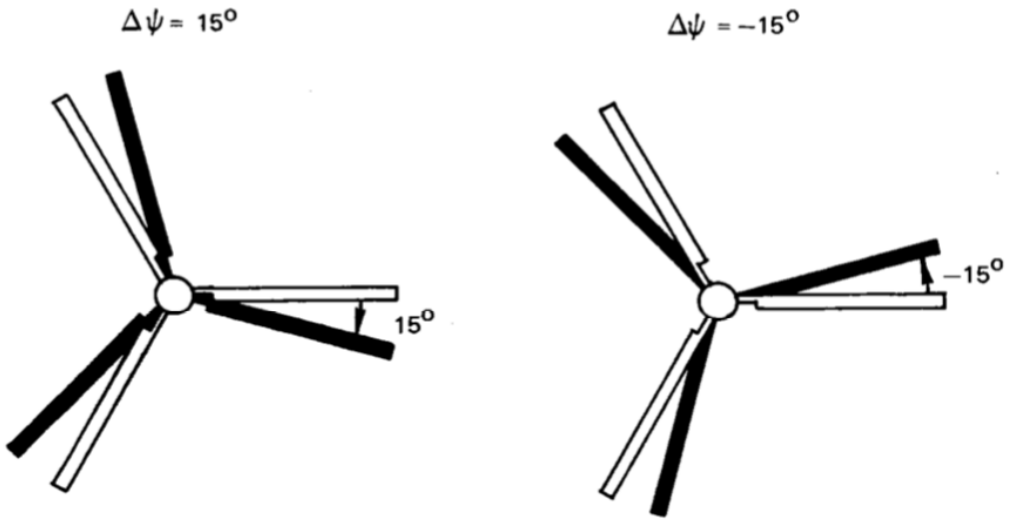

(a) Positive azimuth spacing (b) Negative azimuth spacing

Figure 3.5: Geometry convention
Source: Langrebe [20]

3.3.1. Co-rotating vs Contra-rotating

A common comparison is between a baseline co-planar rotor (a single rotor) and a contra- or a co-rotating rotor. Eg. a 2×2-bladed co-rotating rotor can be compared to an isolated 4-bladed or a 2-bladed rotor. A detailed comparison is done by Mahendra [5] in 2018. He compares a 6-bladed co-planar rotor, a 2×3-bladed co-rotating and a corresponding contra-rotating rotor. The azimuthal angle for co-rotating rotor was kept very small. The results show that the power requirement of contra-rotating rotor is less than co-rotating and baseline rotor, and the difference increases at higher thrust values. The difference between co- and contra-rotating rotors is 20-30 W at thrust values of around 100 N. A supporting hypothesis for this result is the *swirl recovery* in contra-rotating case. Due to propeller rotation, a swirl component is introduced in the freestream flow which redistributes the energy between angular and axial flow components, thus, there is a loss in axial direction. In case of contra-rotating rotor, the swirl in the wake of upper rotor is reduced by

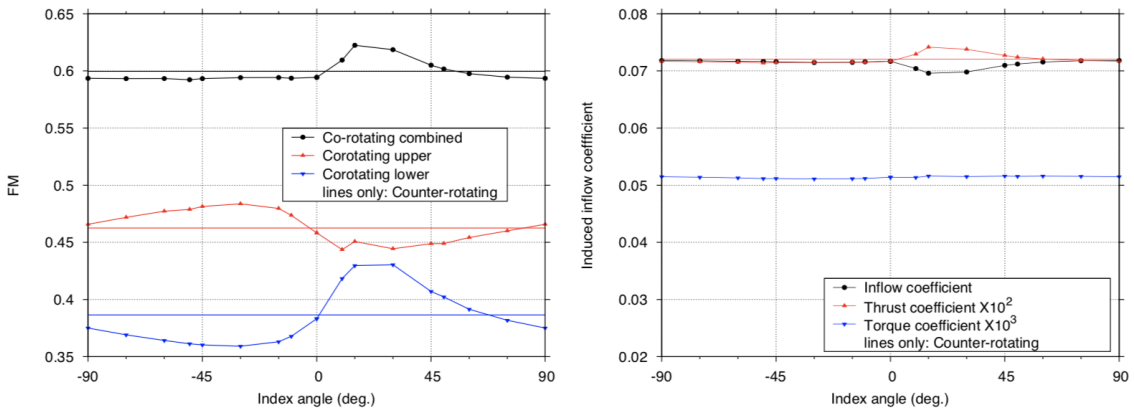

(a) Figure of Merit variation (b) Induced inflow variation

Figure 3.6: Comparison of Contra and Co-rotating rotors
Source: Mahendra [5]

lower rotor, mitigating swirl losses.

Next, the azimuthal angle was varied for the co-rotating rotor and it was found out that for particular values of azimuthal angle, co-rotating rotor performance is better than contra-rotating rotor, as shown in Figure 3.6 (a) and (b). A similar result was obtained by Uehara [38] in which a co-rotating rotor with 10^o azimuthal angle outperformed its contra-rotating counterpart. According to Mahendra [5], the contribution to better performance is mostly from the lower rotor as compared to the upper rotor. These results are in contradiction to swirl recovery hypothesis (which would favour contra-rotating rotor in all cases) and suggests that *induced inflow* effects play a major role for improved performance rather than *swirl recovery* effects, at these particular azimuthal angles.

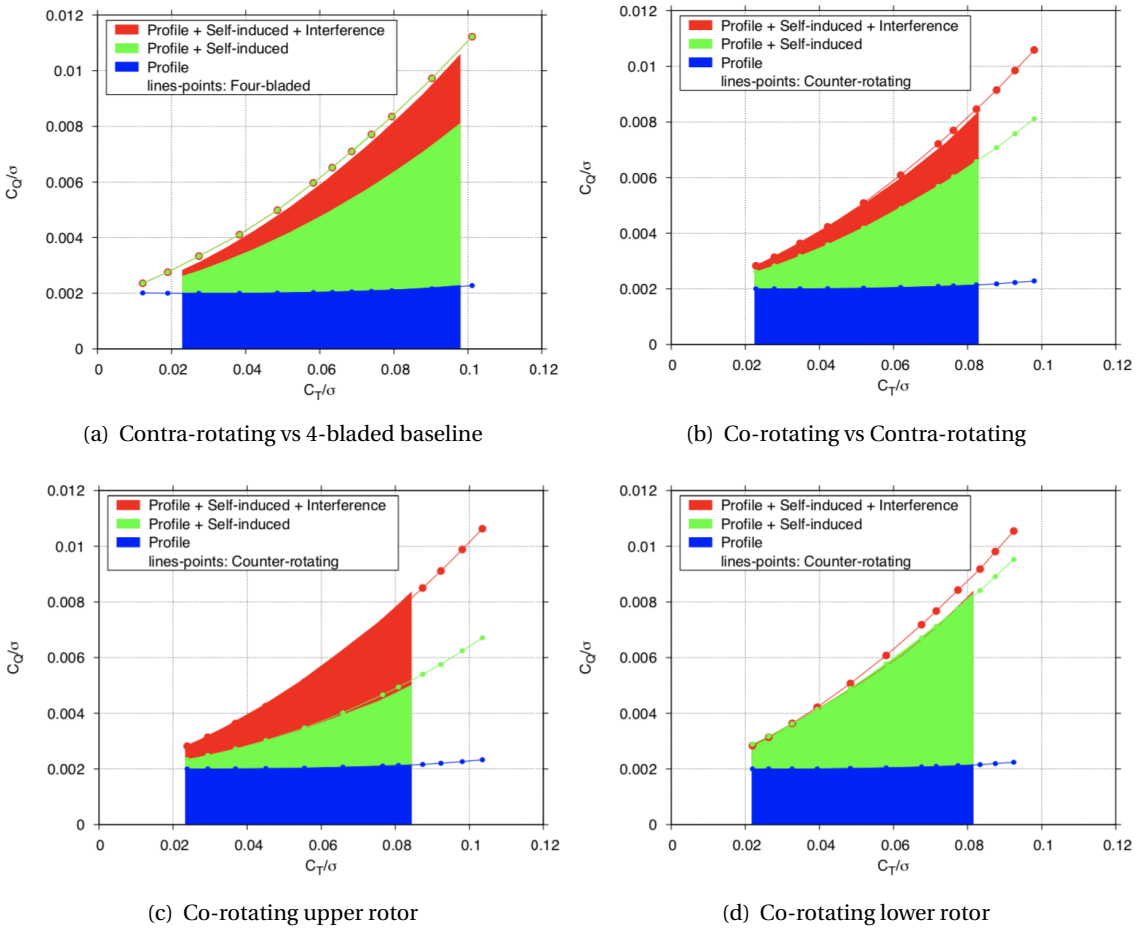

(a) Contra-rotating vs 4-bladed baseline

(b) Co-rotating vs Contra-rotating

(c) Co-rotating upper rotor

(d) Co-rotating lower rotor

Figure 3.7: Comparison of Contra and Co-rotating rotors, a detailed analysis
Source: Mahendra [5]

To perform a more detailed investigation and confirm the above hypothesis, the rotor torque was separated into 3 different components: *profile torque* (due to profile drag), *self-induced torque* (inflow induced by rotor's own wake) and *interference torque* (inflow induced by the other rotor and its wake). The result for 15^o angle is taken for co-rotating rotor which was the most efficient configuration obtained. Figure 3.7 (a) shows the comparison between contra-rotating and the corresponding 4-bladed baseline rotor. The torque requirement for the former is less, which mainly comes from reduction in *self-induced torque*, even though there is an extra *interference torque* added. A similar observation is seen in Figure 3.7 (b) where the overall torque for co-rotating is less than contra-rotating rotor, the reason being reduction in *interference torque* (rotor-rotor interaction). This is due to the fact that at particular azimuthal angles, tip vortex of upper rotor misses the lower rotor

blade, avoiding blade-vortex interaction.

In order to better understand contributions from upper and lower rotor, Mahendra [5] plotted their individual torque components as shown in Figure 3.7 (c) and (d) and compared to the contra-rotating rotor. The *self-induced torque* in the upper rotor is less as compared to lower rotor due to the fact that upper rotor wake convects down faster axially. The *interference torque* due to another rotor wake is far more in upper rotor than lower rotor (where it is almost negligible) due to increased proximity of lower rotor wake with upper rotor blades. The increase in *interference torque* in upper rotor is more than increase in *self-induced torque* in lower rotor, thus, increasing the overall torque requirement in the former. Combining both the upper and lower rotors, co-rotating rotor torque requirement is less than the contra-rotating rotor while the torque reduction mainly comes from the lower rotor. This proves that effects such as *induced inflow* (both self and interference) in case of co-rotating rotors can play a greater role at particular azimuthal angles than *swirl recovery* effect in case of contra-rotating rotors, making the former perform better. During the present study, a similar type of analysis has been carried out where a co-rotating rotor has been compared to a baseline rotor, while trying to understand the physical reason for the differences and similarities observed.

3.3.2. Azimuthal angle variation

Azimuthal angle is used by various names by different authors such as index angle, clock position or azimuthal separation, etc. As seen in the previous section, variation of azimuthal angle can show significant improvement in results over other configurations. One of the first investigations on co-rotating rotor was done in 1974 by Landgrebe [20] on a small scale 2×3-bladed rotor. The results show that azimuthal separations of 30°, 45° and -30° show the best improvement in performance and these improvements increase with increasing tip Mach number and thrust level. The higher axial separation gives even better performance at these particular azimuthal angles.

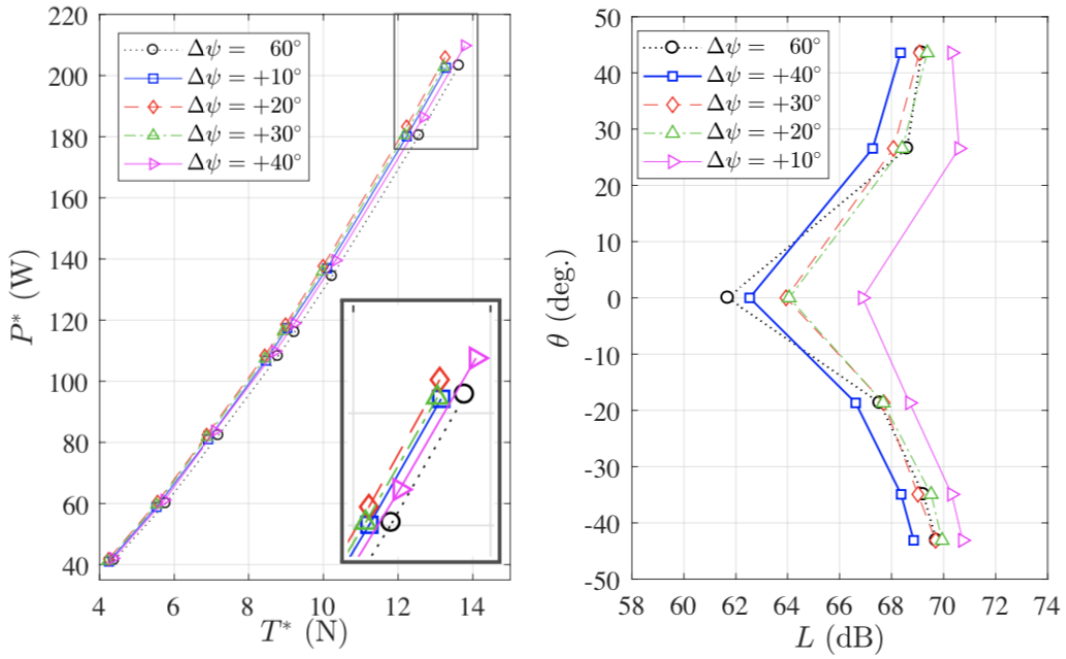

(a) Thrust results for $\Delta z/R = 0.15$

(b) Acoustic results for $\Delta z/R = 0.15$

Figure 3.8: Results for different azimuth spacing
Source: Whiteside [40]

A similar investigation was performed by Rorke [32] in 1976 on a full scale rotor (2×3-bladed

rotor). The most efficient configuration is obtained for 62.1° for lower tip Mach number and 43.6° for higher tip Mach number. This is slightly different from previous results in which most efficient configuration varied from 30° to 45°. This can be a result of different Reynolds number because of different scales of rotor. Another recent investigation was made by Whiteside [40] with 2×3-bladed co-rotating rotor, with one of the result for azimuthal separation shown in Figure 3.8 (a). Whiteside made a conclusion that highest thrust is obtained for 60° configuration in case of positive separation and −40° for negative separation. The first result is quite close to Rorke [32] who obtained 62.1° as the most efficient one and second result is close to Landgrebe [20] who obtained −30° as one of the most efficient ones.

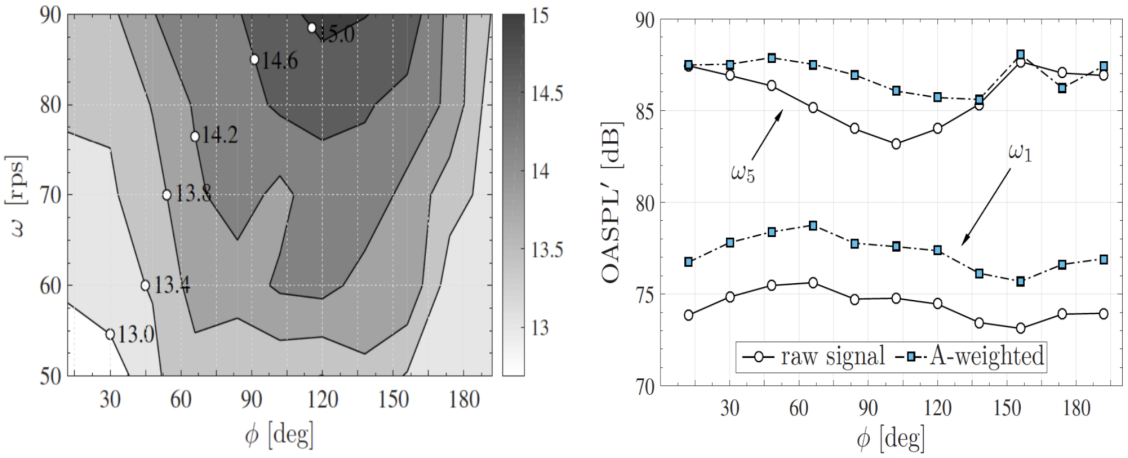

(a) Thrust contour for $\Delta z = 1$

(b) OASPL vs ϕ

Figure 3.9: Aerodynamic and Aeroacoustic results
Source: Tinney [37]

Tinney [37] also investigated such trends using a 2×2-bladed rotor, the results of which are shown in Figure 3.9 (a) depicting the thrust contour. It can be seen that as the azimuthal separation is increased (for a fixed value of ω) thrust value increases, goes to a maximum around $100^o - 120^o$ and then decreases again. The angle at which maximum thrust value is attained varies for different rotational speed (ω). The trend is same as obtained by previous authors, though they mentioned different azimuthal angles for maximum thrust value.

A number of aeroacoustic investigations were also conducted by various authors. Results from Whiteside [40] are shown in Figure 3.8 (b) where angular positions of measurement locations are plotted against OASPL (unweighted). The trend indicates that, for all angular positions, as azimuthal angle increases, OASPL value decreases. In the plane of rotor ($\theta = 0^o$), least noise is given by azimuthal separation of 60° which is the symmetrical configuration (since it is a 2×3-bladed rotor). Out of plane of rotor, OASPL value increases which is the same trend we observe from Tinney [37] and Bain [2]. The loading and thickness noise from a propeller are obtained as sinusoidal variations of pressure-time signal. In the plane of rotation, there is destructive interference between them which leads to a reduction in OASPL value, whereas, out of plane of rotation, the destructive interference decreases which leads to an increase in OASPL value. Tinney [37] also presented results for different azimuth separations shown in Figure 3.9 (b). For ω_5=90 rps, the trend is similar to the previous result from Whiteside [40], although for ω_1=50 rps, the trend slightly changes. Another analysis was performed by Rorke [32] as shown in Table 3.1. Maximum OASPL reduction is obtained with 43.6° configuration which was also the case for highest C_T value.

Looking at the results, some common trends can be observed. As we increase the azimuthal separation between rotors, thrust value increases and noise value decreases. On the other side, it

Tip Mach Number = 0.523				
$\Delta\psi$ (deg.)	$\Delta\theta$ (deg.)	% C_T/σ gain at C_Q=0.008 (%)	Noise Reduction at Blade Passage Frequency (dB)	Perceived Noise Level Reduction (PNdB)
34.4	+1	6.1	-	-
43.6	+1	5.6	-	-
62.1	+1	5.5	-	-
62.1	-1	5.5	-	-
43.6	0	4.7	4	3
25.2	+1	4.4	-	-
43.6	-1	4.4	-	-
25.2	0	4.0	4	3
34.4	0	3.8	-1	0
62.1	0	2.9	-6	1
25.2	-1	2.8	-	-
34.4	-1	1.1	-	-

Table 3.1: Acoustic measurements; $\Delta\psi$ is azimuthal separation, $\Delta\theta$ is differential collective pitch between upper and lower rotor, σ is the rotor solidity
Source: Rorke [32]

is difficult to predict the azimuthal separation for maximum thrust and minimum noise because the value differs amongst many authors. Azimuthal separation at which highest performance is attained is summarized in Table 3.2 alongwith some common trends observed. Various factors play role such as number of rotors, axial distance that has been set (explained in next section), rotor blade/airfoil design, rotational speed of rotor, etc. and all these factors affect the performance of a co-rotating rotor. A major objective of this study was to investigate the effect of azimuthal separation in detail and explain the reason behind the trends observed based on flow physics, which has not been mentioned by any of the authors, so that the same reasoning can be used to predict the trend for all azimuthal angles.

Author	Azimuthal angle	Common Trend	
Landgrebe [20]	$30^o, 45^o$	Azimuthal angle $\Uparrow$	
Rorke [32]	$43.6^o, 62.1^o$		
Whiteside [40]	60^o	Thrust $\Uparrow$	Noise $\Downarrow$
Tinney [37]	$100^o - 120^o$		

Table 3.2: Azimuthal angles at which most efficient performance is obtained and common trends observed

3.3.3. Axial distance variation

Landgrebe [20] conducted one of the first investigations for axial separation too and showed that increasing the separation results in a performance benefit for the rotor, both at 60^o and 30^o azimuthal spacing. Probable reason can be a reduction in blade-vortex interaction when axial distance is increased. Due to this, induced drag on each of the blades decreases, thus, reducing torque requirement and increasing thrust produced for a particular torque applied. The performance benefits increase more at high tip Mach number and high thrust value which was also the case found with azimuthal separation trends in section 3.3.2.

A similar trend is obtained by Mahendra [5] (shown in Figure 3.10), Whiteside [40] and Ra-

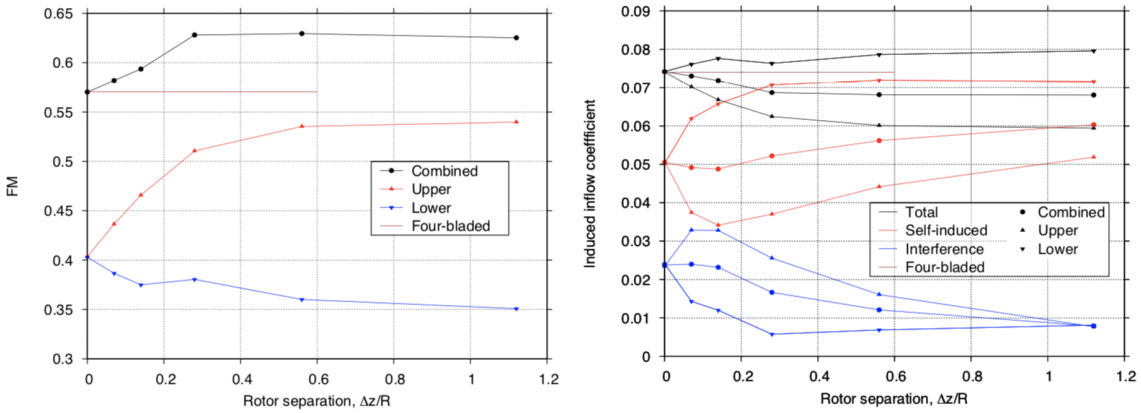

(a) Figure of Merit variation

(b) Induced inflow coefficient variation

Figure 3.10: Results for axial variation at $\Delta\phi = 90^o$
Source: Mahendra [5]

masamy [31]. Results obtained by Tinney [37] for different axial spacing are presented in Figure 3.11. The thrust contour area increases as axial distance is increased which is a similar trend as previous authors. The reason can be due to difference in blade-vortex interaction and inflow velocity on both the rotors. When axial separation is increased, the mutual interaction between the two rotors decrease, thus, the rotors are operating in a lesser undisturbed flow, ultimately increasing their performance.

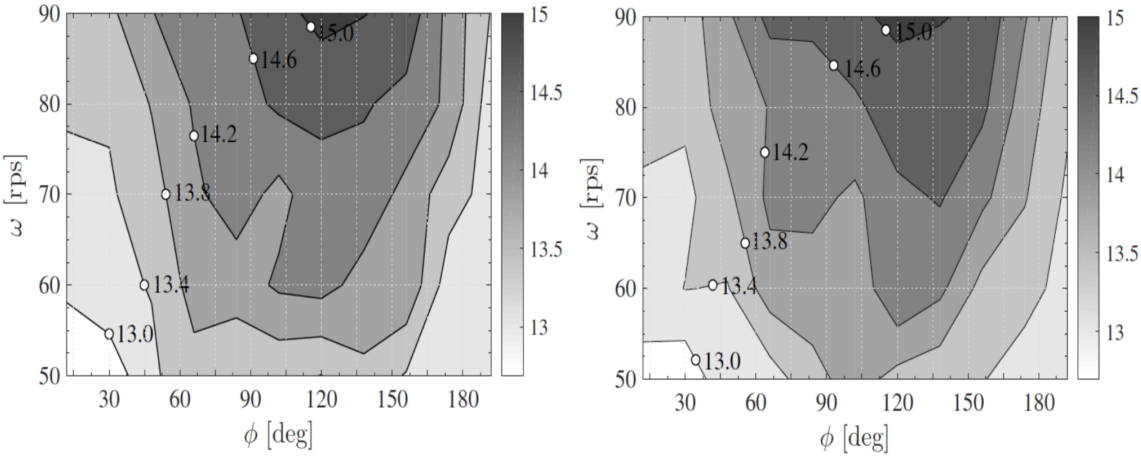

(a) $\Delta z = 1$

(b) $\Delta z = 2$

Figure 3.11: Thrust contour for different axial variation
Source: Tinney [37]

Another result is obtained by Knesnik [19] who showed that as axial distance is increased, efficiency value increases. This trend is similar to the common trends observed previously, although it also includes *forward flight* cases whereas previous results only included *hover* cases. In case of forward flight, advance/diameter ratio J (equation 3.3) is non-zero and thus performance characteristics (efficiency, thrust, power, etc.) depend on the value of J. In case of hover, advance/diameter ratio is zero and therefore, cannot be directly compared to forward flight case.

Some authors looked into aeroacoustic results too for different axial separation. Whiteside [40] showed that as axial spacing is increased, OASPL value increases at all angular positions, though

these values are less than the corresponding co-planar rotor configuration (having same number of blades as the co-rotating rotor). The increase in noise can be explained based on the second term of equation 2.9 of FWH analogy, whose contribution increases as thrust increases for higher axial separations. For all axial positions, OASPL value increases from in-plane to out of plane position which is the same trend given by Tinney [37]. Knesnik [19] showed that increasing axial distance decreases OASPL value, whose trend is opposite to the previous result. Although, Knesnik has showed results for forward flight cases while previous results were for hover cases, therefore, as explained previously about advance/diameter ratio, a direct comparison is again not possible.

Table 3.3 summarizes the common trends found till now. Comparing all the results, there can be a general agreement for aerodynamic performance that increasing axial distance increases the aerodynamic efficiency and thrust values. This trend has also been seen in case of other co-axial rotors such as contra-rotating rotors [5] [31]. There are very less results available on aeroacoustic characteristics so it is difficult to come to a general conclusion, though Table 3.3 mentions the common trends obtained by some authors (especially about hover case). One of the most important aspects lacking in the previous studies is the explanation for the results based on rotor flow physics, and this was the main motivation for the present study.

Common Trend	
Axial distance ⇑	
Thrust ⇑	Noise ⇑

Table 3.3: Summary of some common trends observed for axial distance variation

3.3.4. Differential collective pitch variation

The lower rotor affects the flow on the upper rotor (as compared to an isolated rotor) because of which angle of attack decreases ultimately leading to decrease in thrust values. Similarly, upper rotor too affects the flow on the lower rotor increasing the inflow of velocity. Thus, the lower rotor experiences a disturbed flow coming from the upper rotor. Due to different flow conditions, optimum value of collective pitch is different for both rotors. The idea is to have a differential collective pitch between them to optimize the thrust output and observe the effect on aeroacoustic characteristics.

Rorke [32] presented results for two different azimuthal positions : 43.6^o and 25.2^o and 3 collective pitch positions for each. He showed that $+1^o$ differential collective pitch position (upper rotor collective pitch 1^o higher than lower rotor) performs better than 0^o and -1^o case. The reason can be due to redistribution of vortex path and/or increased separation of the two tip path planes for that configuration. Another analysis was done by Landgrebe [20] who presented an opposite trend. The differential collective pitch was varied by $+2^o$ and -2^o. Results show that both positive and negative variation in angles have worse effect on performance characteristics as compared to baseline rotor (0^o case).

Since, not a significant amount of data is available for pitch variation, it is difficult to conclude a general trend for co-rotating rotors. Interestingly, the differential pitch values were obtained in different manner by both the above-mentioned authors. Rorke [32] increased (or decreased) the collective pitch value of upper rotor while keeping the collective pitch of lower rotor fixed. Landgrebe [20], on the other hand, varied collective pitch value of both rotors, eg. increased the value ($+1^o$) of upper rotor and decreased the value (-1^o) of lower rotor for $+2^o$ differential collective pitch value. Therefore, due to different configurations tested, a direct comparison is not fair and this can be the reason for opposite trends obtained above. The other reason can be due to difference

in scales of rotor, where former used a full scale rotor and latter used a small scale rotor. As a result, there is a difference in Reynolds number between experiments. During the present study, an investigation has been made regarding the variation in collective pitch and the role it can play in improving performance and acoustic characteristics of the co-rotating rotor.

3.3.5. Differential radius variation

Figure 3.2 (b) showed that the flow is accelerated in the streamtube when it passes through the propeller. If a second propeller is operating in the wake of first propeller, the flow experienced by the former will be different from the flow when it was operating in an isolated manner. Now, if the rotor diameter is varied so that only a part of the second rotor disk is affected by the propeller wake, it can have a difference in the overall performance and acoustics. A study was done by Nichols [28] on 3 different propeller configurations (shown in Figure 3.12) - both rotor of same diameter (a), upper rotor smaller (b) and lower rotor smaller (c). Here, upper rotor smaller means first flow is experienced by the smaller rotor and then by the larger rotor. For the experiments, APC 7×5 and APC 5×5 were used [16].

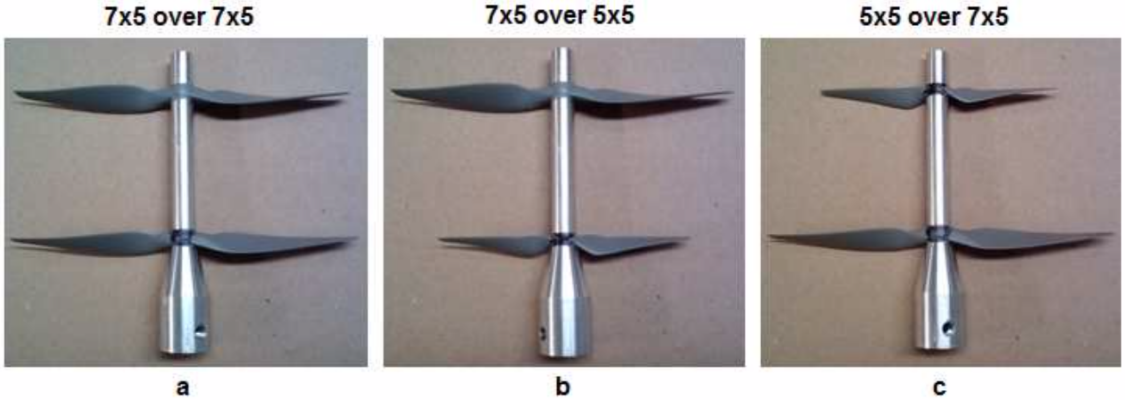

Figure 3.12: 3 different stacked rotor configurations
Source: Nichols [28]

The results show higher performance for rotors in case when upper rotor is smaller (b), as compared to other configurations and baseline 4-bladed co-planar rotor. Also, the azimuthal variation does not have a significant effect in configuration (b) as compared to configurations (a) and (c). Since the upper rotor is smaller, its wake affects only a small part of the lower rotor. Consequently, the latter is operating in a relatively more undisturbed flow, especially the rotor tip (which plays a major role both in performance and acoustics) which greatly reduces the blade-vortex interaction, increasing the overall rotor performance. For the same reason, the variation in azimuthal separation does not have a significant effect on configuration (b) as much as for configurations (a) and (c).

Landgrebe [20] conducted experiments for differential radius variation and showed similar conclusions. He also showed that combination of differential collective pitch and differential radius has further performance improvement than each of the parameters separately.

3.3.6. Summary

A brief summary of the previous studies reviewed has been presented below:

- A comparison of *co-rotating* and *contra-rotating* rotors shows that the former can perform better than the latter at certain specific configurations.

- Varying the *azimuthal angle* brings some performance and acoustic improvements but some authors mention that the effect is not as significant as other parameters. The most efficient configuration also differs amongst different authors.

- Increasing *axial distance* has performance improvement but one author mentions that acoustic characteristics is worsened. Additionally, there is a limit to axial distance due to geometry constraints.

- Two authors mentioned *differential collective pitch* results giving opposite conclusions for aerodynamics, although their method of achieving differential pitch was different.

- Increasing *differential radius* shows performance improvement when the upper rotor is smaller.

- One author showed that combination of *differential radius* and *differential collective pitch* has further performance improvement than each of the parameters separately.

3.4. Thesis Plan and Research Objectives

In the previous section, a summary of all the research work performed by previous authors was presented. In some cases, the results had an agreement whereas in some cases, the results had opposite trends or they cannot be compared due to different test conditions used. Overall, the study on co-rotating rotors lacks in various aspects. One of the major issues is that there is no explanation for why a performance variation for the rotor is being observed. Some authors have made speculation regarding the flow physics of the rotor but there is no proof provided for the same. Some comparisons have been made in terms of thrust, torque or overall noise results, but there is no explanation for the flow behaviour (velocity, pressure, vorticity, etc.) in the flow field surrounding the rotor. Additionally, there is no detailed comparison between two different configurations of the rotor (eg. two different azimuthal separations) such that the same comparison can be used to explain the behaviour in case other parameters are varied, thus, lacking a global perspective for a co-rotating rotor.

The motivation for the present study was to investigate the flow behaviour of a co-rotating rotor such that the results observed either during the study or during the literature review can be explained. This will help to look into additional parameters for the rotor which have not been explored till now and propose a new design which can show significant improvements in performance and acoustics. For the purpose, various research objectives were formulated. The thesis was divided into 3 different phases, as explained below, with each phase having its own research objectives.

Phase I - Grid Resolution study

A study was performed on the computational setup (explained in Chapter 5) of the rotor by running various simulations at different resolutions and multiple parameters were compared for convergence. The research objectives are mentioned below:

- *How much resolution is sufficient enough for an acceptable level of convergence for co-rotating rotor simulations?*

  The purpose was to find out upto what level of convergence is achieved at higher resolutions when compared to results at lower resolutions. Finally, a particular resolution was decided upon so that the results are converged and also, the computational expenses are not too high.

- *What is the accuracy of the results achieved when the result for best resolution is compared to reference literature? Is that accuracy acceptable?*

The next step in phase I was to validate the converged results for that particular configuration of the co-rotating rotor and investigate the reasons for the differences observed. The observed difference will be taken into account when performing simulations in next phases.

Phase II - Flow Physics study

Two studies were performed by varying the azimuthal and axial separation of the co-rotating rotor. The research objectives are mentioned below:

- *What is the reason for change of performance and acoustic characteristics of the co-rotating rotor when azimuthal separation is varied?*
- *What is the reason for change of performance and acoustic characteristics of the co-rotating rotor when axial separation is varied?*

  The purpose was to provide an explanation for the difference in simulation results obtained, based on flow physics of the rotor. Furthermore, a generalized theory was proposed which, in combination with the literature review, will help to predict the behaviour of the co-rotating rotor for any of its other configurations.

- *Can the lower rotor play a role of high lift device, such as flap, when operating very close to the upper rotor?*

  The idea was to increase the overall performance of the co-rotating rotor by making the lower rotor behave like a flap for the upper rotor. For the purpose, a configuration having very less azimuthal and axial separation was chosen.

- *What is the reason for difference between computational and experimental results observed?*

  While validating the computational results with experiments (in both Phase I and II), there will be some differences. The purpose was to provide the reason for those differences and check whether the differences are due to computational or experimental setup, or both.

Phase III - Quantification and Baseline study

Comparison was made to an isolated 2-bladed rotor at same rotational speed and another 2-bladed rotor with same thrust as the co-rotating rotor. The research objectives are mentioned below:

- *How much is the performance gained or lost by the co-rotating rotor as compared to an isolated 2-bladed rotor?*
- *Is it possible to quantify the difference?*

  According to the literature, there is some performance lost by each of the rotors in a co-rotating configuration as compared to an isolated rotor. The purpose was to quantify this behaviour by using both the aerodynamic and aeroacoustic data and if possible, generalize the result to predict performance of other configurations too.

- *How much is the difference in noise for a co-rotating rotor as compared to an isolated rotor producing the same thrust?*

  The purpose was to propose the idea of replacing an isolated rotor with a co-rotating configuration which will produce the same thrust but less noise. A particular co-rotating configuration was chosen from Phase I or Phase II for the purpose.

- *Can a new co-rotating configuration be proposed, which can have improved aerodynamic and aeroacoustic behaviour?*

  Based on the flow physics investigation in all the 3 phases, a new design will be studied which can have better performance than all the previous configurations.

At the end of this study, the answers to the above-mentioned research questions will be summarized and a general conclusion will be made regarding the behaviour of a co-rotating rotor.

4

Methodology

In this chapter, the methodology employed in the present study will be discussed. Initially, the methods used for fluid flow solutions in Dassault Systèmes PowerFLOW will be discussed and compared to other methods in use today, mentioning the advantages and disadvantages in each of them. The second part of chapter will deal with aeroacoustic post-processing methods employed, especially elaborating on FWH analogy and its implementation in the context of co-rotating rotor.

4.1. Computational Fluid Dynamics (CFD) solver

For every configuration that was run in all the three phases, the first step was to solve the flow field in the computational domain. For the purpose, Dassault Systèmes PowerFLOW 6-2019 was used, which employs the Lattice Boltzmann Method (LBM) to solve the unsteady flow field. In the past few decades, this method has emerged as an alternative to traditional Navier-Stokes solver. LBM is particularly suited for the present study due to its effectiveness in tackling unsteady problems because of its intrinsic low dissipation and dispersion properties [8] [25].

The next few sections will present the fundamentals of LBM, the way it has been implemented in PowerFLOW and comparison of LBM and Navier-Stokes solver, highlighting advantages and disadvantages of each of them.

4.1.1. Fundamentals of Lattice-Boltzmann Methods

The Lattice-Boltzmann Method initially developed from Lattice Gas Automata, a discrete particle kinetics solver. It can also be seen as a finite difference solver of the Boltzmann equation [11]. The kinetic theory of Boltzmann describes fluid as a composition of particles, moving with random motions and exchanging momentum and energy through the processes of streaming and collision of particles [3]. Since LBM is a discretized approach to Boltzmann theory, it restricts the particles to the nodes of a lattice. Each particle can have 9 possible directions (which includes rest too) in a quadratic mesh in 2 dimensions; this is defined as D2Q9 model. Another model named as D3Q19 has 19 possible directions in 3 dimensions. Both the models are shown in Figure 4.1.

The Boltzmann equation (eq 4.1) and its form after LBM discretization (eq 4.2) is shown below:

$$\frac{\partial f}{\partial t} + \boldsymbol{u} * \nabla f = \Omega \tag{4.1}$$

$$f_i\left(\boldsymbol{x} + c\boldsymbol{e_i}\Delta t, t + \Delta t\right) - f_i(\boldsymbol{x}, t) = \frac{f_i(\boldsymbol{x}, t) - f_i^{eq}(\boldsymbol{x}, t)}{\tau} \tag{4.2}$$

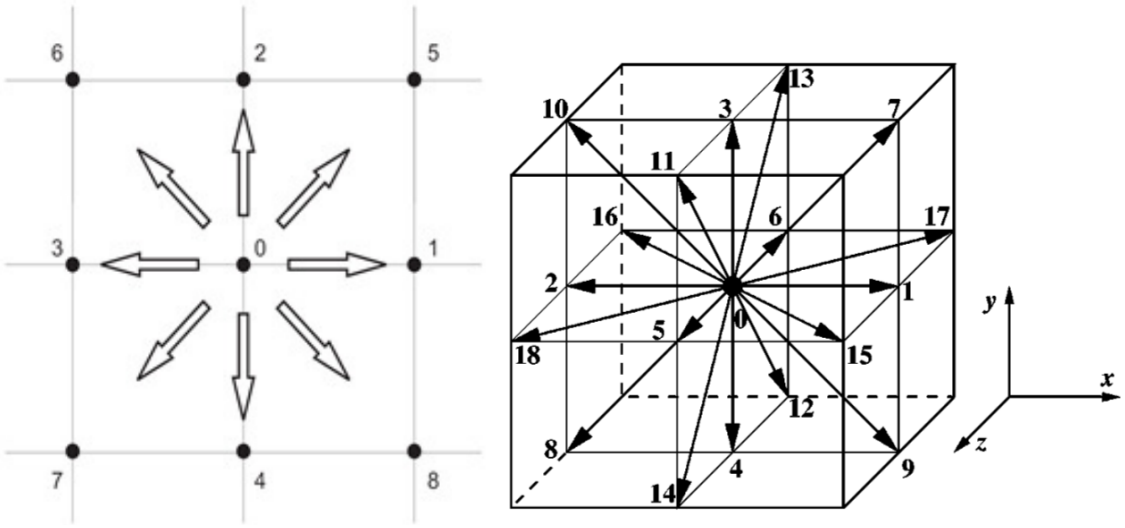

(a) D2Q9 (b) D3Q19

Figure 4.1: Discrete velocity set in D2Q9 (2 dimensions) and D3Q19 (3 dimensions) model
Source: Begum [4] and Mei [26]

where $f = f(\mathbf{x}, t)$ is the particle distribution function, $\mathbf{x}$ the position of the particle, $\mathbf{u}$ the flow velocity and Ω the collision operator. The discretized equation introduces variables such as c for the lattice speed, τ the relaxation time before reaching equilibrium, $\mathbf{e_i}$ the discrete microscopic velocity with i denoting each possible direction of the particle, ranging from 1 to 9 for 2D case and 1 to 19 for 3D case. $c\mathbf{e_i}\Delta t$ is the space increment, Δt the time increment and f_i^{eq} is the equilibrium distribution. The left hand side of discretized equation 4.2 represents the process of streaming and the right hand side represents the process of collision. In the above equation, the streaming and collision part are together in one statement but in case of solid boundaries, the two must be separated due to boundary condition being a separate collision.

In case of single phase flows, f_i^{eq} can be described through the Bhatnagar-Gross-Krook (BGK) collision model as:

$$f_i^{eq}(\boldsymbol{x}, t) = w_i \rho \left[1 + 3\frac{\boldsymbol{e}_i * \boldsymbol{u}}{c} + \frac{9}{2}\frac{(\boldsymbol{e}_i * \boldsymbol{u})^2}{c^2} - \frac{3}{2}\frac{\boldsymbol{u} * \boldsymbol{u}}{c^2}\right] \tag{4.3}$$

where, w_i are the weights [4]: in 2 dimensional case, the value is 4/9 for particles at rest (i=0), 1/9 for i=1,2,3,4, 1/36 for i=5,6,7,8, where the indices correspond to the direction shown in Figure 4.1. The macroscopic velocity and density in 2D case can be calculated from the distribution function f_i as:

$$\rho(\boldsymbol{x}, t) = \sum_{i=0}^{8} f_i(\boldsymbol{x}, t) \tag{4.4}$$

$$\boldsymbol{u}(\boldsymbol{x}, t) = \frac{1}{\rho}\sum_{i=0}^{8} c f_i \boldsymbol{e_i} \tag{4.5}$$

Algorithm of LBM

The fundamental algorithm for LBM can be summarized in 3 major steps as shown in Figure 4.2:

1. The first step is to initialize the value of $\rho, \mathbf{u}, f_i^{eq}$ and f_i. This comes from the initial condition in the first timestep shown in Figure 4.2 (a). In further timesteps, values from the previous

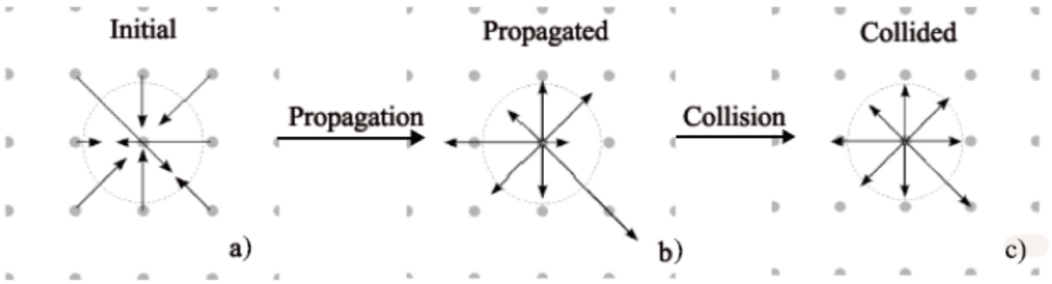

Figure 4.2: LBM algorithm steps for D2Q9
Source: Begum [4]

timestep is used and ρ and $\mathbf{u}$ are calculated using eq 4.4 and 4.5. The length of arrow in the figure represents the particle distribution function i.e. the probability for a particle to transverse in the direction of arrow.

2. In step (b), the propagation step is executed in the direction of $\mathbf{e_i}$ and a new value of distribution function f_i^* is calculated from eq 4.2, using the values at previous timestep. The new value of ρ and $\mathbf{u}$ are calculated using eq 4.4 and 4.5.

3. In step (c), the collision process is represented and a new equilibrium distribution f_i^{eq} is calculated using eq 4.3. Again using eq. 4.2, a new value of particle distribution function is calculated as:

$$f_i = f_i^* - \frac{1}{\tau}\left(f_i^* - f_i^{eq}\right) \tag{4.6}$$

The new value of f_i is then used again in step (b) to calculate macroscopic velocity and density, and the process continues.

Implementation of Boundary Conditions

In any numerical problem, boundary conditions (BCs) are employed to represent closely to the physical nature of the problem. Their implementation assumes significant importance to ensure the stability and accuracy of the numerical solution. To reflect the macroscopic BCs of the fluid, LBM makes use of two of the widely used BCs: *Bounce-back BC* [34] and *Zou-He velocity and pressure BC* [41].

- **Bounce-back BC**: This type of BC is typically used to represent no-slip boundary condition. The basic principle is that when a particle (particle distribution function) encounters a wall node, the particle is scattered back to the node where it came from, as shown in Figure 4.3 (a). Thus, the velocity at the wall is set to zero, ensuring a no-slip condition. There are two major variants of this implementation: the *on-grid* and the *mid-grid* bounce-back [34].

  The *on-grid bounce-back* implementation, shown in Figure 4.3 (a), aligns the boundary of fluid domain with the lattice points and the incoming directions of particle is reversed when encountering a boundary node. The advantage is that its implementation is smooth and the BC does not distinguish between different geometries, thus adapting easily even with complex geometries. The *mid-grid bounce-back* uses fictitious nodes and places the boundary wall between such fictitious nodes and real nodes of the fluid, and applies a collision process for the BC implementation.

  Although easy to implement, *on-grid bounce-back* is only first-order accurate due to the one-sided treatment at the boundary. On the other side, *mid-grid bounce-back* provides second order accuracy while being mildly complicated to implement.

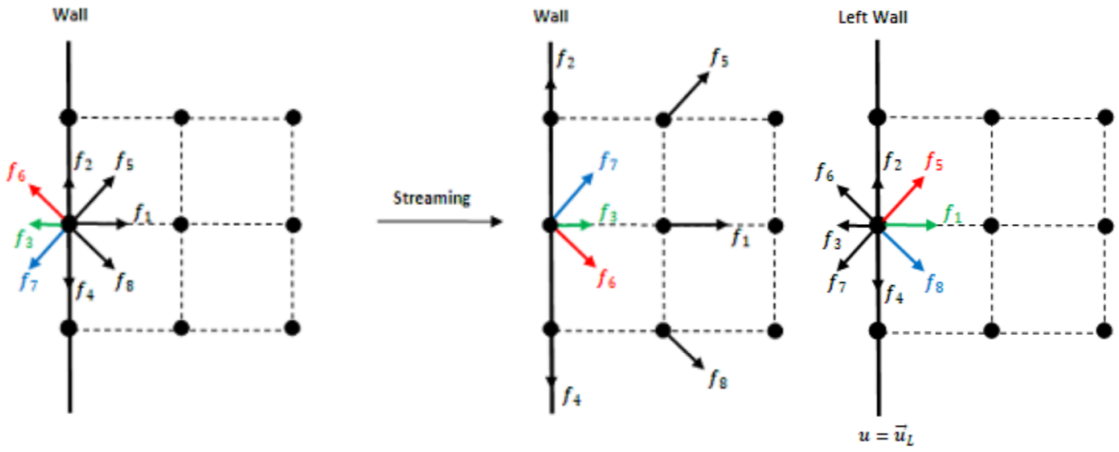

(a) Bounce Back BC (b) Zou-He BC

Figure 4.3: The two types of Boundary Conditions in LBM
Source: Bao [3]

- **Zou-He velocity and pressure BC**: In some cases, we need to implement a velocity or pressure at the boundary. The implementation was originally developed by Zou and He in 1997 [41] as shown in Figure 4.3 (b). After implementing the prescribed value at the boundary node, values of some distribution functions are known after streaming while other functions are computed using a *linear system of equations* and the *bounce-back BC*. The BC implementation depends on the orientation of geometry, thus, requires some effort to use for complex geometries.

In PowerFLOW, a turbulent wall model using the *Law of the Wall* is used to model the boundary condition, in case of high Re flows. The model implementation is as follows:

$$u^+ = \frac{1}{k}\ln\left(\frac{y^+}{A}\right) + B \tag{4.7}$$

$$y^+ = \frac{y u^\star}{\nu} \tag{4.8}$$

$$A = 1 + f\left(\frac{\partial p}{\partial x}\right) \tag{4.9}$$

where, u^+ is the non-dimensional velocity, y the vertical distance from wall, y^+ the non-dimensional wall distance, $u^\star$ the friction velocity and k=0.4 is the Von-Karman constant. The wall shear stress τ_w is then obtained and used as a wall boundary condition:

$$\tau_w = \rho\left(u^\star\right)^2 \tag{4.10}$$

Turbulence Modeling

In PowerFLOW, there are three major types of simulation methods [36]:

- **Direct Simulation**: This is especially the case for low Re flows (Re<10000). The lattice length needs to be very small to capture the smallest scales of turbulence and then, the LBM becomes equivalent to a Direct Numerical Simulation (DNS) for a Navier-Stokes solver [10]. Unfortunately, this method becomes impractical and computationally expensive for high-Re flows.
- **Laminar to Turbulent transition**: PowerFLOW uses specific physical models that helps to model laminar to turbulent transition. This is employed in case when 10000<Re<100,000.

- **Turbulence modeling**: Turbulence modeling assumes special significance especially for high-Re flows. PowerFLOW uses the commonly known Very Large Eddy Simulation (VLES) approach for Re>100,000. The turbulent kinetic energy and dissipation are calculated using the RNG form of $k-\epsilon$ turbulence model to model the subgrid scale flow properties [10]. Furthermore, as mentioned previously, it uses *Law of the Wall* to determine the local friction coefficient C_f on the boundaries.

4.1.2. LBM vs Navier-Stokes solver

Lattice-Boltzmann Method (LBM) is considered as an alternative to the traditional Navier-Stokes (NS) solvers. Therefore, it is imperative to compare the advantages and disadvantages of LBM as compared to NS solvers. The main advantages are as follows [3] [10]:

- LBM simulations are inherently stable, accurate and unsteady with a Courant-Friedrich-Lewy (CFL) value of 1
- Complex geometries and boundary shapes can be managed easily
- LBM solver can be easily parallelized, therefore, can be applied to heavy simulations
- Grid generation is semi-automatic with a very good cell quality
- LBM has intrinsically low dissipative and dispersive properties, thus, appropriate for unsteady problems like aeroacoustics

The main disadvantages of LBM are as follows:

- Less effective for steady-state flows
- LBM still needs to be extensively used for high Mach number flows (>0.4). Most of the applications up till now has been for low Mach number flows

The present study for co-rotating rotor incorporates an unsteady and low Mach number flow field and thus, considering the above mentioned points, LBM is particularly suited for getting an accurate aerodynamic and aeroacoustic result. There are no compressible effects (Mach number < 0.3), therefore, the above mentioned disadvantages do not apply to the present study.

4.1.3. Mesh creation in PowerFLOW

Lattice-Boltzmann Method (LBM) method of mesh generation is different from what is employed by Navier-Stokes (NS) solvers. In Dassault Systèmes PowerFLOW, mesh (also called as lattice) is generated in a semi-automatic manner. The whole simulation volume is divided into different lattice elements which are 3D elements in the shape of cubes, called as voxels. Near a body surface, a planar lattice is formed between the body and a voxel, known as surfel. These elements are shown in Figure 4.4 (a). The particles move from voxel to voxel; if a surfel is encountered, the boundary condition is applied.

In a computational simulation, the most important regions are near to the object in focus but the simulation volume is kept large to avoid boundary effects on the results [27]. Due to this, different resolution regions are defined; near the body, resolution is kept high while resolution farther away is kept low. In PowerFLOW, it is possible to define *Variable Resolution (VR)* regions for the purpose. The voxel size between successive VR regions increases by a factor of 2 (volume increases by a factor of 8) as compared to a higher resolution region, shown in Figure 4.4 (b). As a result, the timestep used for updating the flowfield is also scaled by a factor of 2 (coarser VR region updating every twice the number of timesteps of the finer VR region) which improves computational efficiency.

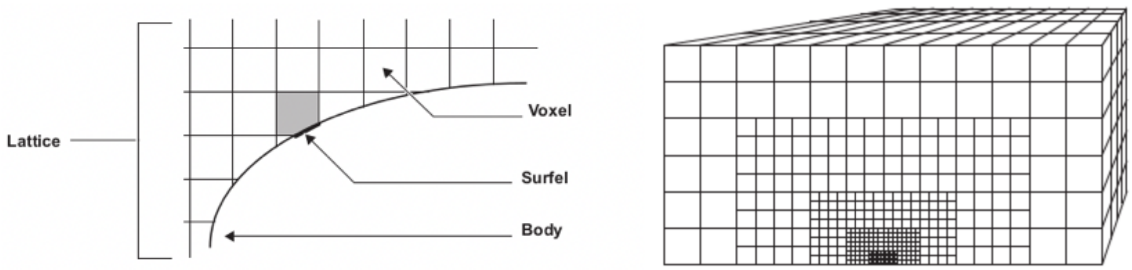

(a) Different lattice elements (b) Different VR regions

Figure 4.4: Mesh creation in PowerFLOW
Source: [36]

Therefore, it is important to have a correct number and position of VR regions which can improve the balance between computational expenses and accuracy [1]. The size of the voxel in the finest VR region is defined as the *resolution* for the case and is an important parameter for the present study, especially for the *Grid Resolution study* phase.

The present study is for a co-rotating rotor which includes a rotating body. To incorporate this into PowerFLOW, a *local rotating reference frame* (LRF) is defined which prescribes a rotational speed to the frame and this results in a different reference frame fixed to the rotating body, as shown in Figure 4.5. The LRF can either be defined as *stationary*, in case when the flow is axisymmetric and transient effects are negligible, or as *sliding-mesh*, in case when the geometry is complex and there are significant transient effects. The LRF with *sliding-mesh* has a limitation of not being able to cross in rotation 2 different VR regions. A special care was taken in the present study in this regard while deciding the size of LRF region.

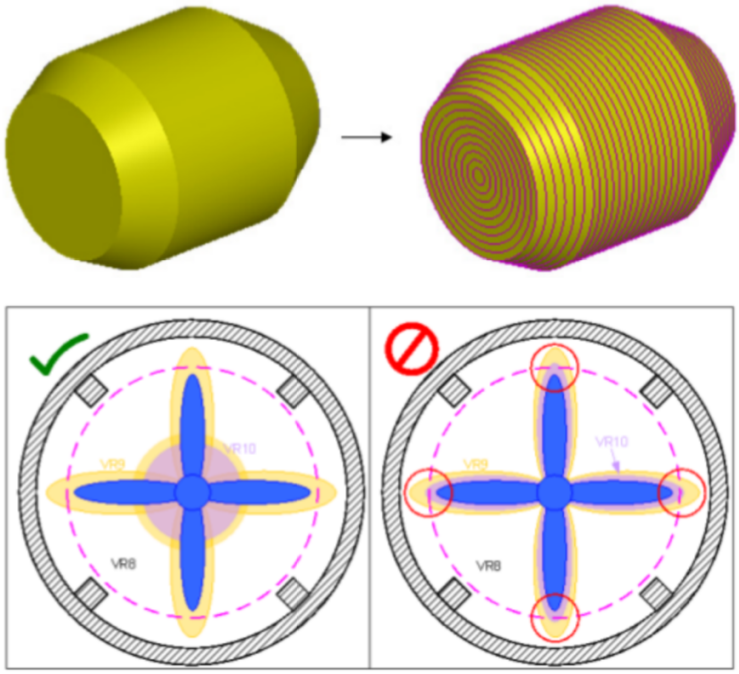

Figure 4.5: Dividing a body of revolution into rings (top) and intersection between such rings and multiple VR regions (bottom)
Source: [36]

4.2. Computational AeroAcoustics (CAA) solver

The next step, after solving the flow field, is to post-process the pressure field for getting the acoustic signature of the body. In PowerFLOW, Ffowcs-Williams and Hawkings (FWH) analogy has been implemented for the purpose, which was introduced in section 2.2.4.

4.2.1. FWH analogy implementation

FWH requires a surface over which the pressure field can be integrated to solve for the acoustic far field. This integration surface can either be solid or permeable, which are implemented as follows:

- **FWH solid integration surface**: This surface geometry matches with the boundaries of a solid body that needs to be analyzed. Only the loading and thickness noise are taken into consideration, the 2nd and 3rd term in eq. 2.9 respectively. Thus, non-linear quadrupole noise term is not included in the calculation; this is a drawback of this implementation. The advantage is that computational effort required for such calculations is low and therefore, is a compromise between accuracy and computational expense.

- **FWH permeable integration surface**: This implementation was developed by Francescantonio [13] in 1997. The surface over which the pressure field is integrated is permeable and includes the quadruple term too in the eq. 2.9. The surface is chosen large enough so that it includes all the relevant non-linearities in the flow, which gives it an advantage over solid FWH surface. However, bigger the permeable surface, more is the computational effort required in resolving the flow field near the surface. This is the due to the fact that pressure wave needs a fine resolution to accurately propagate up to the surface. Another issue is that spurious noise sources can corrupt the pressure field captured on the FWH surface. This can be due to poorly resolved structures inside the surface or due to the presence of hydrodynamic fluctuations from turbulent structures at the surface.

As mentioned previously, the present study involves low Mach number flows in which case, quadrupole noise terms have negligible contribution to overall noise. Therefore, both solid and permeable FWH methods are expected to give similar results.

In Dassault Systèmes PowerFLOW, the advanced time formulation of FWH analogy has been employed, based in the formulation 1A by Farassat and Succi [14]. The *advanced time approach* (forward time) calculates in the reference frame of noise sources. The contribution from all sources are calculated at a particular time, and this is propagated to the observer location. Consequently, different contributions reach the observer at different times due to multiple noise source locations in the flow field. The contributions are then summed up to calculate the overall noise. In another approach, known as *retarded time approach*, the contributions are evaluated in the reference frame of observer at a particular time. These contributions are emitted by multiple noise sources at different times.

The *advanced time approach* is easy to implement and efficient than the *retarded time approach*, as it does not involve iterations and can be run in parallel to perform aeroacoustic analysis with aerodynamic computations [9].

4.2.2. FWH sampling and frequency range

During an aeroacoustic analysis, there is a desirable range of frequencies to be investigated. Although the aim is to achieve as high as possible, the highest frequency value which can be sampled is given by two main criteria: *temporal criterion* and *spatial criterion*, which have been explained below. The limit defined by these two criteria is to avoid a phenomenon known as *aliasing*. Figure

4.6 shows an example of aliasing: there is an original wave (solid line), while the dots represent sampled pressure points. The discrete fourier analysis will detect the sampled points, thus, a wave with different phase and amplitude than the original.

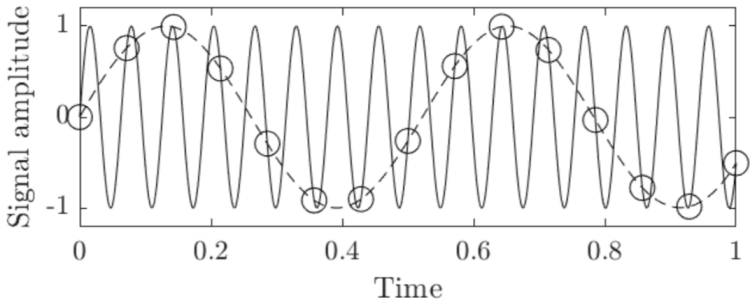

Figure 4.6: Phenomenon of aliasing
Source: Adapted from Anselmi [1]

- **Temporal criterion**: The sampling frequency f_s should be high enough to have sufficient number of points per time, to avoid aliasing. The relation is given through the *Nyquist criterion* which states $f_s \geq 2f$, where f is the highest frequency value to be analyzed.
- **Spatial criterion**: To capture an acoustic wave, a minimum of 10 voxels (10 numerical points) are needed per wavelength [33], although a minimum of 15 is advisable [39]. Thus, the resolution of VR region, in which the FWH integration surface is located, determines the maximum range of frequency which can be analyzed.

It is important to sample pressure values when the flow field has converged, thus, when the pressure fluctuations show a converged trend. During the simulations, pressure values were sampled only after the initial transient phase, which was kept as 2 full rotations of the rotor. PowerFLOW allows to seed a previous simulation file for a new simulation, so as to initialize the flowfield and decrease the transient time. For seeding, any simulation can be used although a fine simulation is generally seeded from a coarse simulation. The following criteria can be employed to choose the starting time t_{start} of the measurement file as mentioned by van der Velden [39]:

- The flow should have passed at least once throughout the whole simulation domain
- The flow should have passed the object of interest at least 10 times:

$$t_{\text{start}} = \frac{10L}{U_o} \tag{4.11}$$

  where, L is the characteristic length of body and U_o the velocity across the body
- The flow parameter for the simulation needs to have reached convergence

The present study is for a co-rotating rotor in hover. In such cases, the value of t_{start} is normally high (due to low value of U_o) as compared to forward flight cases. Therefore, hover becomes a challenging case to simulate and analyze the flowfield, especially for aeroacoustics. Time convergence for the present study has been discussed in section 5.5.2.

5

Setup

This chapter presents the computational setup employed in the present study. Initially, the coordinate systems and geometrical setup for the rotor is explained, along with the zig-zag trip and hub geometry. Then, details about different VR regions are presented, emphasizing their importance in *grid resolution phase*. The chapter concludes with some general details about the simulation and acoustic settings, and flow measurements that were obtained for subsequent analysis.

5.1. Coordinate systems

The present study includes a rotating body, thus, two cartesian coordinate systems were defined: *global coordinate* and *local (rotating) coordinate system*.

The *global coordinate system* is the default coordinate of PowerCASE setup. X-axis (red) was defined along the rotor axis, pointing towards downstream of the propeller flow field. Subsequently, Y-axis (green) and Z-axis (blue) were defined in the plane of rotor, centered between the upper and lower rotor as shown in Figure 5.8 (b) and also in Figure 5.5 (a).

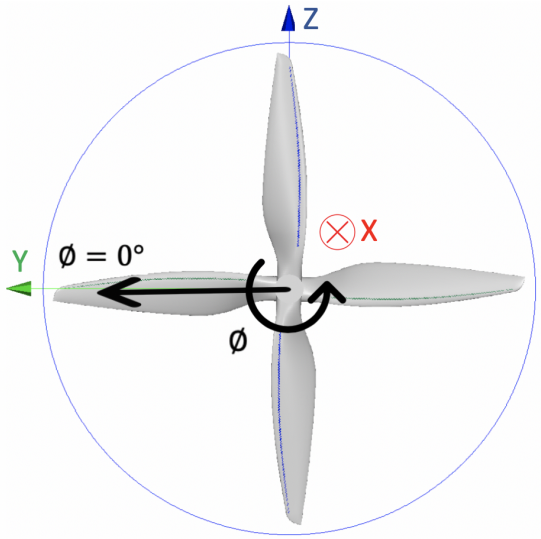

Figure 5.1: Local coordinate system with local rotating reference frame (LRF) region shown in blue outline

The *local coordinate system* was fixed to the co-rotating rotor, as a non-inertial rotating reference system. Y-axis (green) is situated along the lower rotor blade and X-axis was kept same as the X-axis

of *global coordinate system*. The coordinate is centered again between the upper and lower rotor. Figure 5.1 depicts the local coordinate system reference along with LRF region.

5.2. Geometry

5.2.1. Co-rotating rotor geometry

The Phase I and Phase II of this study involves validating the PowerFLOW results against the experimental results of Tinney [37]. The propeller used was a 2-bladed APC 18×5.5 MR, both on the upper and lower rotor. The geometry was obtained directly from *APC Propellers* along with details about its various parameters. Figure 5.2 shows the distribution for chord and twist along the span.

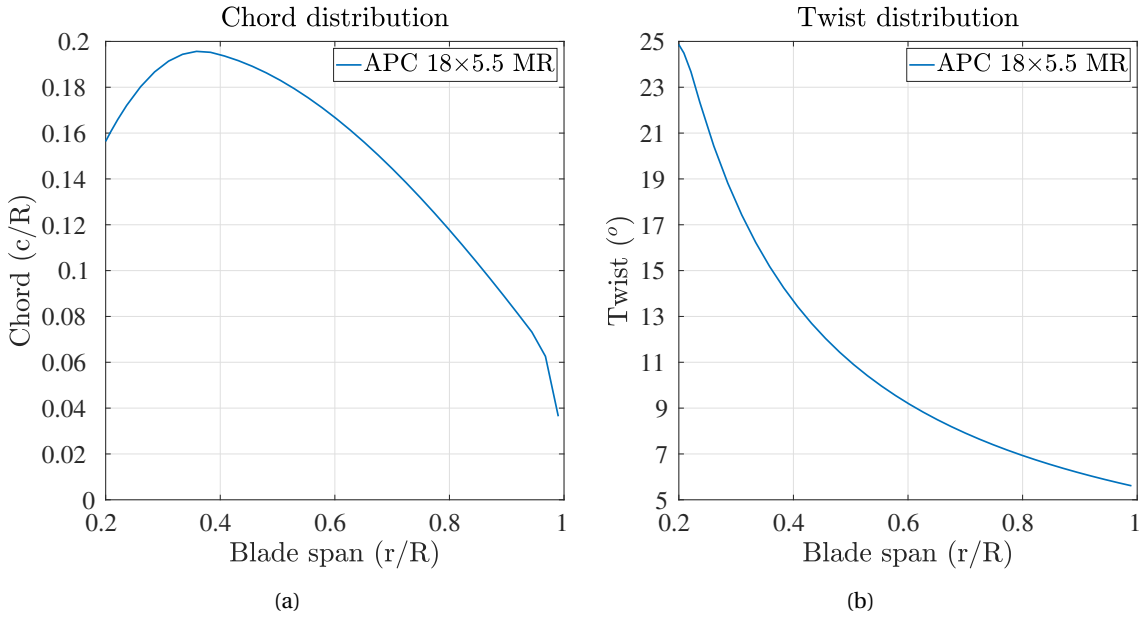

(a) (b)

Figure 5.2: APC 18×5.5 MR propeller geometrical distribution

Using an in-house tool *optydb-pfrotor*, developed by D. Casalino in the Wind Energy group, the rotor was divided into different parts known as *Face IDs* and exported as an stl file along with a table containing various rotor parameters. The stl file and the table was directly imported in PowerCASE, the software used for preparing the PowerFLOW computational setup. Dividing the blade into multiple *Face IDs* helps to allot different resolution to different parts of the geometry, as will be explained in Section 5.3. Figure 5.3 shows all the *Face IDs* on suction side of the blade which is same as on the pressure side. Table 5.1 lists the corresponding blade parts each having one unique *Face ID* along with their color shown in the figure.

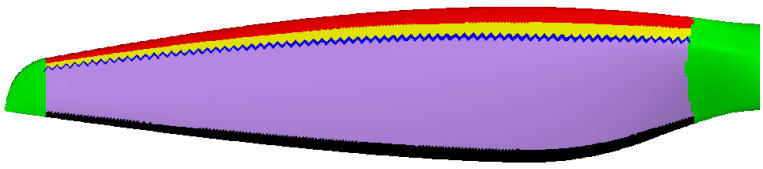

Figure 5.3: Propeller blade with different Face IDs; zig-zag trip trip shown with blue color

Figure 5.4 shows the co-rotating rotor geometry, where the two rotors are separated by an azimuthal and axial distance; these two separations varied with different rotor configurations. Table

Face ID	Leading Edge	Laminar part of blade	Turbulent part of blade	Trailing Edge	Root	Tip
Color	Red	Yellow	Purple/Violet	Black	Green	Green
Length	10%c	5%c	75%c	10%c	15%R	5%R

Table 5.1: Face IDs along with their color shown in the above figure; *c*: local chord, *R*: rotor radius

5.2 shows the list of configurations used in this study. The motivation for these specific configurations will be discussed in Chapter 6.

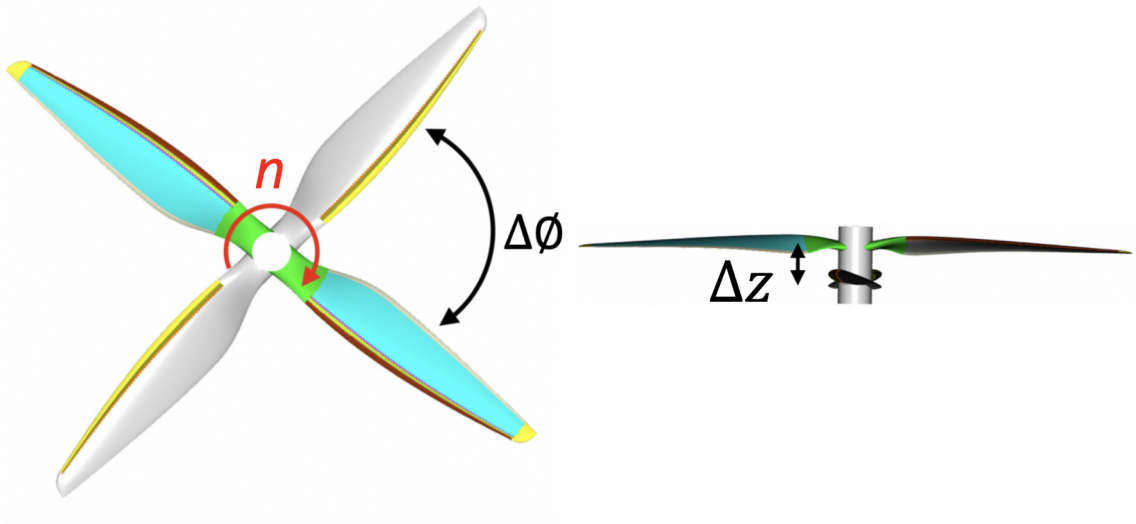

(a) Top view (b) Side view

Figure 5.4: Co-rotating rotor geometry with important geometrical parameters; upper rotor (light blue) and lower rotor (grey)

	Axial separation	***Azimuthal separation***
Phase I	1.1in (2.79cm)	84^o
Phase II	1.1in (2.79cm)	12^o
	1.3in (3.30cm)	84^o
Phase III	isolated 2-bladed rotor	

Table 5.2: Co-rotating rotor configurations used in the present study

5.2.2. Zig-zag trip

On both the pressure and suction side of the blades, zig-zag trips were added as shown in Figure 5.5. The trips were generated using the same tool *optydb-pfrotor*. Trips are commonly used to force laminar-to-turbulent transition on a blade/wing to prevent flow separation.

Trips force transition of the flow at a specific location which is known to the user. This helps to predict flow characteristics in different types of flow or applications. This is specifically important for aeroacoustic analysis where noise produced is strongly dependent on flow behaviour close to the blade surface, especially around trailing edge. Forcing the transition through trip also helps to avoid the phenomenon of artificial laminar regime that can occur in Large Eddy Simulations (LES)

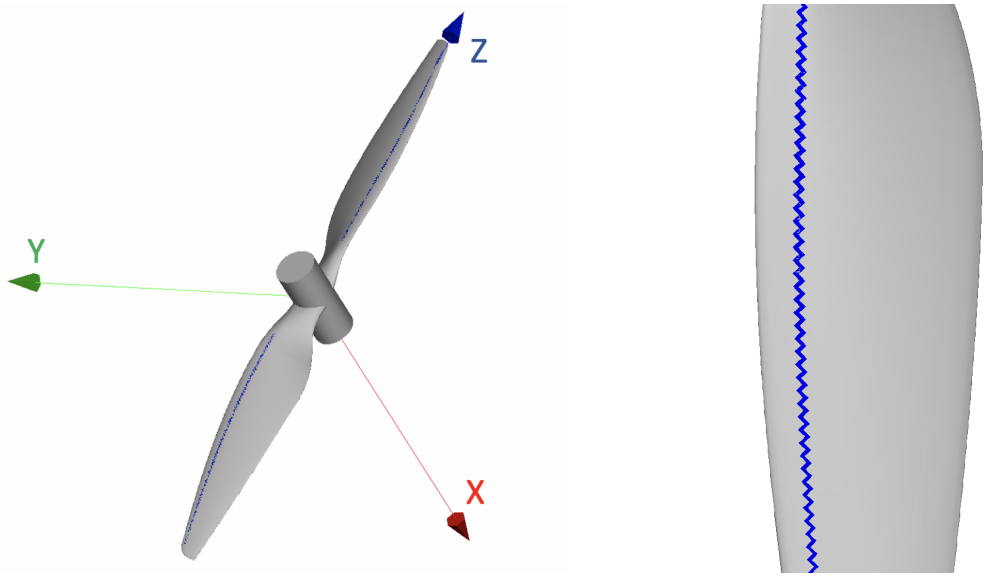

(a) 2-bladed rotor with the trip (b) Zig-zag trip on suction side (zoomed-in)

Figure 5.5: 2-bladed rotor geometry (as used in Phase III) and zig-zag trip used (blue)

[6]. LES describes the major turbulent structures directly; if such flow structures are not computed correctly, artificial separation might occur.

The trip thickness was kept at 0.06mm for all of the configurations simulated. This particular thickness was chosen so as to have minimum number of voxel thickness (in finest VR region) for resolving the trip. A thickness of 2 voxels was found enough for correctly resolving the trip, by observing the surface friction coefficient from simulation results. Below this thickness, the trip may not work properly, thus, 2 is the minimum recommended thickness; for other applications, sometimes 3 voxels thickness is preferred [1]. The y^+ value estimation for finest VR region in mentioned in Table 5.8.

Table 5.3 mentions all the parameters related to the trip, which is same on both pressure and suction side of the blade, and Figure 5.6 shows the corresponding parameters. The trip was present at 15% chord location. The relative minimum (*r_min*) and maximum radius (*r_max*) is the starting and ending point of the trip along the blade span, respectively.

Properties	***Value***	***Location***
Thickness (height)	0.06 mm	-
Chordwise location	0.15c	-
Semi-amplitude	0.02c	-
λ (wavelength)	0.08c	-
Chordwise (streamwise) thickness	0.02c	-
Relative minimum radius (*r_min*)	0.15	rH+r_min(rT-rH)
Relative maximum radius (*r_max*)	0.95	rH+r_max(rT-rH)

Table 5.3: Zig-zag trip parameters (c: local chord, R: radius of blade, rH: hub radius, rT: blade tip radius)

5.2.3. Hub

A simplified cylindrical geometry of a hub was generated in PowerDELTA, the design software of the PowerFLOW package, which was then imported in PowerCASE as an stl file. Figure 5.4 shows the

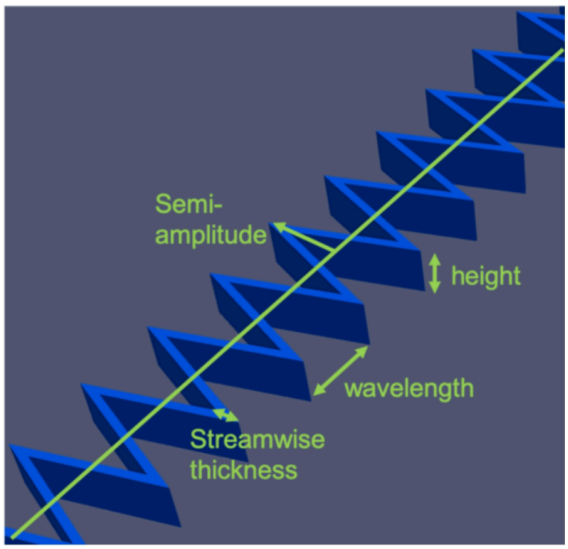

Figure 5.6: Zig-zag trip parameters
Source: D. Casalino, TU Delft

hub geometry along with the rotor blades. Table 5.4 mentions the parameters of hub geometry. A length of 2.5in (6.3cm) and a diameter of 1.1in (2.8cm) was kept so as to avoid any change of hub geometry when azimuthal or axial separation is varied. This will make sure that the difference in performance between two configurations is not due to hub but due to rotor flow physics. The hub was kept the same even in case of isolated 2-bladed rotor simulation (Phase III) due to the above mentioned reason.

Diameter	***Length***
1.1in (2.8cm)	2.5in (6.3cm)

Table 5.4: Hub geometrical parameters

5.3. Variable Resolution (VR) regions

In a computational setup, there are boundaries present on the edge of the domain, which are not present in real flight environment. Consequently, there are differences obtained in flow field results between the former and the latter. To avoid such disparity in the present study [27] and make the results as close to free flight performance, the simulation domain was kept relatively large. Table 5.5 mentions the size of simulation domain for different resolutions.

A total of 19 VR regions were defined, the names of which are given in Table 5.6. The finest one is VR15_pr and coarsest one is VR0b; 'pr' is used for all VR regions which are constructed as an offset from the propeller blade surface. A separate VR region was defined for blade tip to increase its resolution even further. This was considered necessary due to the significance of blade tip in rotor flow physics, especially aeroacoustics.

Phase I of the present study involved running various resolutions for a particular configuration. As a result, voxel size vary for different resolutions for each VR region, which is listed in Table 5.7. The computational expense for a simulation is decided by a parameter known as *fine equivalent voxels*, which is calculated based on total number of voxels in each VR region, as:

Resolution	Size of simulation domain (m^3)
Very Coarse	161×161×161
Coarse	113×113×113
Medium	81×81×81
Fine	57×57×57

Table 5.5: Size of simulation domain for different resolutions

Location	***VR***
Blade surface	VR15_pr, VR14_pr, VR13_pr, VR12_pr
Blade tip	VR12_torus
Flow volume	VR11, VR10, VR09, VR08, VR07, VR06, VR05, VR04, VR03, VR02, VR01, VR00, VR0a, VR0b

Table 5.6: List of VR regions and their corresponding locations (mentioned in order of decreasing resolution)

$$\begin{aligned}\textbf{Fine equivalent voxels} = &\mathbf{N}(\text{finest scale}) + \mathbf{N}(\text{2nd finest scale})\ /2 + \\ &\mathbf{N}(\text{3rd finest scale})/4 + \mathbf{N}(\text{4thfinest scale})\ /8 + \ldots + \\ &\mathbf{N}(\text{coarsest})/(\ 2\text{^}(n \text{ grid levels- } 1)\ )\end{aligned} \tag{5.1}$$

where, N is the total number of voxels in a particular VR region. Table 5.7 mentions the *fine equivalent voxels* for each resolution. The simulations were run for a total of 0.16 sec (8 rotor rotations: 2 transient + 6 sampling). Due to unity CFL condition, the number of timesteps for such duration varied too for each resolution and are mentioned in Table 5.7. Total CPU hours for *Very Coarse* was 9818 and for *Coarse* was 41906.

Resolution	**dx_15 (m)**	**dx_14 (m)**	**dx_0 (m)**	**dx_0b (m)**	**Fine equivalent voxels (millions)**	**Timesteps**
Very Coarse	7.60e-5	1.52e-4	2.49	9.96	14	1655510
Coarse	5.35e-5	1.07e-4	1.75	7.01	38	2350824
Medium	3.80e-5	7.60e-5	1.24	4.98	75	3311020
Fine	2.68e-5	5.36e-5	0.88	3.52	153	4685093

Table 5.7: Voxel size in some of the VR regions, fine equivalent voxels and number of timesteps for a run time of 0.16 sec, for different resolutions

5.3.1. Location and Shape of VR regions

Blade surface

The surface of the blade is the most important location in the whole simulation domain and the quality and accuracy of flow calculation around the surface will determine the quality and accuracy of the entire flow field. For this reason, a total of 4 VR regions are defined wrapping around the blade as an offset from the surface, with the finest region being closest to the surface. Table 5.8 mentions the location of such VR regions while Figure 5.7 shows the shape of VR14_pr (2nd finest). All 4 VR regions are separated by 4 voxels thickness (starting from blade surface) which was decided based on the comparison of results with 8 voxels thickness in the beginning of the study. No difference was found between the results, making 4 voxels thickness a very good compromise between computational expenses and accuracy. Table 5.8 also mentions the y^+ value until which each of the VR regions resolves the flow, calculated from the *Blasius* estimation for a flat plate boundary layer [30].

VR	*Location*	offset from blade surface (m)	y^+ value
VR15_pr	zig-zag trip, blade tip	1.52e-4	18.2
VR14_pr	zig-zag trip, all Face IDs except root	4.56e-4	54.6
VR13_pr	zig-zag trip, all Face IDs except root	1.07e-3	128.1
VR12_pr	zig-zag trip, all Face IDs, hub	2.28e-3	272.9

Table 5.8: VR locations around the blade surface, their offset and y^+ estimation at mid-span position

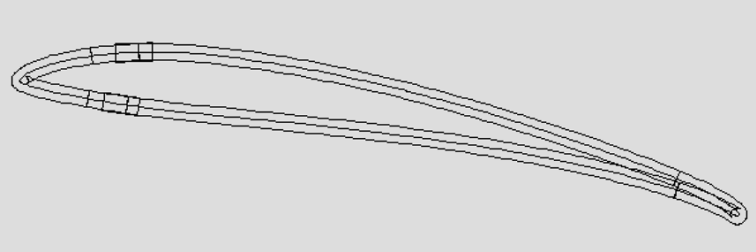

Figure 5.7: Cross-section of propeller blade showing VR14_pr

Blade tip

Figure 5.8 shows the VR12_torus shape which is created as a fitted *Volume of Revolution* around upper and lower rotor blade tip. The resolution of VR12_torus is same as VR12_pr and is situated at an offset of 4 voxels thickness (4*dx_12) from the blade tip. (dx_12 is voxel size in VR12_pr)

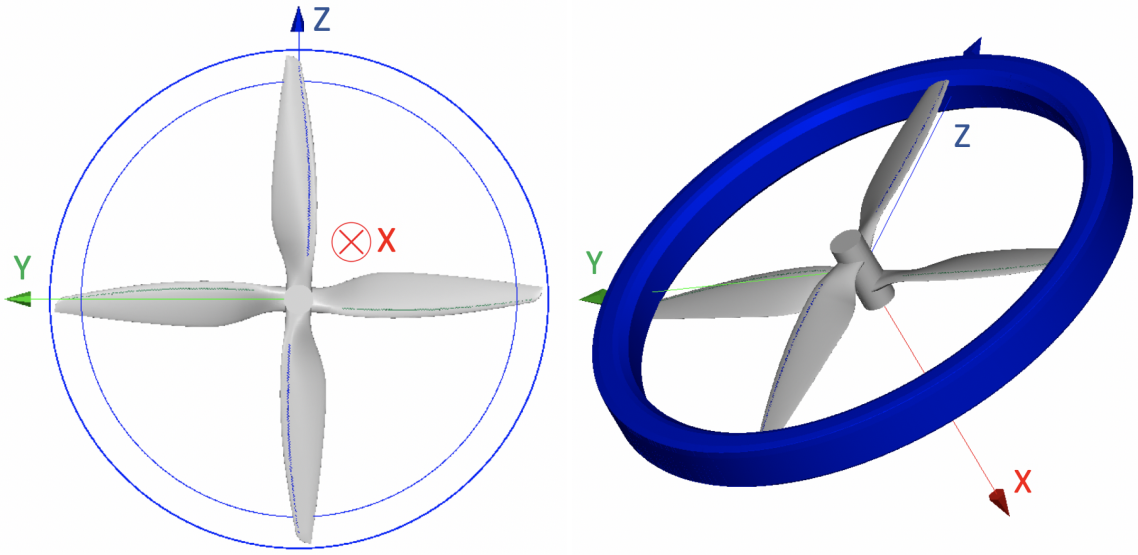

(a) Top view (blue outline)

(b) Orthogonal view (blue solid) showing VR12_torus shape

Figure 5.8: VR12_torus location and shape, wrapping around the blade tip circular path

Near the rotor

Figure 5.9 (a) shows separate regions near the rotor.

- The innermost region is LRF_pr (blue) which is the rotating region containing the rotor. LRF_pr was kept slightly inside VR11 with a gap of 2 voxels thickness (2*dx_11). This was done to en-

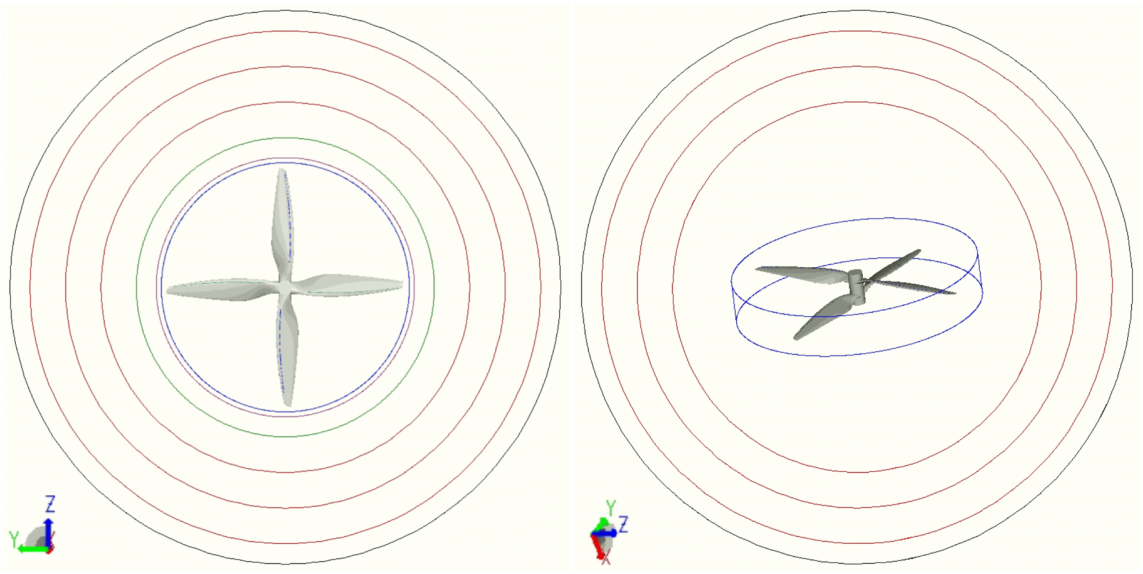

(a) Top view

(b) Orthogonal view showing cylindrical shape of LRF_pr, similar to VR10 and VR11

Figure 5.9: Top and Orthogonal view of flow domain and different regions

sure that the rotating region does not intersect with 2 different VR regions, as was explained in section 4.1.3.

- Going outwards from LRF_pr, next region is VR11 (purple) which is a cylindrical *Volume of Revolution* region containing the co-rotating rotor geometry. It is situated at an offset of 24 voxels thickness (24*dx_11) from the rotor.
- Next region is VR10 (green) which is again cylindrical in shape. The radius of cylinder is kept as 1.25**propeller radius* with thickness equal to *propeller radius*.
- Next regions are FWH_prm1, FWH_prm2, FWH_prm3 (red) which are spherical FWH permeable integration surfaces. These will be discussed in Section 5.4.
- Next region VR09 (black) is also spherical in shape and situated at a distance of 8 voxels thickness (8*dx_9) from FWH_prm3.

Far away from the rotor

Figure 5.10 (a) shows VR regions situated further away from the rotor. Starting from VR09 and moving radially outward, the regions are - VR08, VR07, ..., VR01, VR00, VR0a, VR0b. All VR regions are spherical in shape except the outermost VR0b which is cubic in shape. Each region is separated by 4 voxels thickness from each other. Since voxel size decrease with increase in resolution, the simulation domain size varied for different resolutions with smaller domain being associated with higher resolutions. This is shown in Table 5.5.

5.3.2. Modification for Grid resolution study

During the early stages of the study, the simulations were expensive to operate especially for the *Medium* and *Fine* case. The *grid resolution* phase was then expanded to include 2 new case setups - C2 and C3 (C1 is the original case) and mesh convergence was performed on each of them. The purpose was to reduce computational cost without affecting the aerodynamic and aeroacoustic results.

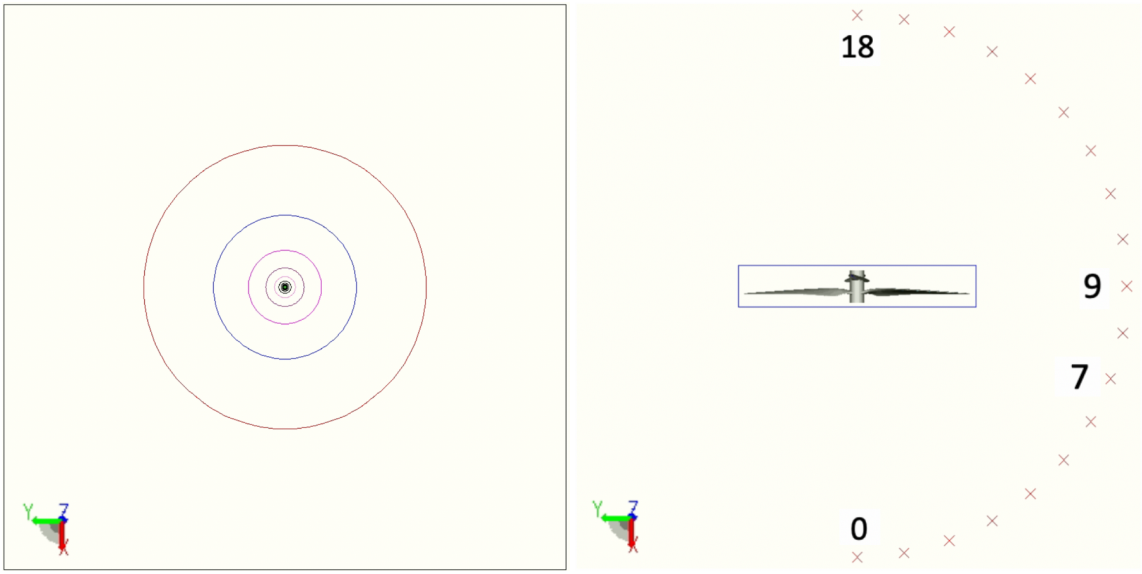

(a) Outer VR regions

(b) Location of microphone probes with important probe numbers

Figure 5.10: Outer VR regions and acoustic settings

Looking at equation 5.1, number of voxels in a finer region is more important than in a coarser region. To reduce *fine equivalent voxels*, VR14_pr was modified as shown in Figure 5.11, as compared to Figure 5.7. Table 5.9 mentions the reduced computational cost for C2 and C3 and the location of VR14_pr for each case. The results for all 3 case setups are discussed in Section 6.1.

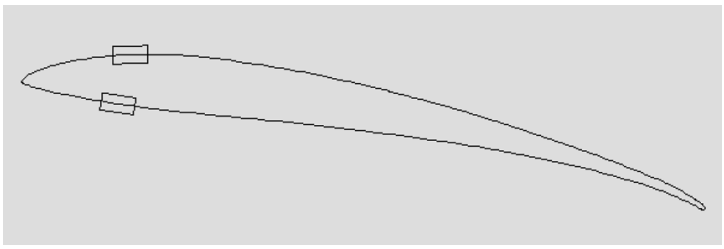

(a) C2 case

(b) C3 case

Figure 5.11: VR14_pr location around propeller blade

Case setups	Vcoarse	*Coarse*	*Medium*	*Fine*	*Location of VR14_pr*
C1	14	38	75	153	zig-zag trip, all Face IDs except root
C2	9	18	35	68	zig-zag trip, blade tip
C3	12	23	44	-	zig-zag trip, blade tip, LE, TE

Table 5.9: Millions of fine equivalent voxels and location of VR14_pr in each case

5.4. Acoustic settings

Apart from aerodynamic performance, reducing noise was an additional objective in the present study. For the purpose, far field analysis was performed by employing both the solid and permeable Ffwocs-Williams and Hawkings (FWH) formulation.

Solid FWH

The solid FWH surface was kept on the blade surface including all the *Face IDs*, *zig-zag trip* and the *hub*. The sampling frequency was set as 40000 Hz based on the spatial and temporal criterion mentioned in Section 4.2. FWH solid formulation also helped to separate the upper and lower rotor contribution at a particular point in the flow field, as will be shown in Chapter 6.

Permeable FWH

The permeable FWH surfaces are shown in Figure 5.9 as 3 red spherical surfaces. They were kept between VR10 and VR09 and separated by 14 voxels thickness (14*dx_9) from each other. The main purpose to use 3 FWH surfaces instead of just 1 was to remove any hydrodynamic fluctuations which might be present in the flow field. This was done by averaging the contribution from all 3 surfaces during far field analysis. The sampling frequency was kept as 40000 Hz. Based on spatial criterion, the cutoff frequency for permeable FWH comes out to be lower than solid FWH, due to larger voxel size in the former. Table 5.10 lists the cutoff frequencies for 3 different resolutions used. The noise spectra results were subsequently analyzed below the cutoff frequencies.

For all noise spectra, frequency resolution was kept as 10 Hz.

Resolution	Cutoff frequency
Very Coarse	4654 Hz
Coarse	6608 Hz
Medium	9290 Hz

Table 5.10: Spatial criterion cutoff frequency for permeable FWH based on voxel size of VR09 for each resolution

Microphone probe positions

To compare the results for solid and permeable FWH, a total of 19 microphone probes were placed at various locations in the flow field, as shown in Figure 5.10 (b) which also mentions the probe numbering as has been used in the study. Eg. probe 9 is located in rotor plane and probe 7 is located out-of-plane. The radial location was kept at 4 voxels thickness (4*dx_9) outside of VR_09. This was done to ensure that microphones were not kept too close to the FWH permeable surfaces and still be located in a sufficiently fine region for a good sampling accuracy.

The sampling frequency was kept as 1/timestep Hz, where each timestep varied between different resolution. Total number of timesteps are mentioned in Table 5.7. The results will be discussed in Section 6.3.

5.5. Global simulation parameters and characteristics

PowerFLOW defines a number of global parameters for running a simulation. These characteristic parameters are used by PowerFLOW to non-dimensionalize the data obtained while post-processing either aerodynamic or aeroacoustic results. Table 5.11 mentions a list of them. Other thermodynamic parameters are mentioned in Table 5.12. Each simulation duration was 0.16 sec with a rotational speed of 50 rps. The Reynolds number (Re) was 1.69e5 at the mid-span of the rotor blade.

For all simulations, *default turbulence intensity* was kept at 0.1% and *default turbulence length scale* was kept as 1 mm. *Maximum expected Mach number* was kept as 0.95 which specifies the maximum Mach Number that can be expected to be encountered in the case [35]. The value is normally kept high because the simulation results may become unreliable if Mach numbers during a simulation significantly exceed the specified *maximum*, although it also increases the number of timesteps to simulate a physical time.

Characteristic Parameters	**Value**	**Reason**
Pressure	101325 Pa	Atmospheric pressure at sea level
Velocity	0.05 m/sec	Freestream velocity
Temperature	288.15 degK	Standard temperature of 15^{o}C
Viscosity	1.46e-5 m^2/sec	Standard viscosity of air
Length	30.45 mm	Average propeller chord length
Area	0.16 m^2	Rotor swept area (πR^2)

Table 5.11: Characteristic parameters

Thermodynamic Parameters	**Value**	**Reason**
Gas molecular weight	28.96 kg/kmol	Average molar weight of air
Gas specific heat ratio	1.4	Standard value for air
Constant-pressure specific heat	1004.7 J/(kg*degK)	Standard value for air
Fluid Prandtl Number	0.707	Standard value for air

Table 5.12: Thermodynamic parameters

5.5.1. Boundary Conditions

The whole simulation domain is divided into three types of Boundary Conditions (BCs) which are explained below. Table 5.13 mentions a list of parameters used for BCs.

- The face upstream of the rotor and the 4 faces parallel to the rotor axis are defined as **pressure and velocity inlet**. The pressure value is standard atmospheric pressure and freestream velocity is kept very low, 0.05 m/sec. This is due to the fact that simulation is for hover case and a value of 0.05 m/sec is very low so that forward flight effect can be neglected (*advance/diameter ratio* is 0.002). Taking a value of 0 m/sec posed numerical problems due to initialization of velocity in the domain. Thus, the domain was initialized with 0.05 m/sec. The turbulence intensity and length scale was kept as default.
- The face downstream of the rotor was defined as **pressure outlet** with free flow walls and, static pressure value as standard atmospheric pressure.
- The solid blade surfaces were defined as standard adiabatic **walls** (no-slip), with roughness value of 0 mm.

Parameters	Value
Freestream velocity	0.05 m/sec
Freestream Mach number	1.47e-4
Rotational speed	50 rps (314.16 rad/sec)
Surface roughness	0 mm

Table 5.13: Parameters used for boundary conditions

5.5.2. Time convergence

As mentioned in section 4.2.2, time convergence is an important criteria especially in hover case. For the purpose, the criteria mentioned by van der Velden [39] in section 4.2.2 were checked for various cases. Table 5.14 shows the calculation for one of the criteria ($t_{\text{start}} = \frac{10L}{U_o}$) based on results for Phase I configuration. The criterion is easily satisfied for the case.

Parameters	L (average thickness of blade)	U_o (average axial velocity at the rotor plane)	t_{start} (calculated)	t_{start} (PowerFLOW)
Value	0.0218 m	5.4192 m/sec	0.0402 sec	0.04 sec (2 rotations)

Table 5.14: Time convergence criteria for flow simulations

Figure 5.12 shows time convergence for two of the most important parameters, non-dimensionalized *thrust* of rotor and *pressure fluctuations* (at a point situated 3× *rotor diameter* from the rotor axis in the rotor plane). The values have converged even before 2 rotations (0.04 sec) which was kept as the transient time for all simulations. The fluctuations in mean *thrust* and mean *torque* value was found to be 0.22 % and 0.16% respectively, which can be considered as a very good level of convergence.

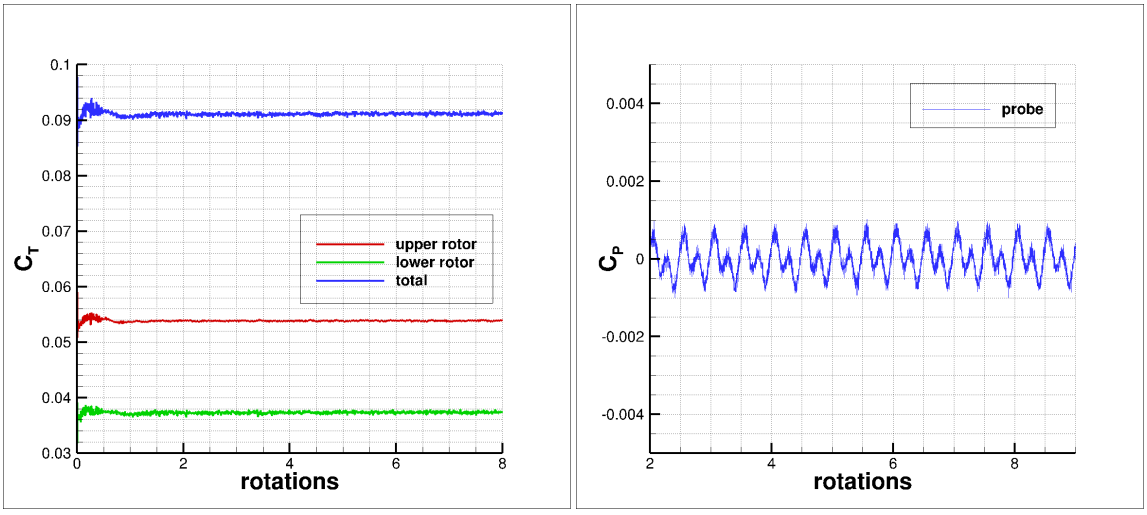

(a) Thrust convergence

(b) Pressure convergence

Figure 5.12: Time convergence for both aerodynamic and aeroacoustic parameters; $C_T = \frac{T}{\rho n^2 D^4}$, $C_P = \frac{P - P_{mean}}{0.5 \rho v^2_{0.54R}}$

Therefore, the above two mentioned convergence criteria were satisfied which was sufficient enough to post-process the data for further analysis.

5.5.3. Flow field and acoustic measurements

A number of flow parameters were saved during and after the simulation. The data was further used for post-processing in PowerVIZ and PowerACOUSTICS. Since the size of data saved is of the order of 100s of GB (or 1-2 TB), only specific part of the domain was used to save the data. All the parameters while post-processing were non-dimensionalized with respect to a reference value. A list of all non-dimensional parameters and reference value used are mentioned in Appendix A.

PowerFLOW saves data every 2^{n-1} timesteps for every n^{th} VR region, where *n=1* is the highest resolution VR region. Table 5.15 summarizes the type of data saved along with the domain utilized for it. The listed measurement files were collected in every simulation run during the study.

Measurement	**Region**	**Sampling frequency (Hz)**	**Parameters sampled**
Mean flow	Red cylinder	50 (every rotation)	Pressure, Velocity, Vorticity, Density
Transient flow	Blue cylinder	72000 (every 0.25^o of rotation)	Pressure, Velocity, Vorticity, Density
FWH permeable	FWH surfaces	40000	Pressure
FWH solid	Blade surface	40000	Pressure
Forces	Blade surface	2.58e6	Forces, Moments

Table 5.15: Measurement data saved and its corresponding region in the flow field

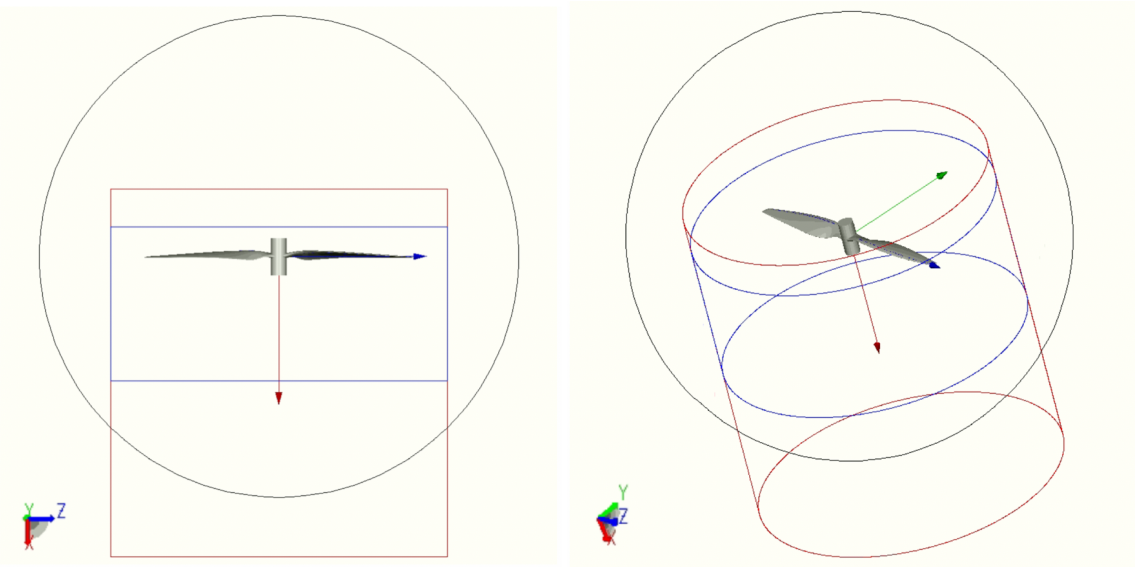

(a) Side view (b) Orthogonal view

Figure 5.13: Domain utilized for measurement files; mean flow (red) and transient flow (blue) domain with VR09 (black) is shown

- *Transient flow* data was saved in the blue cylindrical region shown in Figure 5.13. The radius of the cylinder was same as VR10 while the two ends varied between -50mm to 210mm. The data was saved for only 1 rotation after the flow was converged. Transient files are used to study the instantaneous properties of the flow field which helps to highlight the important phenomenon occurring for the rotor.
- *Mean flow* data was saved in the red cylindrical region shown in Figure 5.13. The radius of the cylinder was same as VR10 while the two ends varied between -114mm to 508mm. Mean flow

averages the data over 1 rotation and saves it at the end of each rotation, after the flow has converged. Averaging helps to remove fluctuations in the data and gives a different perspective of the flow field, as compared to *transient flow*.

- *FWH* permeable and solid files were saved for aeroacoustic post-processing as explained in Section 5.4.
- *Force* and *moment* data were saved at the solid blade surfaces which was then used to analyze and compare the thrust and torque output for different configurations.

5.6. Reference experimental setup

In the phase I and II, aerodynamic and aeroacoustic results were validated with the experimental results obtained by Tinney [37]. In case of aerodynamics, only thrust results were available. The uncertainty error due to repeatability was calculated to be 0.8 N, which was found from the difference in repeated thrust measurements of the same co-rotating configuration. This error has been shown in the thrust convergence results in Figure 6.1 (a) in Chapter 6.

The rotor noise was measured at the locations shown in Figure 5.14 with the corresponding probe number 1-8. Probe 2 is the in-plane probe with respect to the rotating plane of the upper rotor, while others are out-of-plane. The exact location of each probe is mentioned in Table 5.16. The probes were kept at 3× *rotor diameter* (54 in) from the rotor axis.

Figure 5.14: Location of pressure probes in the experimental setup for validation
Source: Tinney [37]

Probe	X (in)	X (m)	Y (in)	Y (m)	Z (m)
1	-9.55	-0.2426	54	1.3716	0
2	-0.55	-0.0139	54	1.3716	0
3	8.45	0.2146	54	1.3716	0
4	17.45	0.4432	54	1.3716	0
5	26.45	0.6718	54	1.3716	0
6	35.45	0.9004	54	1.3716	0
7	44.45	1.1290	54	1.3716	0
8	53.45	1.3576	54	1.3716	0

Table 5.16: Measurement probe locations
Source: Tinney [37]

6 Results

The results corresponding to different computational setups (as mentioned in Chapter 5) are presented in this chapter. The chapter is divided into different sections, each corresponding to a particular rotor configuration. Initially, the grid resolution study is presented. The baseline 2-bladed rotor results are discussed thereafter, which will be used in subsequent sections to explain the flow physics of the co-rotating configurations. Each section discusses both the aerodynamic and aeroacoustic results, while also validating against experimental results, if possible. At the end of each section, a conclusion is made regarding the understanding of flow physics of the co-rotating rotor based on which the configuration of next section is decided upon. The chapter ends with quantification of different flow phenomena found during the study.

6.1. Grid Resolution study

A total of 3 different computational setups were studied in which VR14_pr region was varied as shown in Figure 5.11 in Chapter 5. Table 6.1 lists all the geometrical parameters corresponding to the rotor configuration and Figure 5.4 shows the rotor geometry. Table 5.9 lists down all the setups and resolutions studied in this phase with their corresponding number of fine equivalent voxels.

$\Delta\phi(^o)$	Δz (in)	n (rps)	D (in)	hub length (in)
84	1.1	50	18	2.5

Table 6.1: Geometrical parameters for grid resolution study

6.1.1. Choice of C1 over C2 and C3

Figure 6.1 shows the convergence results for *thrust* and *torque* obtained for all 3 configurations. In case of thrust, results are also compared with experimental result (no experimental torque results were present). The dotted lines in thrust plot represents the uncertainty error in experiments.

In case of any resolution study, an expected trend is of a converged plot as resolution increases. For convergence, a tolerance of 2% is taken. Looking at the Figure 6.1, following conclusions can be made:

- **C1** (Red): Results show convergence after *Medium* resolution
- **C2** (Green): Results did not show convergence even after running for 4 different resolutions. A sharp change in values is observed for *Medium* case

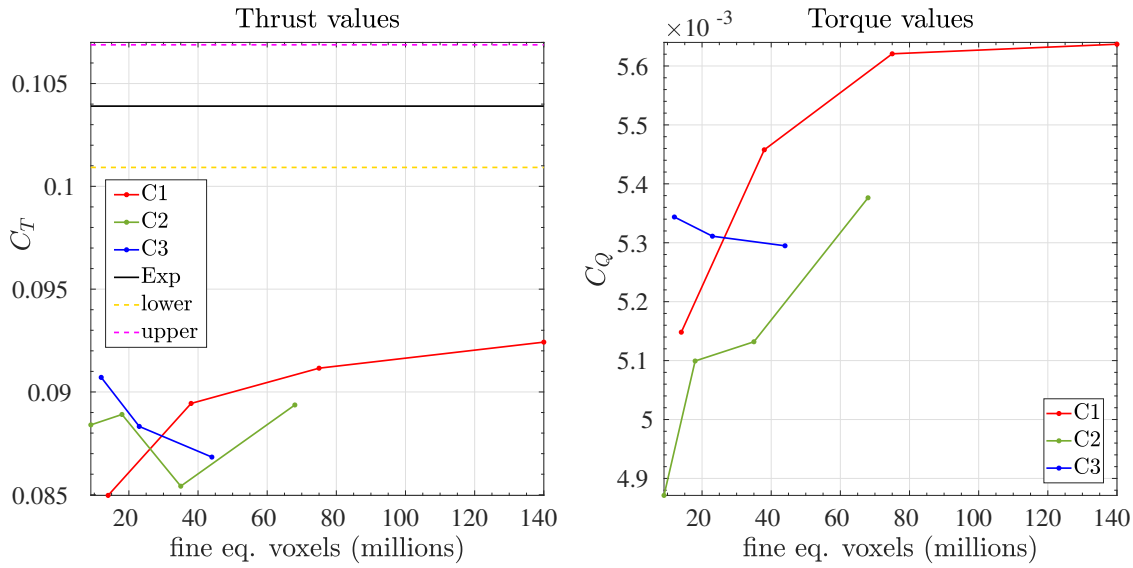

(a) Thrust convergence

(b) Torque convergence

Figure 6.1: Convergence results for all configurations

- **C3** (Blue): Results show convergence for initial 3 resolutions though the values were farther away from experimental result, as compared to C1 case

Thus, C2 case was rejected due to lack of convergence and C3 case, although showed trends for convergence, was rejected due to higher difference of thrust values from the experimental result. C1 case was finally selected for further analysis. This proves that resolution of the whole blade is important so as to achieve correct numerical results.

There are some differences between PowerFLOW and experimental result, the reasons for which will be discussed in the next few sections.

6.1.2. Choice of Medium over other resolutions

To decide a particular resolution for C1 configuration, various parameters were analyzed, both performance and acoustic. From Figure 6.1, the correct choice would be *Medium* case with 75 million fine equivalent voxels because the change in thrust and torque values between *Medium* and *Fine* case is less than 2%. To justify this choice, convergence study was performed on other parameters too, which are mentioned in the next few pages.

Aerodynamic analysis

In this section, aerodynamic parameters are analyzed such as spanwise thrust distribution and individual rotor thrust and torque.

Spanwise thrust variation

Figure 6.2 presents result for spanwise variation of thrust coefficient (C_T) for upper and lower rotor. It can be observed that values for Coarse and Medium case are much closer to each other than Vcoarse case which supports the final choice for Medium case.

Individual rotor performance

Figure 6.3 and 6.4 compares upper and lower rotor thrust (C_T) and torque (C_Q) values, for different resolutions. The plots are made for a total of 8 rotations to depict that values were converged before 2 rotations, which was kept as the transient time for all simulations. The comparison of different

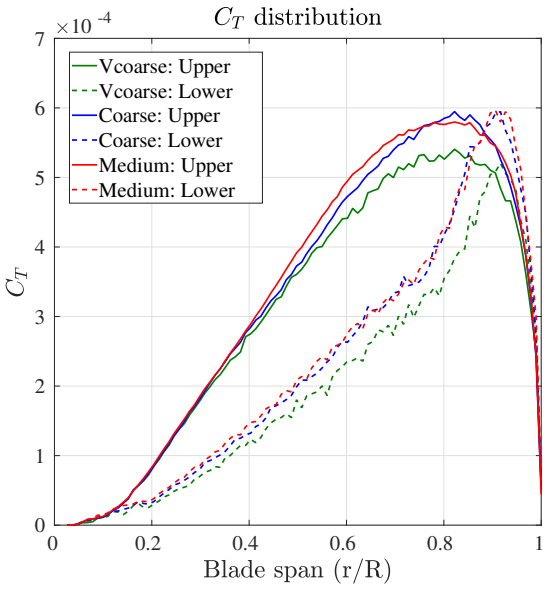

Figure 6.2: Grid convergence study for spanwise thrust distribution

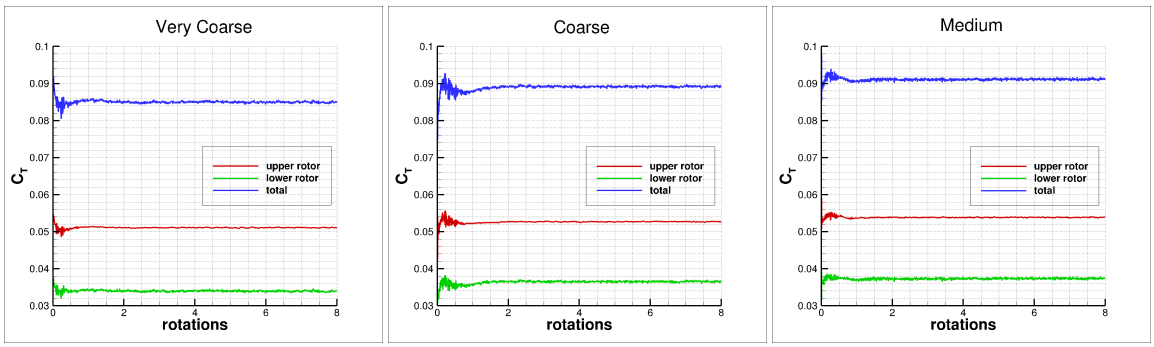

(a) Vcoarse (b) Coarse (c) Medium

Figure 6.3: Individual rotor thrust performance

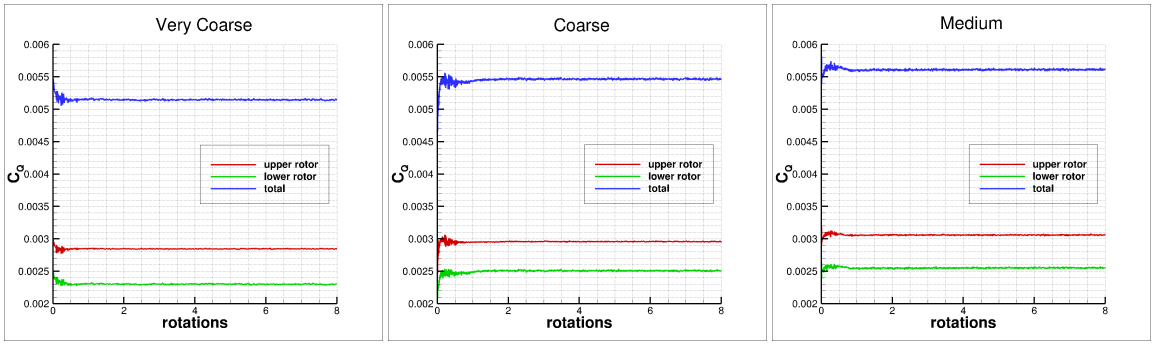

(a) Vcoarse (b) Coarse (c) Medium

Figure 6.4: Individual rotor torque performance

resolutions show converging trend from *Vcoarse* to *Coarse* and then *Medium*, which supports the final choice for *Medium* case. Another interesting thing to note is that difference between upper and lower rotor values (both thrust and torque) remains constant for all resolutions. This suggests

the fact that interaction between both rotors is dependent on bigger flow structures which are well captured even by *Vcoarse* case.

Aeroacoustic analysis

Various aeroacoustic parameters were analyzed in detail and finally a conclusion was made regarding the final choice of a resolution. The objective was to check what role resolution plays in acoustic performance of a co-rotating rotor and compare it with the resolution required for aerodynamic results.

Choice of Permeable FWH formulation over Solid FWH

For far-field analysis, two types of FWH formulation were used - *Permeable* and *Solid*, as mentioned in Chapter 5. The results were compared for both at different probe locations in the fluid domain. Figure 6.5 presents the results for probe 7 and probe 9, where probe locations are shown in Figure 5.10 (b). In case of in-plane probe 9, all 3 results (*probe, permeable* and *solid* FWH) match very well, with *permeable* tonal level within 0.3 dB/Hz of *probe* and *solid* tonal level within 0.5 dB/Hz. In case of out-of-plane probe 7, *solid* FWH produced tonal results with a difference of 2.5 dB/Hz from *probe* results and *permeable* FWH well within 0.1 dB/Hz. In case of broadband levels, both *solid* and *permeable* showed similar results. Thus, since *permeable* results were close to *probe* results overall, for any kind of spectral analysis in future, *permeable* FWH was selected. If necessary, *solid* FWH results were also presented for additional insight.

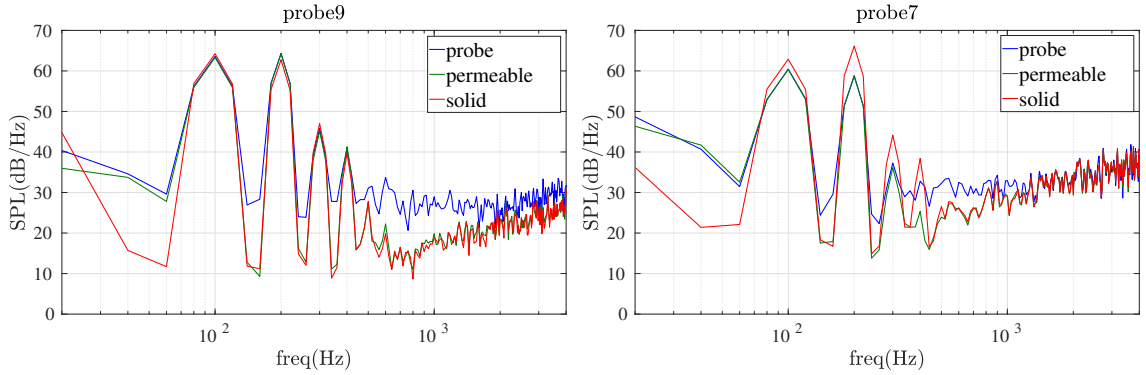

(a) Probe 9 (in-plane)

(b) Probe 7 (out-of-plane)

Figure 6.5: Comparison of permeable and solid FWH formulation

Comparison of different resolutions for C1 case

Noise spectra was plotted at two probe locations of Tinney [37]: probe 2 and probe 8, as shown in Figure 6.6, whereas, the probe locations are shown in Figure 5.14 in Chapter 5. At both locations, *Coarse* and *Medium* results are closer than *Vcoarse* results, especially for the broadband part. Therefore, it can be said that *Coarse* resolution is enough to capture the noise spectra of the rotor. On the other hand, the tonal noise result is similar for all 3 resolutions, as can also be seen in Figure 6.7 where grid convergence is checked for tonal peak value and also compared with experimental results. For both the probes, there is less than 0.5 dB/Hz variation between *Vcoarse* and *Medium*.

In spite of acoustic convergence in *Coarse* case, thrust results converged only until *Medium* case as seen previously and thus, *Medium* case was finally selected as the resolution suitable for further co-rotating rotor analyses.

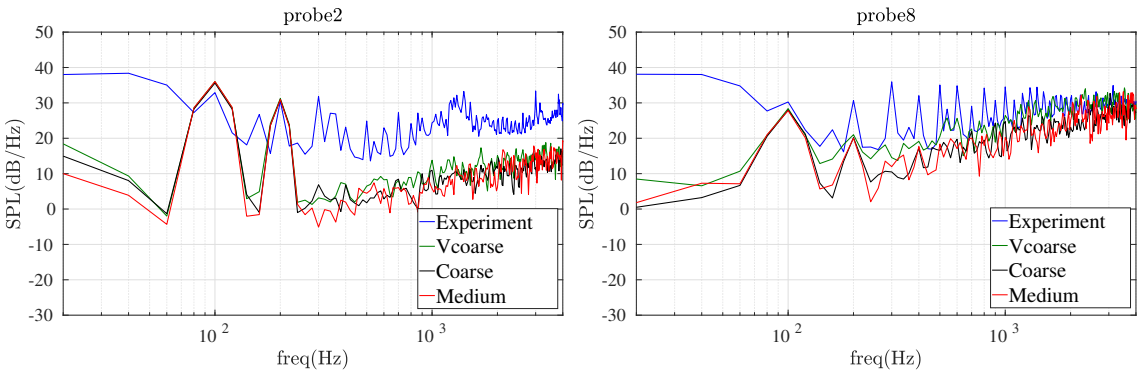

(a) Probe 2 (in-plane) (b) Probe 8 (out-of-plane)

Figure 6.6: Resolution study for noise spectra and comparison with experiments

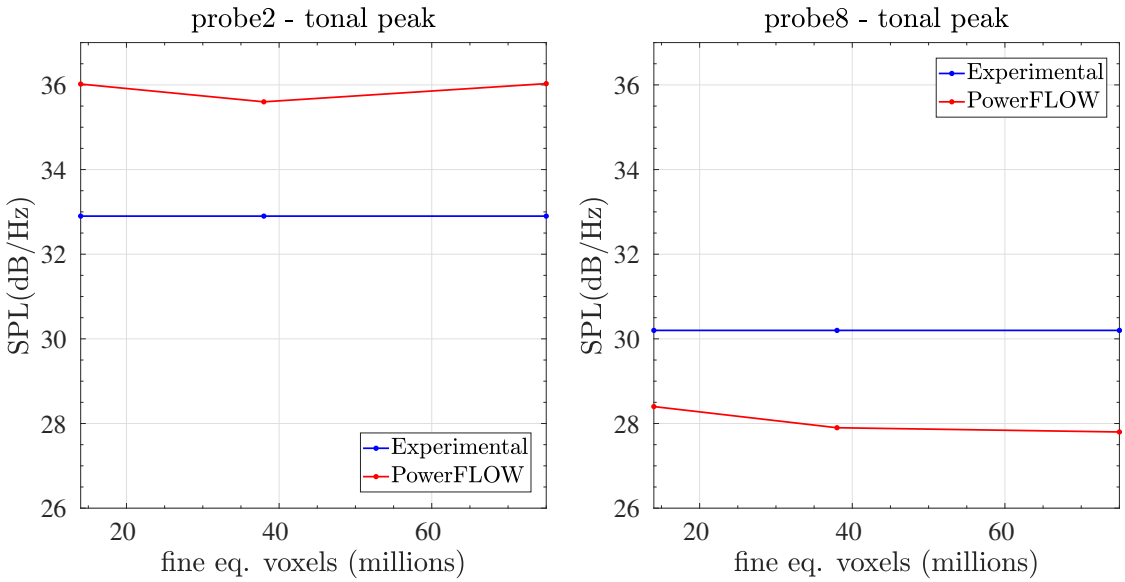

(a) Probe 2 (in-plane) (b) Probe 8 (out-of-plane)

Figure 6.7: Resolution study for tonal peak value and comparison with experiments

6.2. Baseline 2-bladed rotor

In this section, a short review of the results of 2-bladed isolated (baseline) rotor is presented. These results will be used to compare the performance of each rotor in a co-rotating rotor with the baseline rotor, which will help to understand the flow phenomena taking place. The simulation was performed at the resolution finalized in grid resolution study (phase I).

Thrust		**Torque**	
T (N)	**C_T**	**Q (Nm)**	**C_Q**
8.23	0.06	0.1903	0.0031

Table 6.2: Thrust and Torque value obtained for 2-bladed isolated rotor

Table 6.2 presents the thrust and torque value obtained for a rotational speed of 50 rps. Figure 6.8 shows the spanwise thrust distribution. The flow velocity magnitude v seen at a blade span

location increases from root towards tip (ωr increases as r increases), thus lift produced increases since lift is directly proportional to v^2 and consequently, thrust increases. At the tip, thrust sharply decreases due to tip vortex formation which decreases the pressure difference between the upper and lower surface of the blade, decreasing the lift.

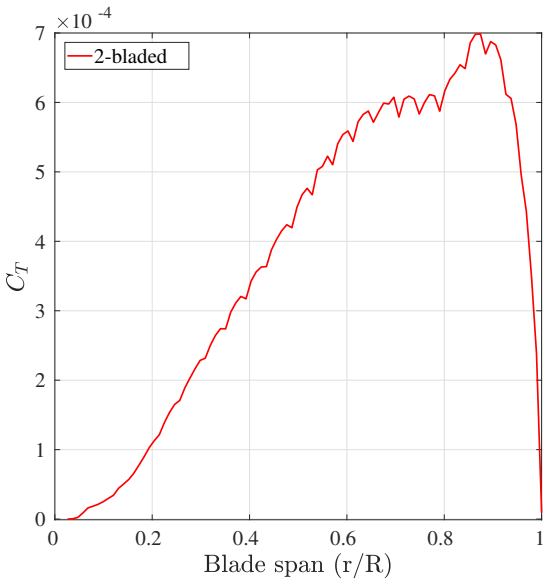

Figure 6.8: Spanwise thrust distribution for a 2-bladed isolated rotor

Around 0.8 *r/R*, there is sudden jump in thrust. To explain this phenomenon, the flow field was visualized by plotting vorticity contours as can be seen in Figure 6.9 (a). Tip vortices from each rotor can be seen convecting downwards and inwards starting from the rotor plane, which can also be seen from Figure 6.9 (b). The same trajectory is plotted in Figure 6.17 along with co-rotating rotor results. Each rotor blade interacts with these tip vortices which affects the flow around the blades; this interaction is termed as Blade Vortex Interaction (BVI). Figure 6.10 explains how this takes place, by depicting an interaction between a wing and a vortex.

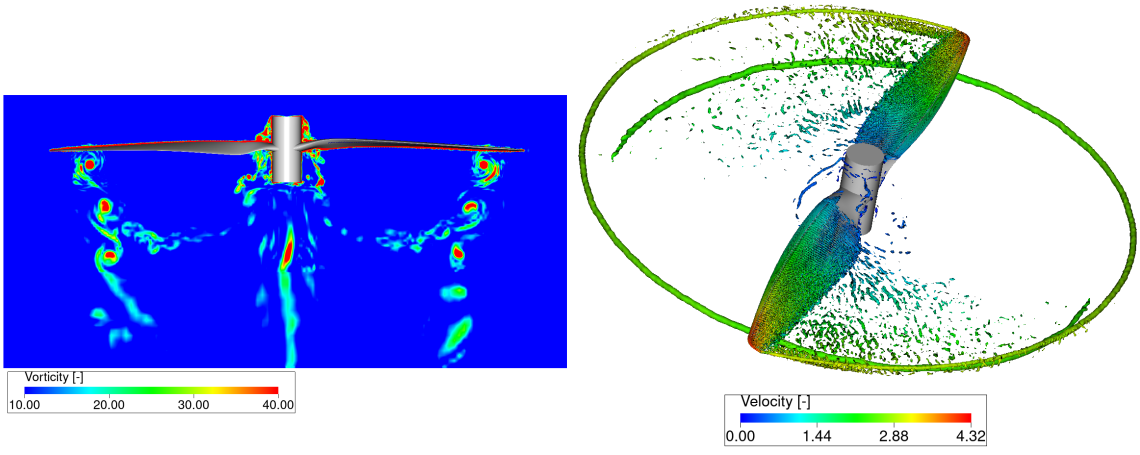

(a) Vorticity contours

(b) Isosurface visualization for λ_2=-5e6 1/sec^2

Figure 6.9: Tip vortex trajectory around the 2-bladed rotor in two different views

The vortex can be situated either in the plane of wing or upper or lower to it. The velocity in-

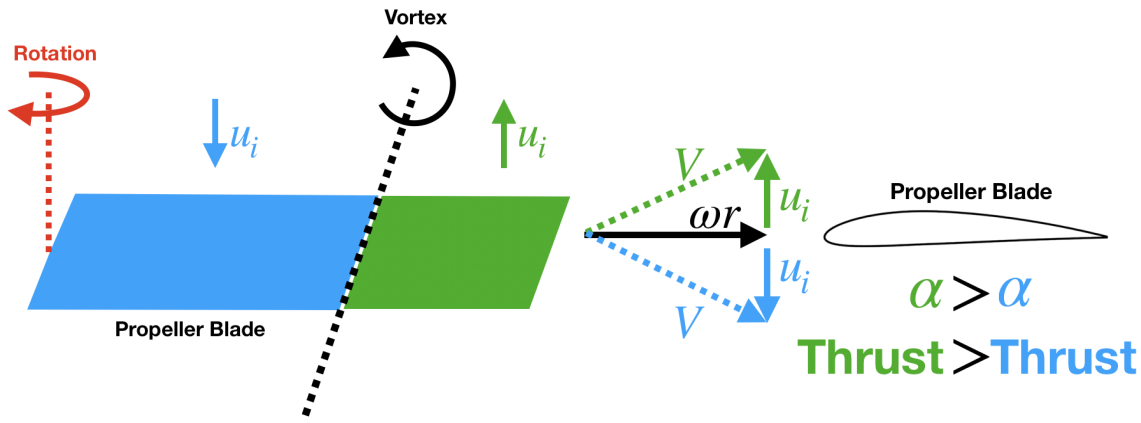

(a) Vortex interacting with a blade (b) Velocity diagram for an airfoil

Figure 6.10: Diagrammatic description of velocity induction due to vortices in the flow field

duced by a vortex is given by (for an incompressible inviscid flow):

$$V_\theta = \frac{\Gamma}{2\pi r} \tag{6.1}$$

where, Γ is the circulation around the vortex and r is the distance from vortex. Thus, the closer the vortex is to the wing, the stronger is the induction effect. The velocity induced in the **blue** region is downwards and in **green** region, upwards. This decreases angle of attack on the blade for the former and increases for the latter, as can be concluded from velocity diagram in Figure 6.10 (b) (α in the figure is the change in angle of attack). The result of this can be seen in Figure 6.11 where spanwise variation of axial velocity and angle of attack is plotted. These values are retrieved from the flow field calculation at a distance of 25mm in front of LE of the rotor blade, and thus do not represent the exact values experienced at the blade.

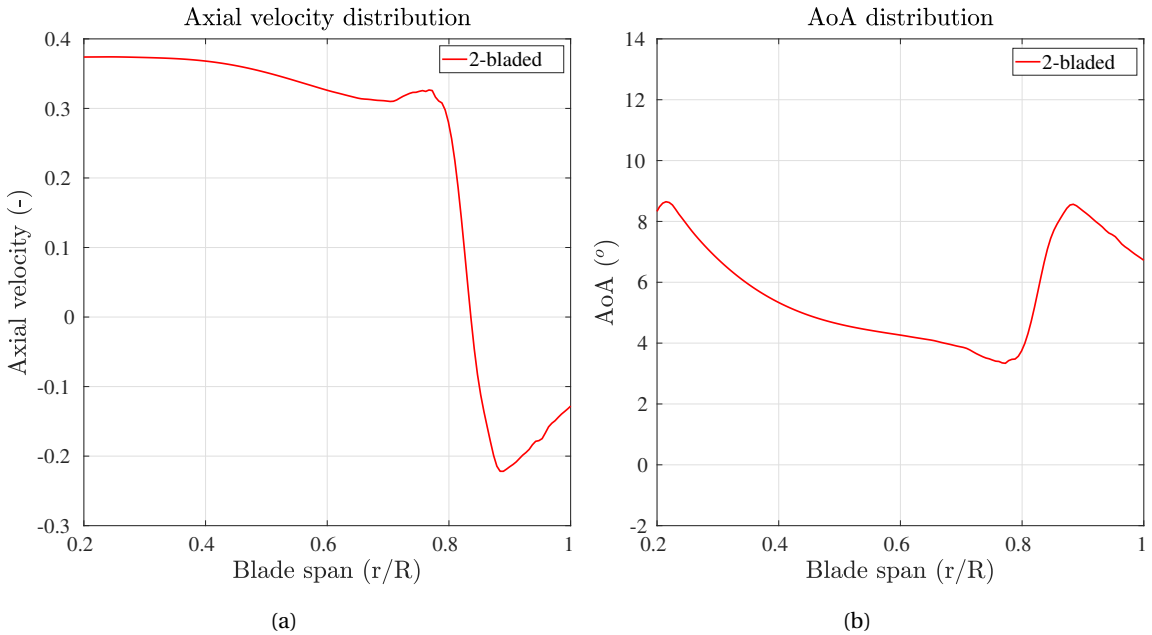

(a) (b)

Figure 6.11: Axial velocity and angle of attack distribution on a 2-bladed isolated rotor

The sharp change in axial velocity can be seen around 0.8 r/R which results in a corresponding change in AoA, and thrust produced. Accordingly, more the vortex is closer to the blade, more is this interaction effect and vice-versa. The sharp change in AoA would not be present if the tip vortices are situated further downstream of the rotor plane, ultimately increasing the overall thrust produced. In case of any co-axial rotor, the tip vortex trajectory is shifted due to the interaction of the other rotor. This will be more clear when results for the co-rotating rotor are analyzed.

6.3. Flow physics of co-rotating rotor

A total of 3 different co-rotating rotor configurations are discussed in this section. Initially, the results for rotor used in Phase I (*grid resolution study*) are analyzed. Then, the results for *azimuthal* and *axial variation* (Phase II) are discussed to understand the flow phenomena taking place.

6.3.1. Phase I

Table 6.3 shows the thrust and torque value obtained corresponding to the final resolution decided in *grid resolution study* and comparison with the experiment.

		PowerFLOW	Experiment	Difference	Difference (%)
Thrust	**T (N)**	12.22	13.94	1.72	**12.34**
	C_T	0.09	0.10	0.01	
Torque	**Q (Nm)**	0.3445	-	-	-
	C_Q	0.0056	-	-	

Table 6.3: Thrust and Torque value obtained from PowerFLOW and comparison of thrust with experiment

The thrust result obtained from PowerFLOW is different from the experimental result [37] by 12.34%, as can also be noticed from Figure 6.1 (a). This can be due to various reasons. The experiment was done in a confined environment that induces recirculation of the flow, and which is not present in the PowerFLOW computational setup. Other reasons can be due to difference in setup, wherein experimental setup had a different hub geometry and an additional electric motor and test stand. Further clarification will be given about this difference in the coming sections.

Aerodynamic analysis

Spanwise thrust variation

To understand the behaviour of co-rotating rotor, each of the upper and lower rotor is compared with the baseline 2-bladed rotor in Table 6.4 along with the corresponding spanwise thrust distribution in Figure 6.12. The thrust distribution is similar to what has been obtained by Bain [2] for a 2×3-bladed co-rotating rotor. Both the upper and lower rotor thrust is less than the baseline 2-bladed rotor, with the upper rotor producing more thrust than the lower rotor. The same conclusion has also been made by Mahendra [5]. To understand this, we need to take a look at Figure 6.13 where streamline path is visualized around both the upper and lower rotor. The upper rotor is operating in a freestream flow whereas the lower rotor is operating in a disturbed flow (wake of the upper rotor); this is the reason former produces more thrust than the latter. A more detailed explanation for the same is presented in the next few pages.

The upper and the lower rotor are operating in different rotor plane, separated by some axial distance Δz. There are 2 major consequences due to this:

- **Inflow effect**: Each rotor is acting in the *streamtube* of the other rotor. As a result, each rotor experiences an increased axial velocity as compared to the baseline rotor. The axial velocity at the lower rotor will increase more than at the upper rotor; this can be understood from the

		2-bladed	upper rotor	lower rotor
Thrust	**T (N)**	8.23	7.22	5
	C_T	0.06	0.05	0.04
Torque	**Q (Nm)**	0.1903	0.1879	0.1566
	C_Q	0.0031	0.0031	0.0026

Table 6.4: Thrust comparison of baseline rotor vs each rotor of 84^o co-rotating rotor

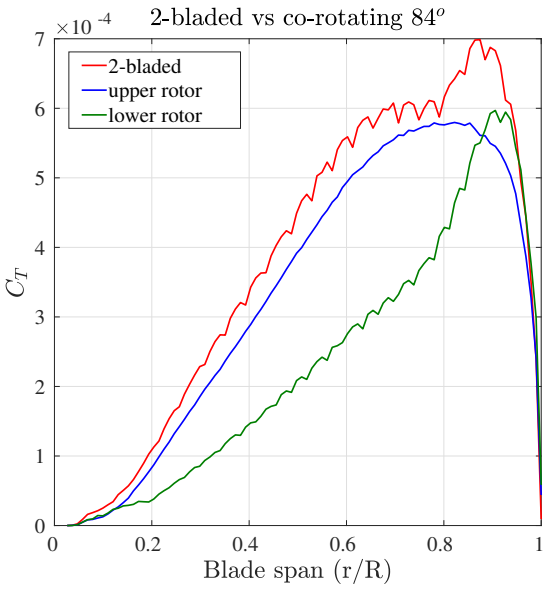

Figure 6.12: Comparison of spanwise thrust distribution of co-rotating rotor with baseline rotor

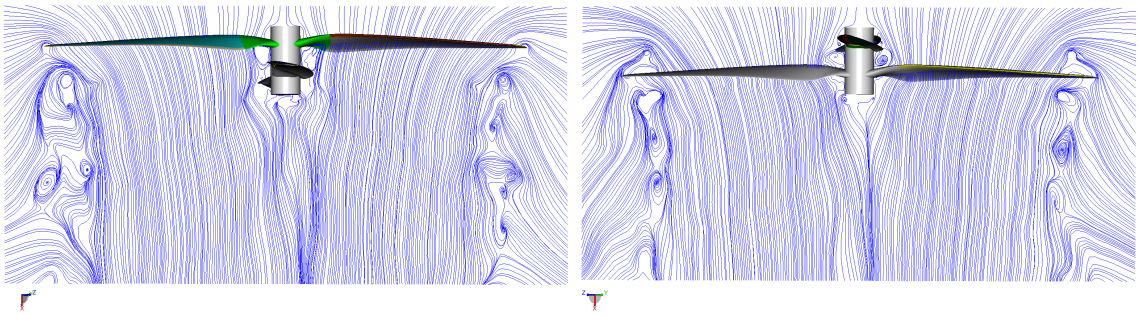

(a) Upper rotor (b) Lower rotor

Figure 6.13: Path followed by streamlines around a co-rotating rotor

shape of the *streamtube* in Figure 3.3 in Chapter 3. More the axial velocity, more is the inflow angle experienced by the blade and less is the angle of attack; thus, thrust produced decreases.

- **Blade-Vortex Interaction (BVI)**: Each rotor interacts with its own tip vortices (*self-induction*) and tip vortices of the other rotor (*interference*). This affects the flow on each rotor as explained previously in Section 6.2. The interaction effect on flow velocities can either be more or less as compared to a baseline rotor; this has been shown in the next page.

To explain the *inflow effect*, axial velocity and angle of attack are retrieved from the flow field (at the same point as for baseline rotor) as experienced by both the upper and lower rotor and com-

pared with the baseline rotor, as shown in Figure 6.14. The axial velocity for the lower rotor is higher than the upper rotor, as expected. Thus, for a twist distribution shown in Figure 5.2 (b) in Chapter 5, it translates to a higher AoA distribution for the latter, and consequently higher thrust, which is what we observe in the Figure 6.12.

The axial velocity for both the rotors is higher than the baseline rotor, which results in a higher AoA for the latter. This is what is observed in Figure 6.14 (b) and corresponding thrust distribution in Figure 6.12.

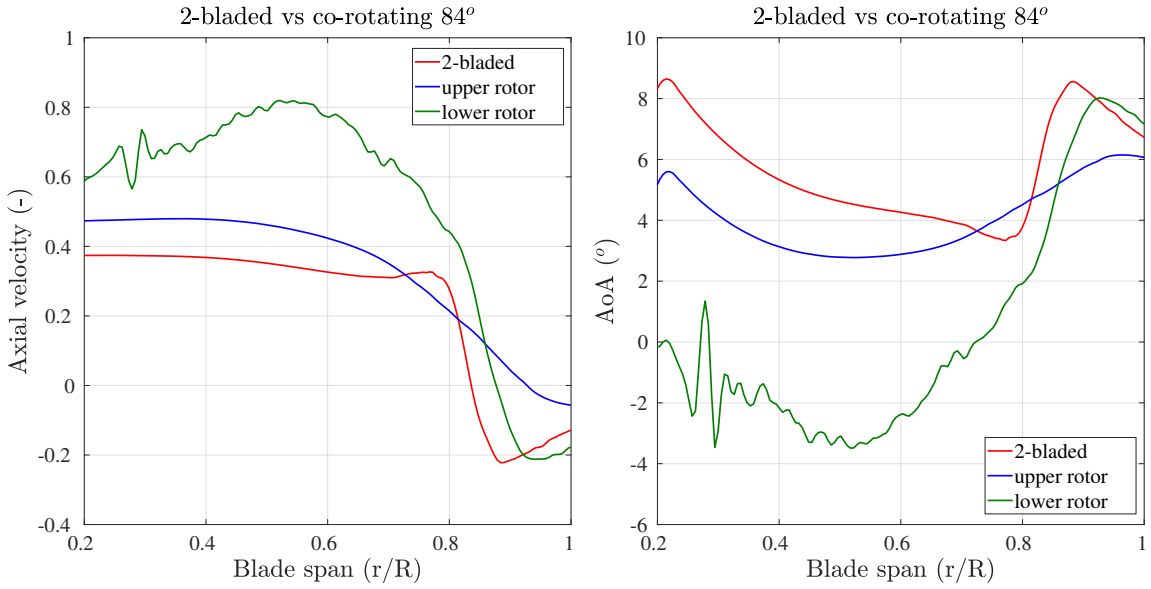

(a) (b)

Figure 6.14: Axial velocity and angle of attack distribution showing inflow and BVI effect

To the explain the effect of *BVI*, Figure 6.15 shows vorticity contour plots for both the *upper* and *lower rotor*. The *upper rotor* experiences freestream flow and interacts with vortices which are situated further downstream of the rotor. Thus, BVI is less in case of upper rotor, as compared to both lower rotor and baseline rotor. This is the reason why there is no sharp change observed in thrust distribution in Figure 6.12.

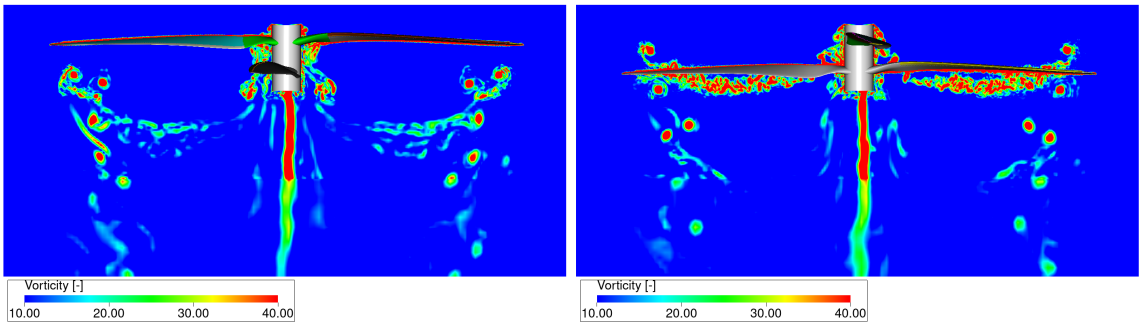

(a) Upper rotor (b) Lower rotor

Figure 6.15: Vorticity contour plots showing interaction of tip vortices with rotor blades

The *lower rotor*, on the other hand, interacts with upper rotor tip vortices (situated above the lower rotor) in addition to its own vortices (situated below the lower rotor), thus having much

greater interaction effect than compared to both the upper rotor and baseline rotor. Due to this, there is additional velocity induced at the lower rotor as explained in Section 6.2 which results in a sudden change in slope of AoA distribution (AoA decreases) after 0.8 *r/R* as shown in Figure 6.14 (b). Consequently, thrust rapidly increases before decreasing sharply at the tip.

As a whole, the *baseline* rotor behaves closer to *upper rotor* until 0.8 *r/R* (due to freestream flow) and closer to *lower rotor* after 0.8 *r/R* (due to BVI effect).

Another effect of BVI for lower rotor is increase of velocities around the blade tip which results in a stronger tip vortex, compared to upper rotor tip vortex. That is why a sharper decrease in thrust is observed for lower rotor than upper rotor, around the blade tip. From the vorticity data of Figure 6.15, lower rotor tip vortex was found to be 48.15% strong than upper rotor tip vortex.

Isosurfaces and tip vortex trajectory

Figure 6.16 compares vortices in the flowfield by isosurface visualization for λ_2=-1e6 1/sec^2. Comparison has been made between *Vcoarse* and *Medium* case. Due to higher resolution, *Medium* case is able to resolve even smaller flow structures which can be clearly seen from the figure. Since the convergence is achieved after *Medium* case, it suggests that resolving smaller vortices in the flowfield is necessary to capture the flow physics of a rotor.

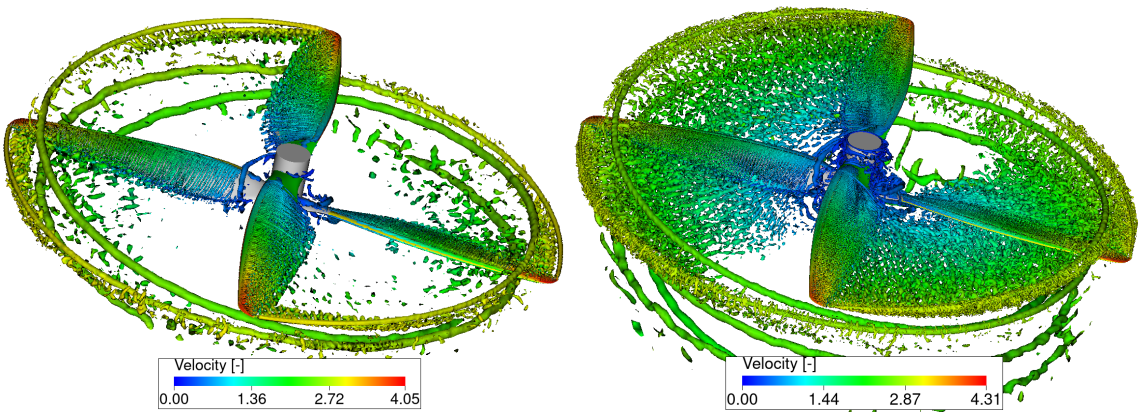

(a) Vcoarse (b) Medium

Figure 6.16: Isosurface visualization for λ_2=-1e6 1/sec^2

Observations made from these figures show different *tip vortex trajectories* for upper and lower rotor blade, as can also be seen in Figure 6.15. The same has been plotted in Figure 6.17, where comparison has been made with baseline rotor too. The upper rotor tip vortex convects faster axially than lower rotor and baseline rotor tip vortex. Looking at the slopes in Figure 6.17 (b), upper rotor tip vortex convects *twice as fast* (2×) as the lower rotor and baseline rotor tip vortex. This is due to the fact that velocity induced by lower tip vortex on upper tip vortex (eq. 6.1) is in downward direction whereas, velocity induced by upper tip vortex on lower tip vortex is in upwards direction. This results in increased distance between upper rotor and its tip vortex (compared to the baseline rotor), which has beneficial effect on upper rotor performance through decrease in BVI.

Following the shape of a streamtube, the *tip vortex* also convects radially inside, with upper tip vortex convecting more than lower tip vortex. The former contracts to around 69% of original radius, while the latter contracts to only 76% (for baseline rotor, it is 72%). This can be reasoned similarly. The induction due to lower tip vortex on upper tip vortex is in inward direction, whereas due to upper tip vortex on lower tip vortex is in outward direction. This increases the inward velocity of upper tip vortex and reduces for the lower. The same conclusions for tip vortex trajectory has been made by Mahendra [5] for both upper and lower rotor.

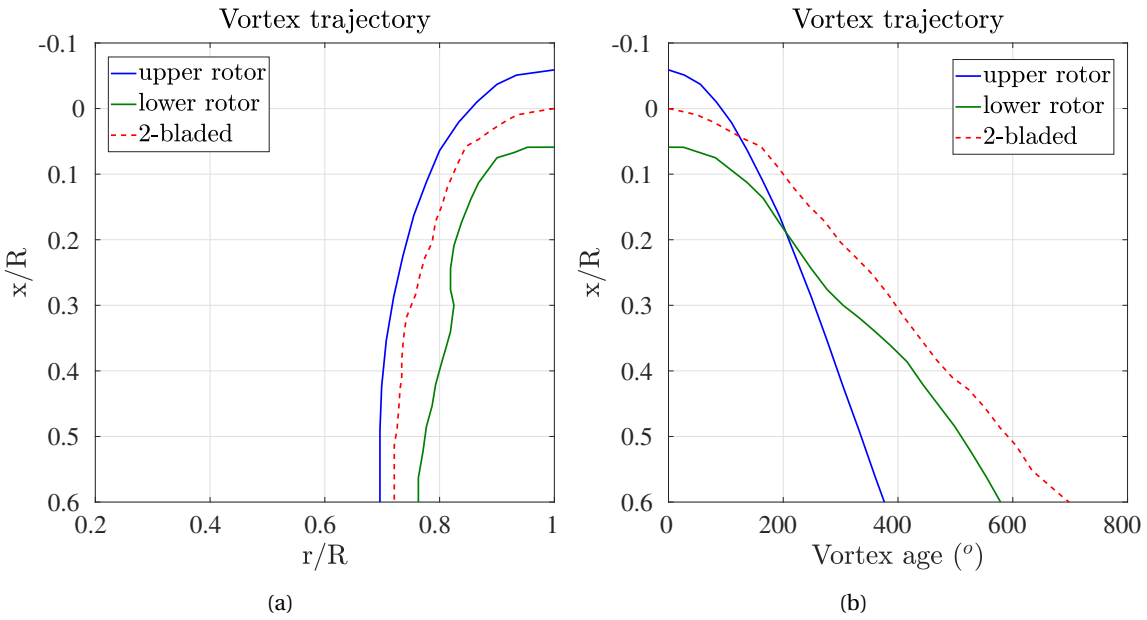

Figure 6.17: Tip vortex trajectory comparison between co-rotating and baseline rotor

The lower rotor blade misses the upper rotor tip vortex and passes below it. It can be attributed to this specific configuration of 84° azimuthal separation. When azimuthal and axial separation is varied, there is some difference expected in BVI (and also in inflow effect), which provides the motivation for the configurations chosen for the next phase. These differences will be more clear when the phase II results are analyzed in the next section. There is an additional vortex produced at the rotor *hub* which rotates in the same direction as rotor (whereas tip vortex rotates in opposite direction). In present case, the *hub* has bluff ends which may have an adverse effect on the overall performance and acoustics. Therefore, in future, the *hub* will be more streamlined so as to negate its effect.

Figure 6.18 shows *vorticity flowfield* at the plane of rotation for upper and lower rotor. It depicts formation of tip vortex for the *upper rotor* and additional vortices leaving past trailing edge (TE). In case of *lower rotor*, two major vortices can be seen - one of the lower rotor itself from the tip and another of the upper rotor tip vortex situated radially inwards to the former. This proves that upper tip vortex is moving axially downward and radially inward. The lower blade can be seen interacting with smaller vortices throughout its span (which was not present in case of upper blade where the flow is more clean), which shows the fact that lower rotor is operating in the wake of upper rotor, thus, adversely affecting the former's performance.

Aeroacoustic analysis

Noise spectra

Noise spectra was plotted at two probe locations of Tinney [37]: probe 2 and probe 8, and compared with experimental results, as shown in Figure 6.19. There are some differences observed between *PowerFLOW* and *experimental* results, especially in broadband part. One of the main reasons can be attributed to the flow recirculation in the confined environment where experiment took place [27]. Due to this, noise value in mid-frequency range (200-1000 Hz) increases due to increase in unsteady loading on the rotor blades, thereby, increasing loading noise. Other reasons can be background facility noise which is mainly attributed to low frequency region (20-70 Hz) and motor noise which powers the co-rotating rotor. These effects were not accounted for in the computational setup.

This difference is more in case of an *in-plane* probe, than compared to an *out-of-plane* probe.

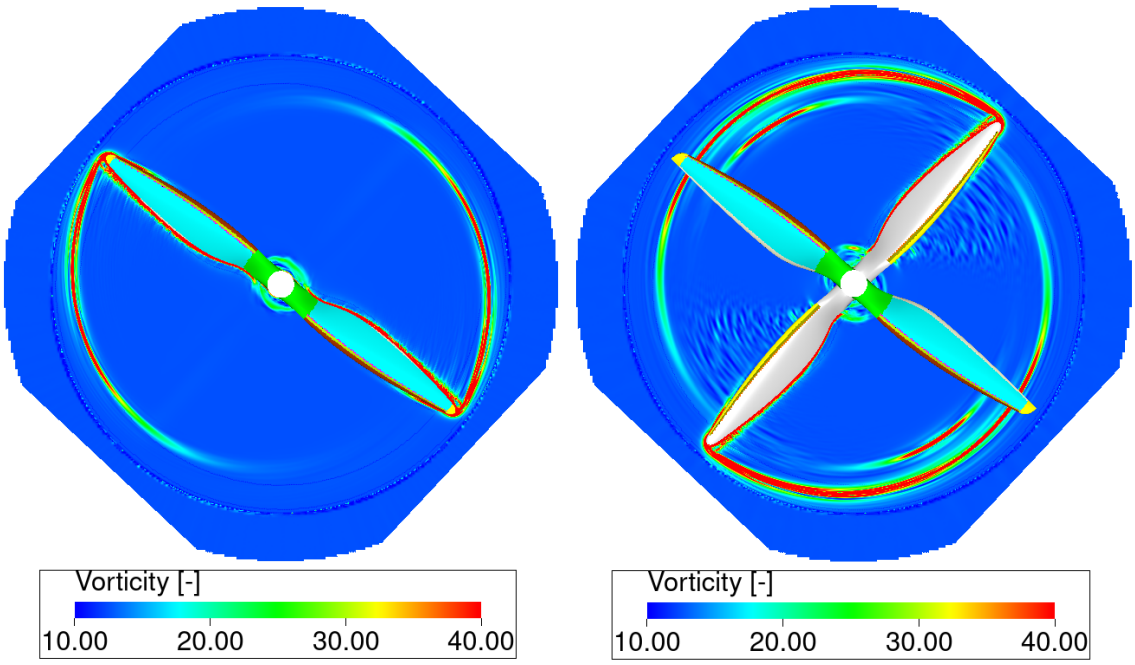

(a) Upper rotor (b) Lower rotor

Figure 6.18: Vorticity flowfield in the plane of rotation, for upper (a) and lower rotor (b)

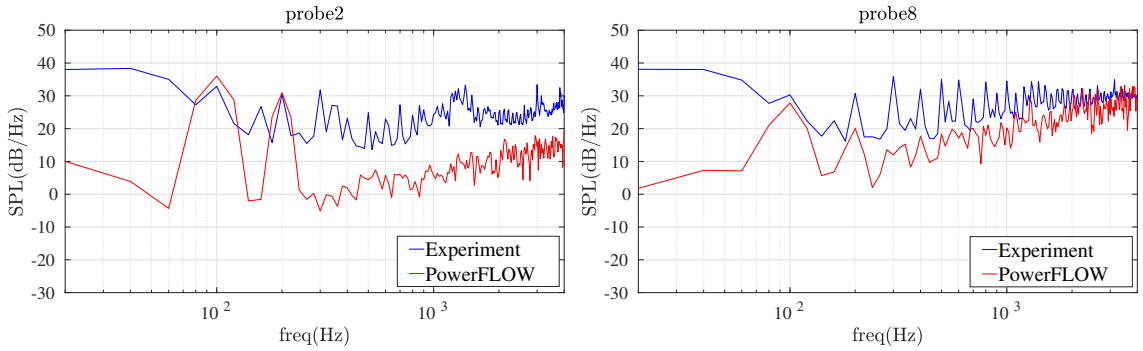

(a) Probe 2 (in-plane) (b) Probe 8 (out-of-plane)

Figure 6.19: Noise spectra and comparison with experiments

This can be attributed to the difference in thrust results obtained. Noise due to unsteady force (thrust) fluctuations are more pronounced in the plane of rotor, than out of plane. In other words, noise due to thrust is more at rotor plane than out-of-plane [17]. As a result, difference in thrust values is reflected more in the former. The same can be seen in Figure 6.20 where OASPL value (90-4000 Hz) has been plotted. The difference in case of in-plane probe is 9 dB whereas, in case of out-of-plane probe 8, it is only 3 dB.

Tonal peak is more for probe 2 than probe 8, by around 8 dB/Hz. This is due to the fact that tonal noise is produced by periodic variation of a signal, in the present case which is, the thrust force on the rotor blade rotating at 50 rps. This variation is more pronounced in the rotor plane than out-of-plane, and thus, tonal peak is higher for probe 2. Since each rotor is 2-bladed, the Blade Passage Frequency (BPF) comes out to be 100 Hz which is where we see the highest tonal peak. The higher harmonics peak value keep on decreasing, typical of a rotor noise spectra as seen in Figure 2.4 in

Chapter 2.

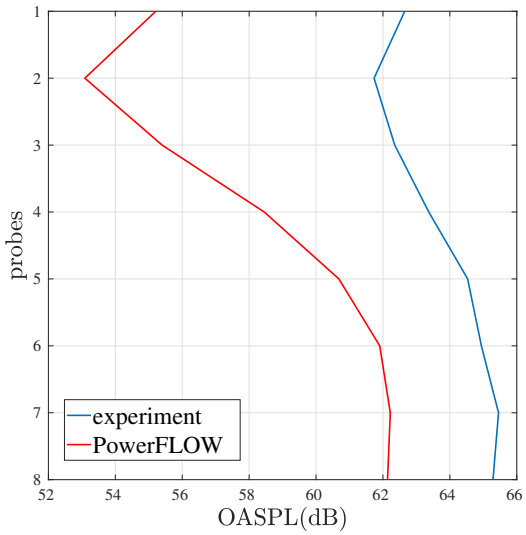

Figure 6.20: OASPL value comparison for 90-4000 Hz at probes 1-8: experiment vs PowerFLOW:

Another observation is that OASPL value (90-4000 Hz) at the rotor plane is less than compared to out-of-plane, by around 9 dB, as seen in Figure 6.20. This is due to the fact that broadband noise sources are of higher amplitude out-of-plane of the rotor than compared to in-plane [7], which can be seen in Figure 6.19 in case of PowerFLOW results. This also agrees with the results obtained by previous authors [40] [2] [37]. The same can be reasoned out from a plot of instantaneous pressure fluctuations at both the probes, shown in Figure 6.21, where upper and lower rotor contribution are plotted separately for 1 rotor rotation (0.02 sec). In case of probe 8 (out-of-plane), pressure fluctuations are much higher than compared to probe 2 (in-plane), which translates to a higher OASPL value for the former.

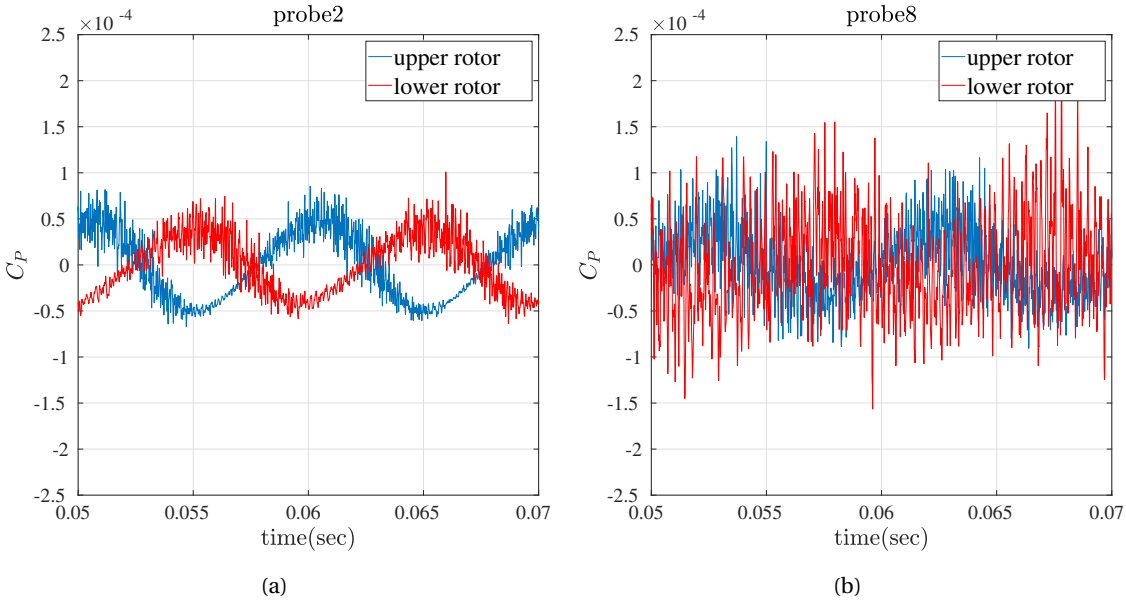

Figure 6.21: Raw signal comparison at probe 2 and probe 8

6.3.2. Phase II

This section deals with variation of *azimuthal* and *axial* separation for the co-rotating rotor. Two new configurations were run for the purpose, as mentioned in Table 6.5. All other parameters were same as the previous configuration. The configurations were chosen corresponding to the experimental data available.

Study	$\Delta\phi(^o)$	Δz	n (rps)
Azimuthal	12	1.1 in (2.79 cm)	50
Axial	84	1.3 in (3.30 cm)	50

Table 6.5: The two new configurations for phase II

Azimuthal variation

Table 6.6 compares the thrust and torque for two different azimuthal separations and their corresponding experimental results.

	Azimuthal (^{o})		PowerFLOW	Experimental	Difference	Difference (%)
Thrust	**12**	**T (N)**	11.7	13.34	1.64	**12.29**
		C_T	0.087	0.099	0.012	
	84	**T (N)**	12.22	13.94	1.72	**12.34**
		C_T	0.09	0.10	0.01	
Torque	**12**	**Q (Nm)**	0.3359	-	-	**-**
		C_Q	0.0055	-	-	
	84	**Q (Nm)**	0.3445	-	-	**-**
		C_Q	0.0056	-	-	

Table 6.6: PowerFLOW values obtained and comparison of thrust with experiment

The *thrust* value decreased as the azimuthal separation was decreased, which is the same conclusion obtained by all the previous authors [5] [20] [32] [40] [37]. Decrease of thrust value was also accompanied by decrease of *torque* and thus, decrease in power required (since rps is constant) to rotate the co-rotating rotor. The difference between *PowerFLOW* and *experiment* is similar in both azimuthal separations, which was also the case while varying axial separation as will be seen in the next few pages. Therefore, it can be concluded that there were some aspects of experiment setup which were not being captured by the computational setup. This can be either due to the confined environment of test section, or effects due to hub and motor or errors in experimental setup, or a combination of these. A future study will be performed to explore the reasons for this difference observed.

Aerodynamic analysis

Spanwise thrust variation

To understand the reason for decrease of thrust in case of 12^o separation, spanwise thrust variation was compared to the 84^o separation case, as shown in Figure 6.22. As the azimuthal separation decreases, upper rotor thrust increases and for the lower rotor, thrust decreases. Since the decrease in latter is more than the increase in former, overall thrust decreases. To understand why this takes place, the 12^o configuration was also compared to the baseline configuration, as shown in Table 6.7

The results show that upper rotor thrust increases to even more than the baseline rotor while the lower rotor thrust decreases. This can also be seen in case of spanwise thrust distribution as shown in Figure 6.23 (a). The upper rotor is performing even better than an isolated 2-bladed rotor. This can be explained by looking at this particular co-rotating configuration. The upper and lower rotor

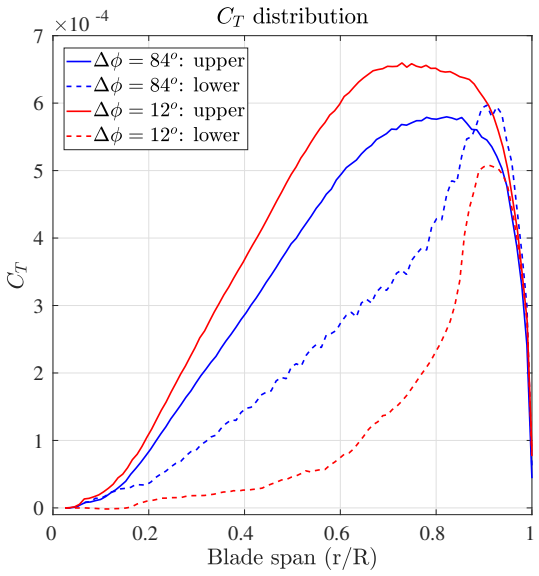

Figure 6.22: Spanwise thrust variation - 84^o vs 12^o

		2-bladed	upper rotor	lower rotor
Thrust	**T (N)**	8.23	8.96	2.74
	C_T	0.06	0.067	0.02
Torque	**Q (Nm)**	0.1903	0.2063	0.1296
	C_Q	0.0031	0.0034	0.0021

Table 6.7: Thrust comparison of baseline rotor vs each rotor of 12^o co-rotating rotor

are situated very close to each other. This gives rise to a third phenomenon, commonly known as: *Circulation effect*.

- **Circulation effect**: Figure 6.23 (b) shows the phenomenon for high lift airfoils in case when a flap is deployed with an airfoil [29]. The flap is equivalent to a vortex kept near the TE of an airfoil which has the same circulation as the flap. The vortex increases velocity on the upper surface and decreases on the lower, thus, increasing the pressure difference between the surfaces. The lift, therefore, increases to values more than the case when there would be no vortex present.

When the lower rotor is added downstream of the upper rotor, there are 3 flow phenomena taking place: *Inflow effect*, *Circulation effect* and *BVI effect*, where the first two effects are potential effects. The circulation effect, due to lower rotor acting as a flap for the upper rotor, increases the upper rotor thrust and opposes the other two effects (which have adverse consequences for thrust). The increase due to former is more than the decrease due to latter, because of which upper rotor produces thrust more than the baseline rotor.

The increased upper rotor thrust induces more axial velocity at the lower rotor, thus, decreasing angle of attack of the latter and ultimately decreasing the thrust to values even lesser than the lower rotor of 84^o configuration, as can be seen from Figure 6.22. Similarly, when lower rotor thrust decreases, it reduces the induced axial velocity on the upper rotor, increasing the AoA and thereby, increasing thrust. This can also be observed from Figure 6.24 where axial velocity and AoA distribution can be compared when azimuthal separation is changed from 84^o to 12^o. The circulation effect will play a role only in case of lower azimuthal separation and will decrease as the separation is increased.

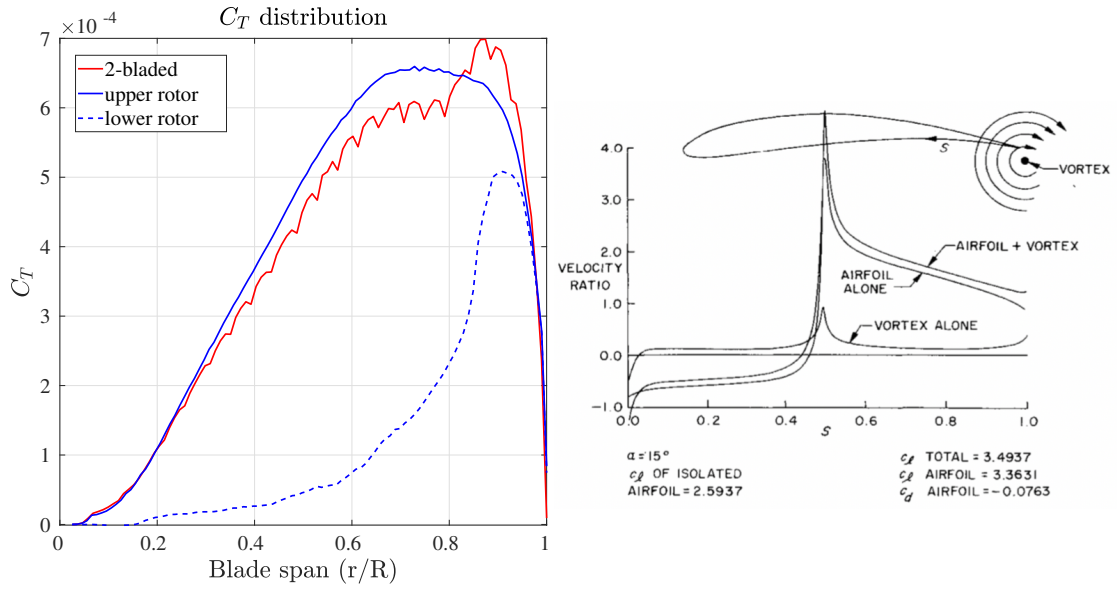

(a) 2-bladed baseline vs 12° co-rotating rotor

(b) Circulation effect [29]

Figure 6.23: Spanwise thrust variation and circulation effect

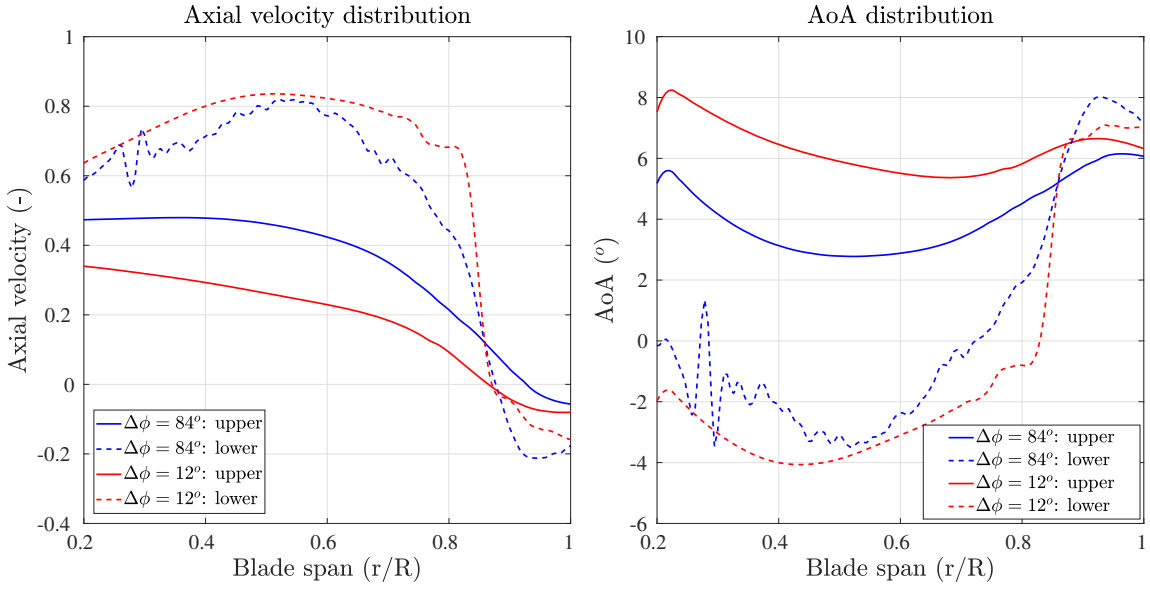

(a)

(b)

Figure 6.24: Comparison of 84° and 12° co-rotating configurations

Figure 6.25 shows *vorticity field* for upper and lower rotor. Similar to previous 84° configuration, *upper rotor* is acting in a freestream flow and having very less BVI effect. The *lower rotor*, on the other hand, is interacting with both the upper and lower rotor tip vortices, both of them situated below the lower rotor. The tip vortex trajectory can also be visualized from Figure 6.26, where isosurfaces have been plotted for λ_2=-5e6 1/sec^2. The effects due to BVI can be observed in the distribution of axial velocity, AoA and thrust, similar to as explained in Section 6.3.

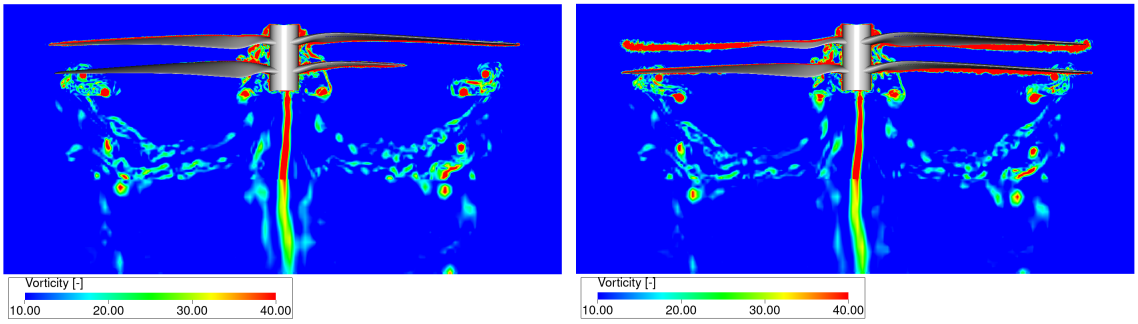

(a) Upper rotor (b) Lower rotor

Figure 6.25: Vorticity contour plots showing interaction of tip vortices with rotor blades, for 12^o azimuthal separation

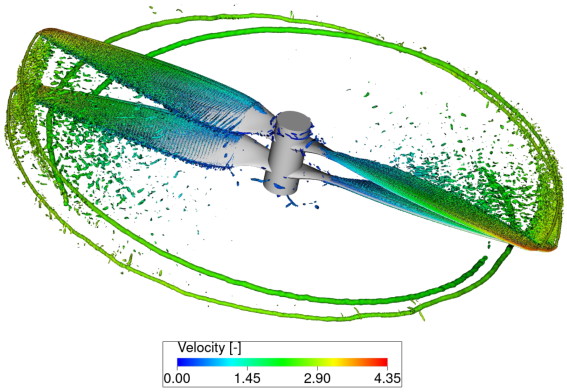

Figure 6.26: Isosurface visualization for λ_2=-5e6 $1/sec^2$, for 12^o azimuthal separation

Coupled system of rotor

In a co-rotating rotor, a total of 3 different effects have been found: *Inflow effect*, *BVI effect* and *Circulation effect*. When azimuthal separation is changed, a combination of these effects determine the behaviour of each of the upper and lower rotor. Both the rotors affect each other through their mutual interaction and thus, operate as a coupled system of rotor. Therefore, a change in one rotor will induce a change in the other rotor too.

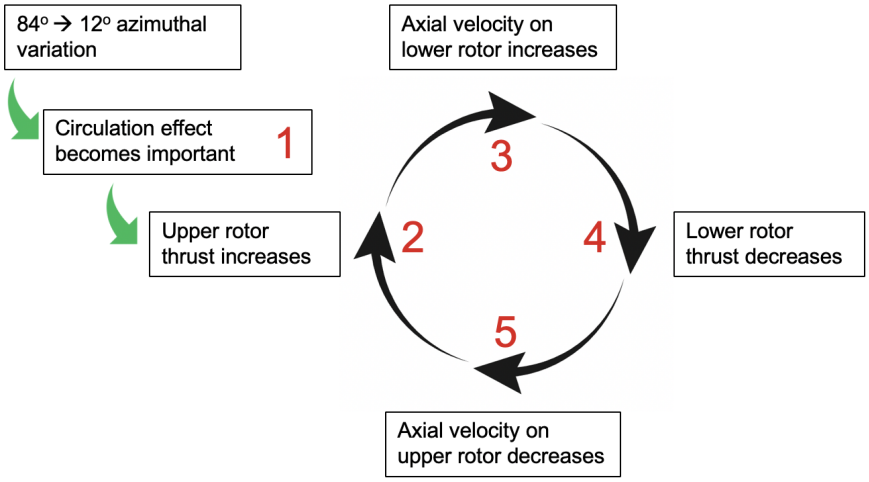

Figure 6.27: Coupled system of rotor for azimuthal variation; numbers correspond to the below-mentioned steps

Figure 6.27 explains the coupled system in the context of azimuthal variation. As the separation is reduced from 84° to 12°, a number of changes take place as:

1. *Circulation effect* takes place due to lower rotor coming closer to the upper rotor
2. *Upper rotor* thrust increases
3. Axial velocity induced at the *lower rotor* increases
4. *Lower rotor* thrust decreases
5. Axial velocity induced at the *upper rotor* decreases; and the process repeats itself from step 2-5 until a converged state has been achieved by both rotors

Individual rotor performance and thrust convergence

The increase in upper rotor thrust and a corresponding decrease in the lower one can also be observed from Figure 6.28, where individual rotor and total thrust is compared between 84° and 12° configurations, by plotting the convergence history upto 6 rotations. It can be clearly noticed that decrease in lower rotor surpasses the increase in upper rotor, thereby, reducing the overall rotor thrust.

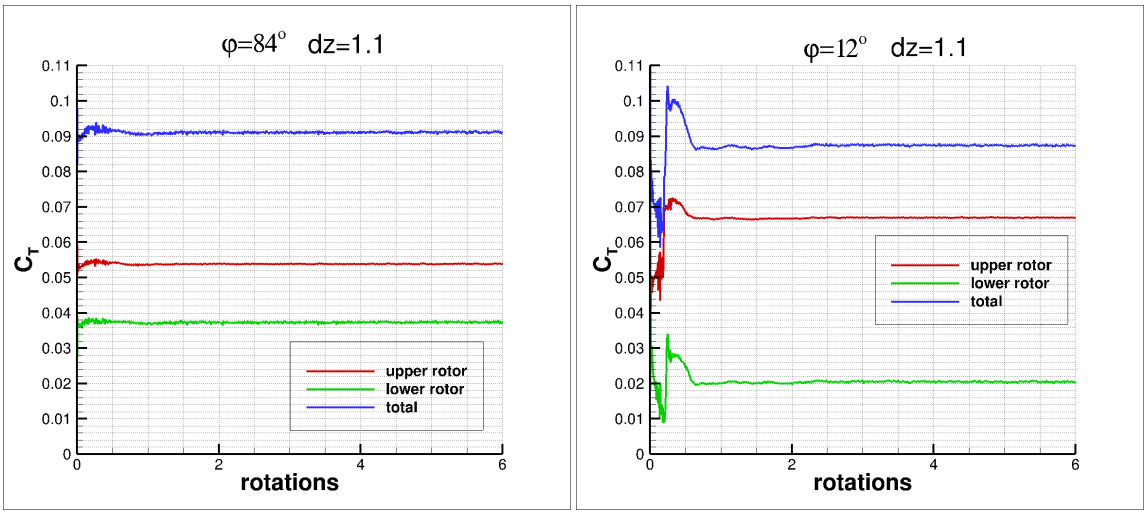

(a) 84° (b) 12°

Figure 6.28: Individual rotor thrust performance; comparison between 12° and 84° configurations

Aeroacoustic analysis

Noise spectra

Noise spectra is compared between 84° and 12° configurations, and their corresponding experimental results. Tonal noise in case of 12° is higher than 84° configuration, although broadband noise is similar. In case of *PowerFLOW* results, first tonal peak of 12° is higher than 84° case by 17 dB/Hz for probe 2, whereas 16 dB/Hz for probe 8. The difference between *experimental* and *PowerFLOW* results is also observed in case of 12° which can be due to similar reasons as mentioned previously in section 6.3.1 for 84° configuration.

To investigate the reasons for increase in noise for 12° case, the *raw pressure signal* was plotted at probe 2 for upper and lower rotors separately, and compared with 84° case as shown in Figure 6.30. There is higher destructive interference observed for the latter, as compared to the former, which corresponds to particular azimuthal separation for each configuration. Due to this, even though overall thrust increases for 84° case, noise generated is lower.

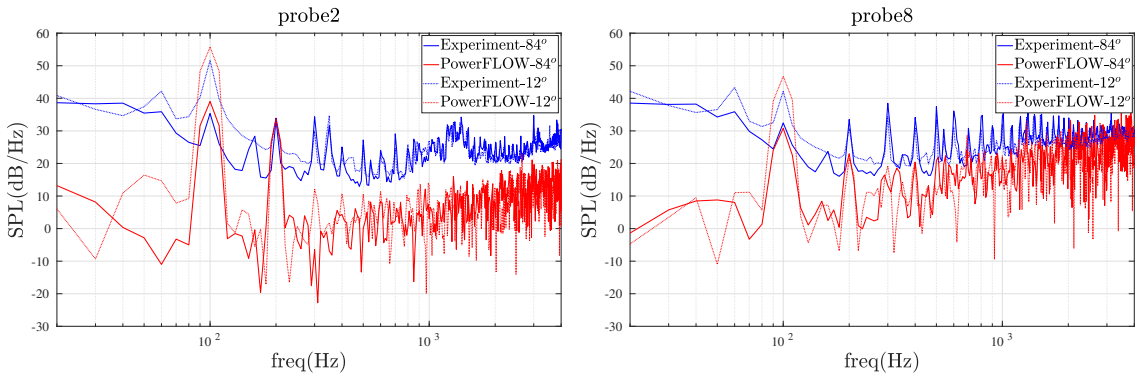

(a) Probe 2 (b) Probe 8

Figure 6.29: Noise spectra comparison between 84° and 12° for both PowerFLOW and experiment

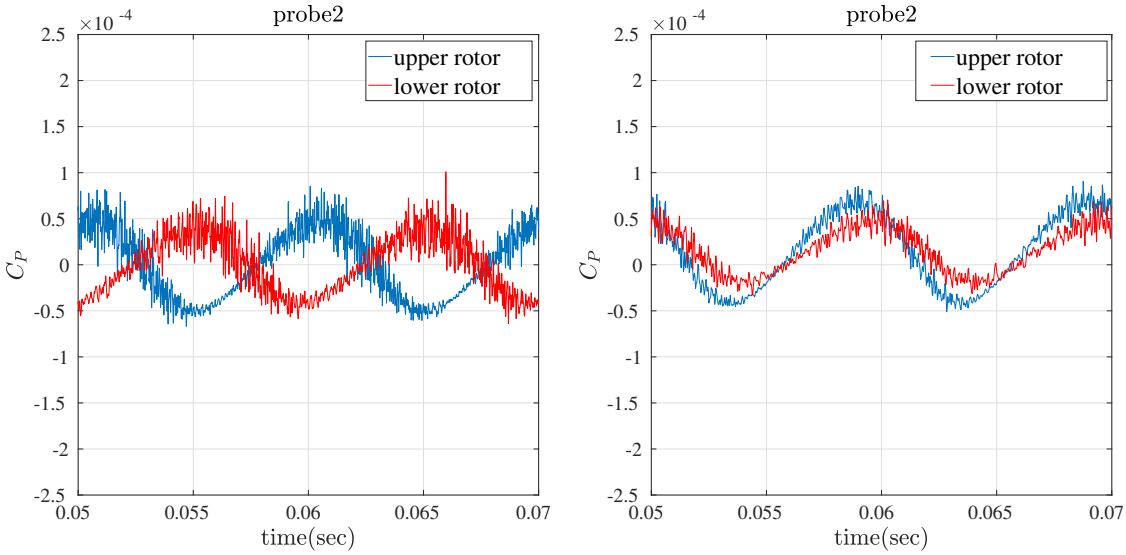

(a) 84° case (b) 12° case

Figure 6.30: Raw signal comparison at probe 2 for 84° and 12°

In-plane vs out-of-plane

Figure 6.31 compares the noise at all probes 1-8 by plotting OASPL value for 90-4000 Hz. The destructive interference plays a much bigger role at the *rotor plane*, than compared to *out-of-plane* location. This is the due to the fact that fluctuations are lower for the former, than for the latter, as can also be seen in Figure 6.21 in section 6.3.1. In other words, destructive interference is more important for tonal noise (which dominates in-plane) than for the broadband noise (which dominates out-of-plane). Therefore, noise at the *rotor plane* is much lower for 84° separation than 12° separation (by 14 dB), while *out-of-plane* the difference reduces to close to 0 dB.

Axial variation

The results related to axial separation and its effect on rotor flow physics are mentioned in this section. Table 6.8 compares the *thrust* and *torque* for two different axial separations and their corresponding experimental results.

As the axial separation is increased, thrust production increases too. This is the same conclu-

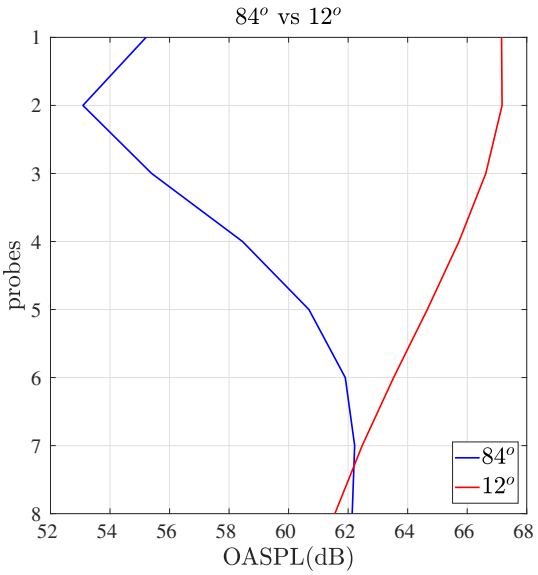

Figure 6.31: OASPL comparison for 90-4000 Hz between 84^o and 12^o

	Axial		PowerFLOW	Experimental	Difference	Difference (%)
Thrust	**1.1 in**	**T (N)**	12.22	13.94	1.72	**12.34**
		C_T	0.09	0.10	0.01	
	1.3 in	**T (N)**	12.31	14.14	1.83	**12.94**
		C_T	0.091	0.106	0.015	
Torque	**1.1 in**	**Q (Nm)**	0.3445	-	-	**-**
		C_Q	0.0056	-	-	
	1.3 in	**Q (Nm)**	0.3432	-	-	**-**
		C_Q	0.0056	-	-	

Table 6.8: PowerFLOW values obtained and comparison of thrust with experiment

sion obtained by previous authors [5] [20] [19] [40] [37]. The difference between *experiment* and *PowerFLOW* remains similar for the two different axial separations, which was also found in case of azimuthal variation. Thus, the same conclusion can be made about the computational setup, that, it is not able to capture some aspects of the experimental setup which accounts for the difference in thrust values obtained.

Aerodynamic analysis

Spanwise thrust variation

To investigate the reason for increase of thrust values, spanwise thrust distribution for both upper and lower rotor was compared between *1.1 in* and *1.3 in* configurations, as shown in Figure 6.32. Table 6.9 mentions the corresponding *thrust* and *torque* values. Although the difference between the thrust values is very less, upper rotor thrust increases and for the lower rotor, thrust decreases. This trend was also found by Mahendra [5] as shown in Figure 3.10 in Chapter 3.

The axial separation behaviour can be reasoned on the basis of streamtube of both rotors. When separation increases, axial velocity induced on the upper rotor due to lower rotor reduces which can be reasoned from the shape of the streamtube of the lower rotor. This increases the AoA on upper rotor and thereby, the thrust produced. Increase in upper rotor thrust increases the axial velocity induced at the lower rotor which decreases the AoA and thus, decreasing the thrust produced. The increase in upper rotor thrust is more than the decrease for lower rotor, therefore, overall thrust

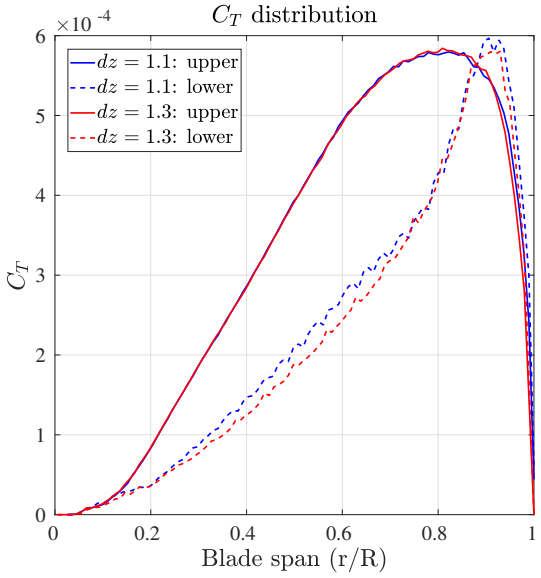

Figure 6.32: Comparison of spanwise thrust variation between 1.1 in and 1.3 in axial separations

		1.1 in		1.3 in	
		upper	**lower**	**upper**	**lower**
Thrust	**T (N)**	7.22	5	7.43	4.88
	C_T	0.05	0.04	0.055	0.036
Torque	**Q (Nm)**	0.188	0.157	0.189	0.154
	C_Q	0.0031	0.0026	0.0031	0.0025

Table 6.9: Individual rotor thrust and torque comparison between 1.1 in and 1.3 in configurations

increases. A comparison of axial velocity and AoA for both axial separations has been shown in Figure 6.33.

Based on this reasoning, as axial separation is increased, thrust increases. After a particular value of separation, the mutual induction of each rotor will be reduced considerably, which will lower the advantage in thrust produced as the separation is increased. For this reason, a converged value of thrust will be obtained after a particular axial separation. The same result has been shown by Mahendra [5] in Figure 3.10.

The BVI for *1.3 in* configuration is similar to *1.1 in* configuration, as was shown in Figure 6.15. The effects due to BVI can be observed in the axial velocity, AoA and thrust distribution for the lower rotor.

Coupled system of rotor

The above explanation for the variation in axial separation can be summarized in steps, which represents a 2-rotor system coupled to each other.

Figure 6.34 explains the coupled system in the context of axial variation. As axial separation is increased:

1. Axial velocity induced at the *upper rotor* decreases
2. *Upper rotor* thrust increases
3. Axial velocity induced at the *lower rotor* increases

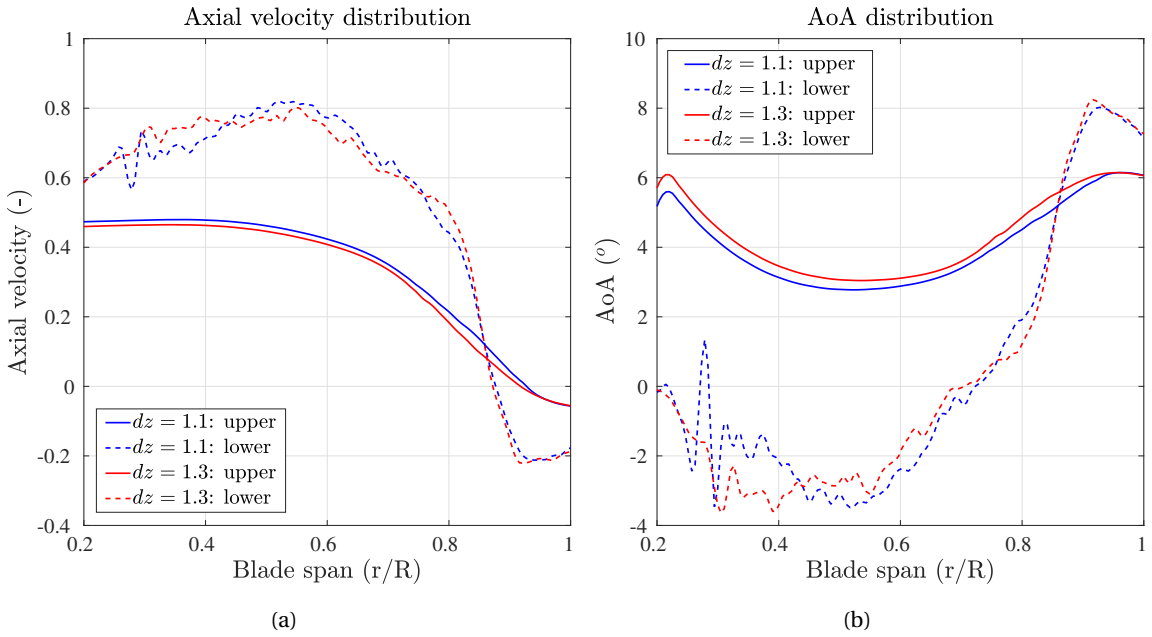

Figure 6.33: Comparison of 1.1in and 1.3in axial separation

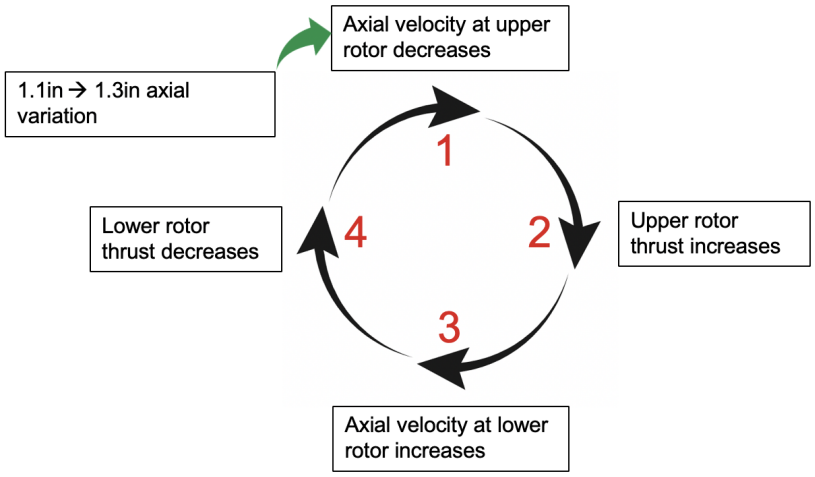

Figure 6.34: Coupled system of rotor for axial variation; numbers correspond to the mentioned steps

4. *Lower rotor* thrust decreases; and the process repeats itself from step 1-4 until a converged state has been achieved by both rotors

Aeroacoustic analysis

Noise spectra

Noise is compared at probe 2 and probe 8 for two different axial separations as shown in Figure 6.35. As expected, noise increases for *1.3 in* case due to increase in overall thrust value, thus increasing the loading noise term in the FWH equation 2.9. The increase in noise is less though, due to minimal increase in thrust value. The tonal peak value for *1.3 in* is higher by 0.4 dB/Hz than *1.1 in* for probe 2, and by 0.8 dB/Hz for probe 8.

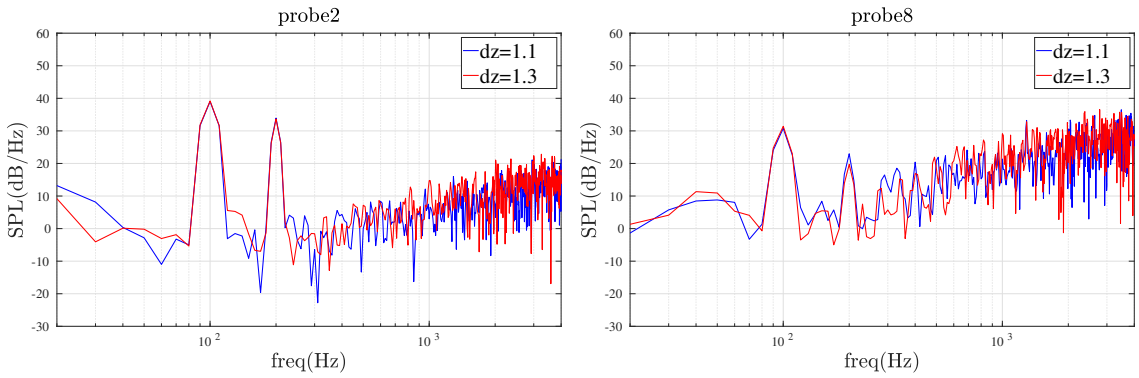

(a) Probe 2 (in-plane) (b) Probe 8 (out-of-plane)

Figure 6.35: Noise spectra comparison between 1.1in and 1.3in axial separations of co-rotating rotor

In-plane vs out-of-plane

Figure 6.36 compares the noise at all probes 1-8 by plotting OASPL value for 90-4000 Hz. The noise increases at all probe locations for *1.3 in* than compared to *1.1 in*. The difference in noise level is 1.5 dB for *out-of-plane* probes and 1 dB for *in-plane* probe, thus, more for the former as compared to the latter (opposite to what was observed in case of azimuthal angle variation). This is because broadband noise increases as thrust increases due to increase in axial distance, which increases out-of-plane noise even further, similar to what was obtained by Whiteside [40].

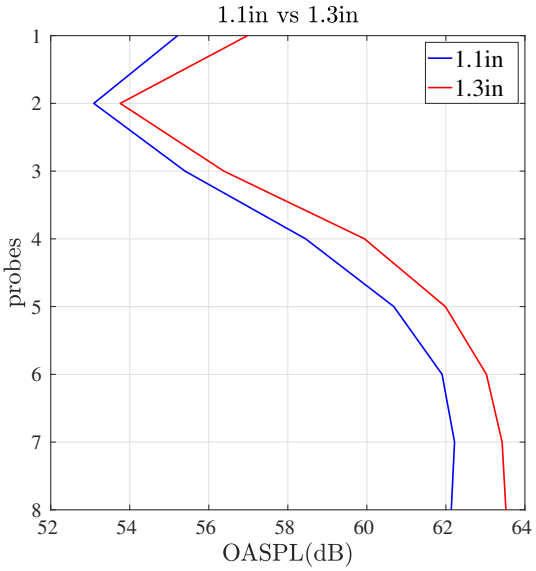

Figure 6.36: OASPL comparison for 90-4000 Hz between 1.1in and 1.3in

6.4. Co-rotating vs 2-bladed: noise comparison

A comparison was made between the co-rotating rotor with 12^o azimuthal separation and a 2-bladed rotor having the same thrust as the former. For the purpose, the collective pitch angle of the 2-bladed rotor was increased by 4.5^o. The pitch angle value was obtained by running low-fidelity simulations on a BEMT tool based on XFOIL, developed by E. Grande in the Wind Energy Group.

Table 6.10 compares the *thrust* and *torque* value of the co-rotating and 2-bladed rotor. Figure

	Co-rotating 12^o	**2-bladed**
T (N)	11.7	11.8
C_T	0.087	0.088
Q (Nm)	0.3359	0.3095
C_Q	0.0055	0.0050

Table 6.10: Thrust and Torque comparison of 12^o co-rotating and 2-bladed rotor

6.37 compares the *noise spectra* between the two configurations. The co-rotating rotor at 12^o azimuthal separation produces higher noise than the 2-bladed rotor producing the same thrust. This can also be seen in Figure 6.38 where OASPL value is compared for 90-4000 Hz. The noise difference is 2 dB at the rotor plane, which increases to 2.5 dB out-of-plane.

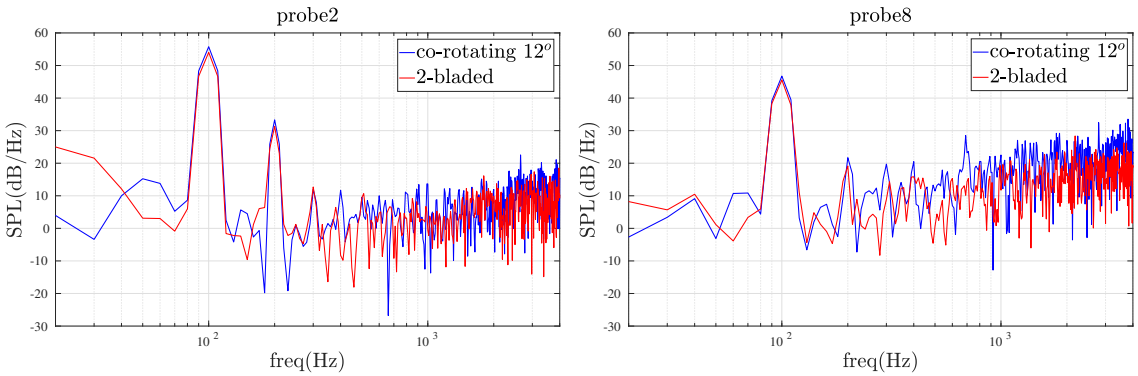

(a) Probe 2 (in-plane)

(b) Probe 8 (out-of-plane)

Figure 6.37: Noise spectra comparison between 12^o co-rotating and 2-bladed rotor

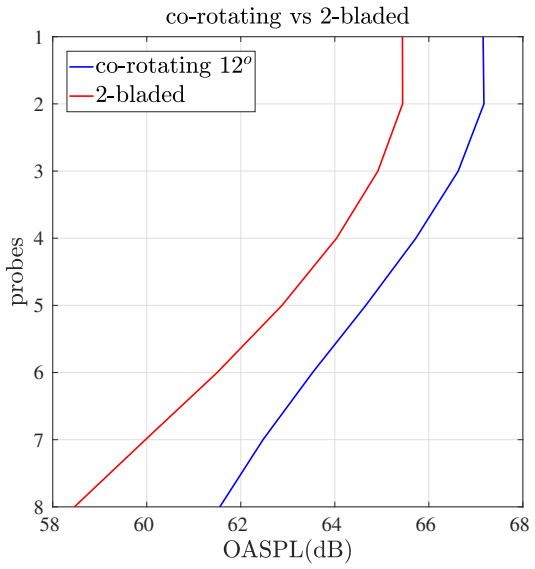

Figure 6.38: OASPL comparison for 90-4000 Hz between 12^o co-rotating and 2-bladed rotor

To investigate the reason for this difference, pressure signal was compared between both the co-rotating and 2-bladed rotor at probe 2 (in-plane probe), wherein upper and lower rotor of the co-rotating rotor was plotted separately too, as shown in Figure 6.39. The pressure fluctuations

from upper and lower rotor adds up to more than the pressure fluctuations from the 2-bladed rotor, the main reason being the smaller azimuthal separation between the former rotors.

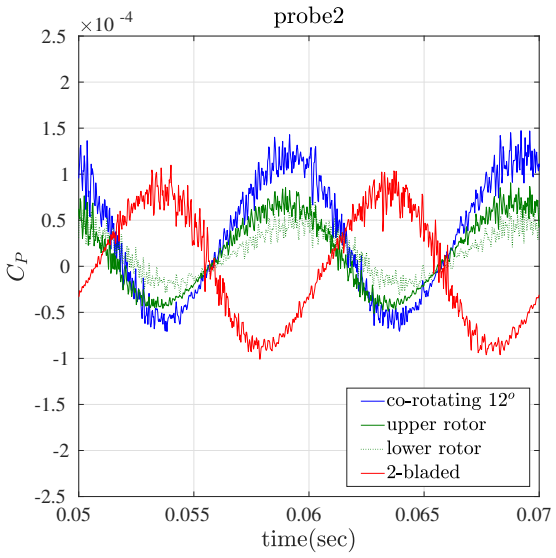

Figure 6.39: Raw pressure signal comparison between co-rotating and 2-bladed rotor

Therefore, a 2-bladed rotor will give *lesser noise* than a 2×2-bladed rotor stacked on top of each other (with a small azimuthal separation) and producing the same thrust. Although, as was previously shown, noise decreases and thrust increases as azimuthal separation is increased for a co-rotating rotor. That being so, a co-rotating rotor with a higher azimuthal separation (close to 80-90^o) will most likely give lesser noise than a 2-bladed rotor producing the same thrust.

6.5. Quantification of flow phenomena

In this section, the flow phenomena in a co-rotating rotor have been quantified based on the thrust results. The purpose is to compare the importance of each phenomenon towards improving the performance of the rotor. A total of 3 major flow phenomena have been found in a co-rotating rotor:

- ***Inflow effect***
- ***Blade-Vortex Interaction (BVI)***
- ***Circulation effect***

A number of assumptions have been taken while quantifying these phenomena, therefore, they do not represent the exact quantity of each but is meant to be a way of comparison of different phenomena. The assumptions taken are:

- There is no *BVI* effect for the upper rotor, therefore, the only effects acting on it are *inflow* and *circulation effect*
- There is no *circulation effect* in case of 84^o azimuthal separation
- The 2-bladed isolated rotor will be taken as the *baseline*, so a rotor marked with 100% performance

- The *inflow effect* is same for both the upper and lower rotor for 84^o case but differs as axial or azimuthal separation is varied; this is valid because the difference in thrust for upper and lower rotor is less for the 84^o case than compared to other cases, thus, difference in inflow effect can be neglected

Table 6.11 and Table 6.12 presents the data for the 84^o and 12^o azimuthal configuration respectively. In case of upper rotor, *circulation effect* greatly enhances the upper rotor performance and counters the *inflow effect*. In case of lower rotor, *BVI* effect is important for higher azimuthal separation but as separation decreases, *inflow effect* starts playing a bigger role and further decreases the lower rotor performance.

	T (N)	**Inflow effect (%)**	**BVI effect (%)**
Upper rotor	7.22	-12.27	0
Lower rotor	5	-12.27	-26.97

Table 6.11: Different effects for 84^o azimuthal (and 1.1 in axial) separation setup - phase I

	T (N)	**Inflow effect (%)**	**BVI effect (%)**	**Circulation Effect (%)**
Upper rotor	8.96	-12.27	0	21.14
Lower rotor	2.74	-39.74	-26.97	0

Table 6.12: Different effects for 12^o azimuthal separation setup - phase II

	T (N)	**Inflow effect (%)**	**BVI effect (%)**
Upper rotor	7.43	-9.72	0
Lower rotor	4.88	-13.73	-26.97

Table 6.13: Different effects for 1.3 in axial separation setup - phase II

Table 6.13 presents the data for the 1.3 in axial configuration. The *inflow effect* for the upper rotor decreases and for the lower rotor increases as axial separation is increased, which was the same conclusion obtained previously in section 6.3.2. The *BVI* effect remains unchanged.

7

Conclusions and Recommendations

7.1. Conclusions

An investigation on co-rotating rotors for the purpose of aerodynamic and aeroacoustic analysis has been performed in this study. Based on the results and analyses in all the phases, various conclusions have been presented in terms of answers to all the research objectives below:

Phase I - Grid Resolution study

- *How much resolution is sufficient enough for an acceptable level of convergence for co-rotating rotor simulations?*

In the resolution study, *Medium* case with 75 million fine equivalent voxels achieved a sufficiently converged result. It was found out that resolving the whole blade surface is important to achieve a good convergence. Resolution of blade surface plays a role in the flow behaviour over the rotor blade and ultimately, the rotor thrust. Trip plays an important role in flow transition and in broadband part of noise, and thus, a special focus must be put on sufficiently resolving it.

- *What is the accuracy of the results achieved when the result for best resolution is compared to reference literature? Is that accuracy acceptable?*

- *What is the reason for difference between computational and experimental results observed?*

The best configuration obtained in the resolution study had a difference of 12.34% from the experimental thrust results. This difference was found constant in all co-rotating rotor configurations and therefore, it can be concluded that there were some aspects of experimental setup which were not being captured in the computational setup. This can be either due to different hub used, confined experimental domain, electric motor used to run the rotor or due to the experimental test stand. Thus, for the present computational setup, the above accuracy was acceptable.

Phase II - Flow Physics study

- *What is the reason for change of performance and acoustic characteristics of the co-rotating rotor when azimuthal separation is varied?*

- *What is the reason for change of performance and acoustic characteristics of the co-rotating rotor when axial separation is varied?*

Three major flow phenomena were found in a co-rotating rotor: *Inflow, Circulation* and *Blade-Vortex Interaction (BVI)* effect. While the first two effects are potential effects, *BVI* effect arises due to finite length of a rotor blade similar to an aircraft wing. *Inflow effect* takes place due to the mutual interaction of streamtubes of the two rotors, which affects the axial velocity and the AoA distribution on the blade. *Circulation effect* is visible in the configuration with lower azimuthal separation. In case when lower rotor is in close vicinity of the upper rotor, the circulation on former increases the circulation on latter, similar in behaviour to a flap. *BVI* effect is due to the interaction of blade tip vortices with both the upper and lower rotor blades. Due to *BVI*, additional velocities are induced on the blades which affects the spanwise thrust distribution, than compared to an ideal case when there would be no tip vortices.

In a co-rotating rotor, upper rotor thrust contribution is more than the lower rotor. This is due to the fact that *upper rotor* is operating in a freestream flow and the tip vortices are situated further downstream of the rotor, compared to an isolated 2-bladed rotor. The *lower rotor*, on the other hand, is operating in the wake of upper rotor and interacting with both the upper and lower rotor tip vortices, which are very close to the rotor blade.

When the *azimuthal separation* is reduced, the circulation effect increases the thrust of the upper rotor to even more than the 2-bladed isolated rotor. As a result, lower rotor thrust reduces due to higher axial velocity induced by the upper rotor. The decrease in lower rotor is more than the increase in upper rotor, thus, overall thrust decreases. Both the rotors act as a coupled system and mutually affect one another. Noise increases for lower azimuthal separation due to lower destructive interference between the sound scattered by upper and lower rotor, as compared to rotors with higher azimuthal separation.

When the *axial separation* is increased, upper rotor thrust increases due to lesser axial velocity induced by the lower rotor streamtube. Since the rotors act as a coupled system, increased upper rotor thrust decreases the lower rotor thrust. Since increase in upper rotor is more than the decrease in lower rotor, overall thrust increases. Noise increases too, for higher axial separation, and this is attributed to the increase in loading noise due to increased thrust value.

Based on the flow phenomena observed, the co-rotating rotor behaviour can be explained when the above-mentioned parameters, and even other geometrical parameters, are varied. This will also help to propose a new configuration with improved thrust and noise characteristics.

- *Can the lower rotor play a role of high lift device, such as flap, when operating very close to the upper rotor?*

The lower rotor was found to be acting like a flap for the upper rotor, increasing its thrust to even more than the 2-bladed isolated rotor, and this was termed as the *circulation effect*. This effect has the potential of improving the performance of co-rotating rotors to even more than found in the present study.

Phase III - Quantification and Baseline study

- *How much is the performance gained or lost by the co-rotating rotor as compared to an isolated 2-bladed rotor?*

- *Is it possible to quantify the difference?*

According to the results obtained, the performance of both the upper and lower rotor is different than an isolated 2-bladed rotor. This was expected since both the rotors mutually interact with each other, affecting the flow experienced by both rotors. In most of the cases, the thrust produced by each rotor decreases, as compared to the isolated rotor, with the lower rotor reduction more than the upper. In case of small azimuthal separation, *circulation effect* increases the thrust produced by the upper rotor to more than the isolated rotor, although lower rotor thrust decreases.

To quantify the difference in performance obtained, it is important to quantify the flow phenomena. This was shown in Section 6.5. The *BVI* effect is an important factor which is responsible for the overall reduction in co-rotating rotor performance, as compared to the isolated rotor. To this end, if a co-rotating rotor design can mitigate the production of tip vortices, performance of the rotor can be increased. In some particular cases (lower azimuthal separation), *inflow effect* is more important for the lower rotor due to the increase in upper rotor thrust value.

- *How much is the difference in noise for a co-rotating rotor as compared to an isolated rotor producing the same thrust?*

The co-rotating rotor with 12^o azimuthal separation was found to produce higher noise by around 2-2.5 dB, than the 2-bladed isolated rotor producing the same thrust. Although, according to the results observed previously, 84^o azimuthal separation can produce lesser noise than the corresponding 2-bladed isolated rotor producing the same thrust.

- *Can a new co-rotating configuration be proposed, which can have improved aerodynamic and aeroacoustic behaviour?*

The lower rotor experiences a different *inflow velocity distribution* than the upper rotor, which adversely affects the AoA on the lower blade especially before 0.8 r/R location. Thus, if the lower rotor blade can be designed such that the AoA is kept the same as the upper rotor, it can improve the overall rotor performance. The inner part of the blade should have *higher twist* than the outer part, even higher than the upper blade. To reduce noise, the improvements should be made on higher azimuthal separation rotors, so that destructive interference plays an important role.

7.2. Recommendations

Finally, there are various recommendations which can be proposed for future studies on co-rotating rotors, either for a high-fidelity or low-fidelity simulations:

- The 12^o configuration should be investigated further by performing a *differential collective pitch* study. The idea is to increase the thrust of the lower rotor which will help to increase the total rotor thrust too, due to *circulation effect*. Since there will be two more adverse effects (*Inflow* and *BVI*) for the rotor, it is possible that *circulation effect* opposes the other two effects and keeps the upper rotor thrust constant, thus, increasing the overall co-rotating rotor thrust.

- *Dual actuator disc theory* should be used in combination with *BEMT* (or another low fidelity model) to perform quicker aerodynamic simulations for a configuration, and then finally perform high-fidelity simulations for accurate aeroacoustic results and validating with an experimental result.

- Investigations should be made at other *rotational speeds* too. According to results from Tinney [37], although the variation in thrust values were similar, the azimuthal separation at which highest thrust value was attained was different for different rotational speeds. Therefore, there is a possibility of additional interactions taking place at other rotational speeds in a co-rotating rotor.

- Simulations should be performed for *azimuthal angles* even higher than 90^o, such that lower rotor is ahead of upper rotor. This will help to understand the decrease of thrust which was observed for angles higher than 90^o by Tinney [37].

- Further investigations should be done for difference between *PowerFLOW* and *experimental* results. A simulation can be performed with similar hub geometry to the experiment, including the motor geometry and using a confined computational domain [27] similar to the experimental test section.
- The *grid resolution study* can be expanded further by changing the spacing between inner VR regions very close to the blade surface. The purpose should be to resolve even better the boundary layer on the surface, and check the difference in thrust produced.
- Investigations should be done with *differential radius* configurations. This will help to avoid BVI in case of lower rotor, ultimately increasing co-rotating rotor performance.
- Rotor blades can be designed with *Prandtl wing* concept, so that tip vortices strength is reduced which results in decrease in BVI and increase in rotor thrust.

A

Appendix

Non-dimensional parameters

Thrust coefficient

$$C_T = \frac{T}{\rho n^2 D^4} \tag{A.1}$$

where, T is thrust produced by the propeller, ρ is fluid density, n is rotations per second and D is propeller diameter.

Torque coefficient

$$C_Q = \frac{Q}{\rho n^2 D^5} \tag{A.2}$$

where, Q is torque provided to the propeller.

Advance Ratio

$$J = \frac{u_0}{nD} \tag{A.3}$$

where, u_0 is flight velocity.

Propeller efficiency

It is defined as:

$$\eta = \frac{T \cdot u_0}{P_{in}} \tag{A.4}$$

It can also be written as:

$$\eta = \frac{T u_0}{P_{in}} = \frac{T u_0}{2\pi n Q} = \frac{1}{2\pi}\frac{C_T}{C_Q} J \tag{A.5}$$

Figure of Merit

$$FOM = \frac{(T_u^{3/2} + T_l^{3/2})\sqrt{2\rho A}}{P_{in}} \tag{A.6}$$

where, T_u and T_l is thrust generated by upper and lower rotor respectively, A is propeller swept area, and P_{in}=P_u+P_l where, P_u and P_l is power input to upper and lower rotor respectively.

Non-dimensional vorticity

$$\text{Vorticity [-]} = \frac{\omega}{n} \tag{A.7}$$

where, ω is the vorticity at a point in the flowfield.

Non-dimensional velocity

$$\text{Velocity [-]} = \frac{v \cdot n}{D} \tag{A.8}$$

where, v is the velocity at a point in the flowfield.

Coefficient of pressure

$$C_P = \frac{P - P_{ref}}{\frac{1}{2} \cdot \rho \cdot v^2} \tag{A.9}$$

where, P_{ref} is the reference pressure (taken as standard atmospheric pressure in this study) and v is the velocity experienced at $0.54R$ spanwise position on the rotor blade.

B

Appendix

Miscellaneous results

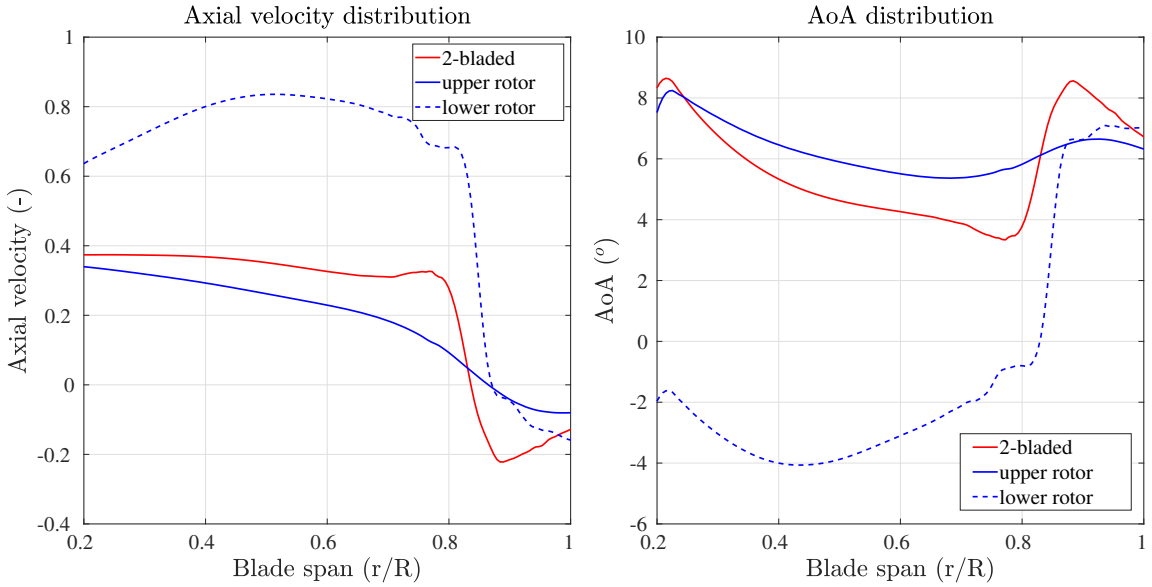

(a) (b)

Figure B.1: Comparison of 12° co-rotating rotor with the baseline rotor

C_P plot

Pressure coefficient (C_P) was plotted at 3 different spanwise locations. For non-dimensionalizing pressure, tangential velocity (ωr) at 0.54R was taken for all pressure values at all locations so that C_P values represent dimensional values when comparing different plots.

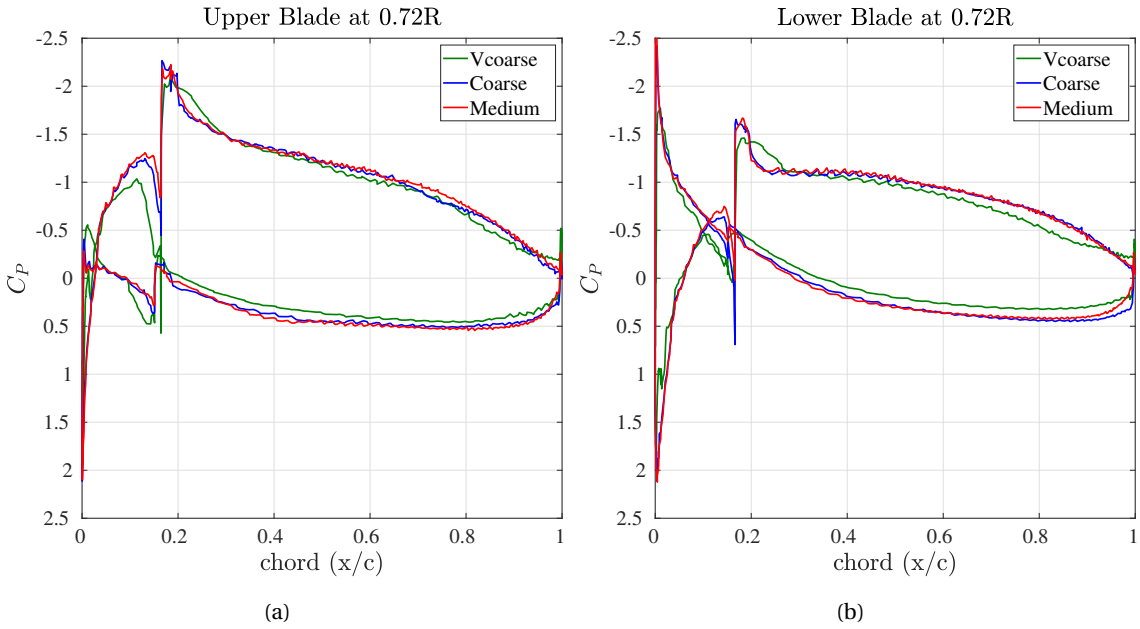

Figure B.2: Resolution study on C_P plots for 84^o and 1.1 in (Phase I) configuration

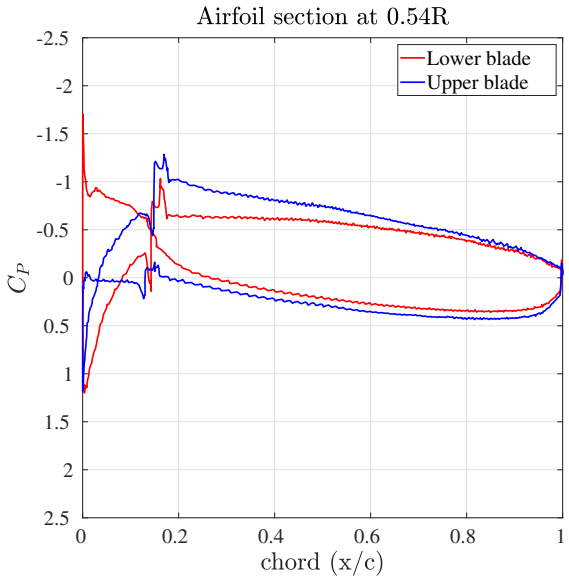

Figure B.3: C_P comparison between upper and lower rotor for 84^o and 1.1 in (Phase I) configuration

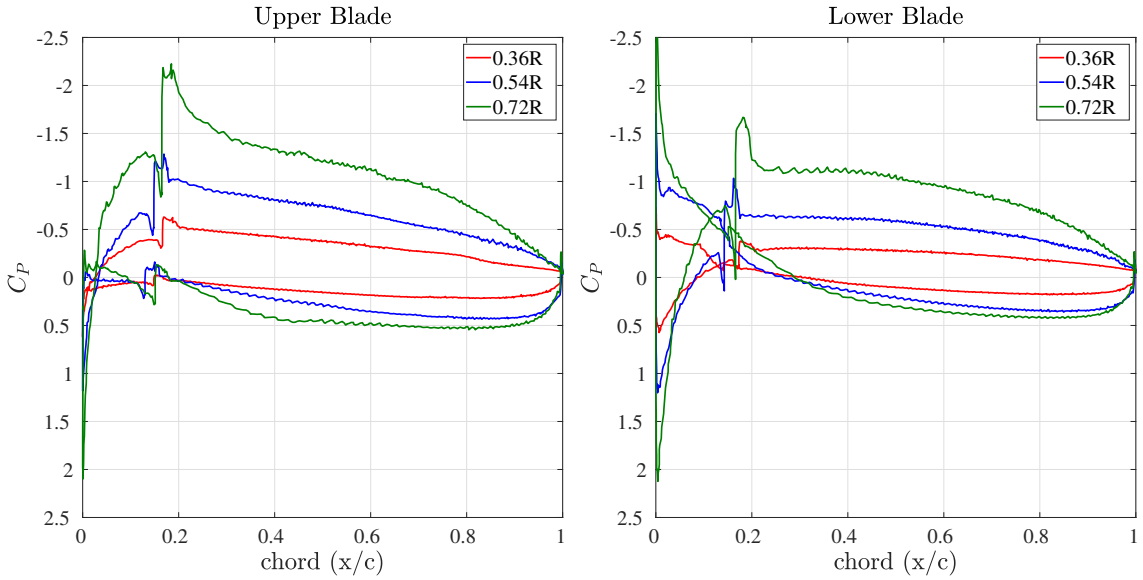

(a) (b)

Figure B.4: C_P comparison for different spanwise locations 84^o and 1.1 in (Phase I) configuration

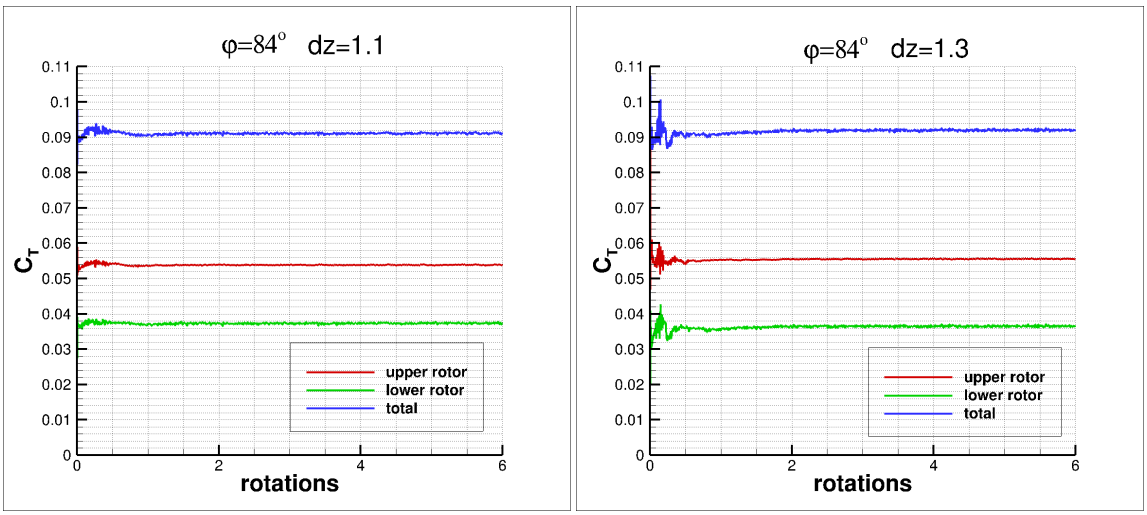

(a) 1.1in (b) 1.3in

Figure B.5: Individual rotor thrust performance for axial variation

Collective pitch of lower rotor	0^o	2.5^o	5^o
Total thrust (N)	11.69	14	16.32
Upper rotor thrust (N)	8.95	8.95	9.03
Lower rotor thrust (N)	2.74	5.05	7.29
2-bladed rotor thrust (N)	8.23	-	-

Table B.1: Thrust variation of 12^o co-rotating configuration when lower rotor collective pitch is varied

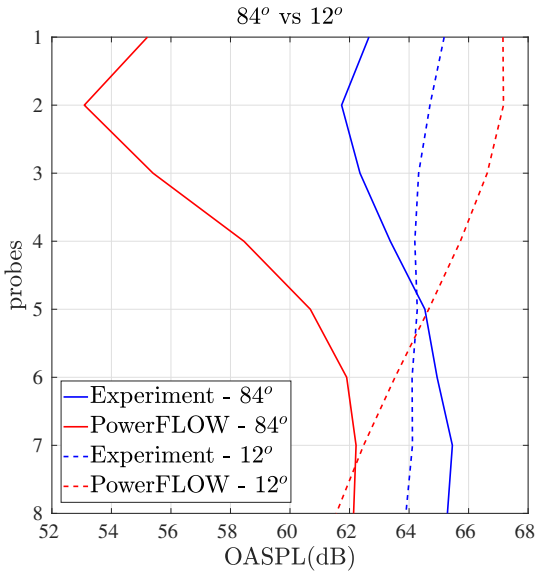

Figure B.6: OASPL comparison for 90-4000 Hz for 84^o and 12^o between PowerFLOW and experiment

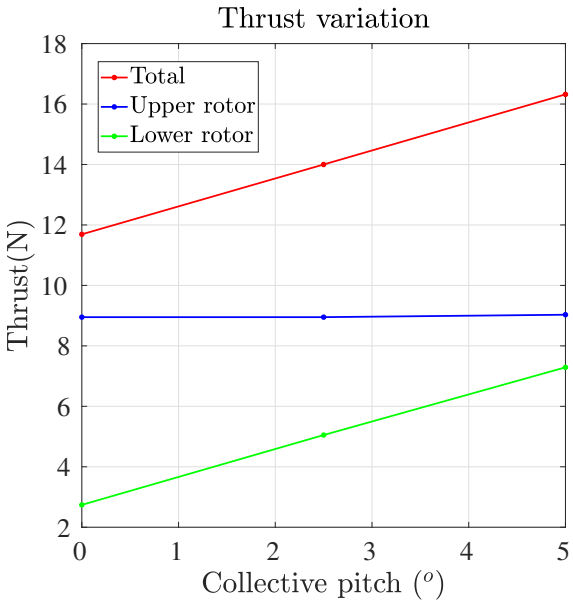

Figure B.7: Thrust variation of 12^o co-rotating configuration when lower rotor collective pitch is varied

Bibliography

[1] Luca Anselmi. Computational analysis of ducted wind turbines noise. 2017.

[2] Jeremy Bain and Chris Hennes. Computational investigation of small axial stacked rotors for dramatic noise reduction. In *11th AIAA Aviation Technology, Integration, and Operations (ATIO) Conference, including the AIAA Balloon Systems Conference and 19th AIAA Lighter-Than*, page 6981, 2011.

[3] Yuanxun Bill Bao and Justin Meskas. Lattice boltzmann method for fluid simulations. *Department of Mathematics, Courant Institute of Mathematical Sciences, New York University, New York*, 2011.

[4] Romana Begum and M Abdul Basit. Lattice boltzmann method and its applications to fluid flow problems. *European Journal of Scientific Research*, 22(2):216–231, 2008.

[5] Mahendra Bhagwat. Co-rotating and counter-rotating coaxial rotor performance. *AHS Aeromechanics Design for Transformative Vertical Flight*, 2018.

[6] Jérôme Boudet, J-F Monier, and Feng Gao. Implementation of a roughness element to trip transition in large-eddy simulation. *Journal of Thermal Science*, 24(1):30–36, 2015.

[7] Kenneth S Brentner and Feridoun Farassat. Modeling aerodynamically generated sound of helicopter rotors. *Progress in Aerospace Sciences*, 39(2-3):83–120, 2003.

[8] Guillaume Brès, Franck Pérot, and David Freed. Properties of the lattice boltzmann method for acoustics. In *15th AIAA/CEAS Aeroacoustics Conference (30th AIAA Aeroacoustics Conference)*, page 3395, 2009.

[9] Damiano Casalino. An advanced time approach for acoustic analogy predictions. *Journal of Sound and Vibration*, 261(4):583–612, 2003.

[10] Damiano Casalino, André FP Ribeiro, and Ehab Fares. Facing rim cavities fluctuation modes. *Journal of Sound and Vibration*, 333(13):2812–2830, 2014.

[11] Shiyi Chen and Gary D Doolen. Lattice boltzmann method for fluid flows. *Annual review of fluid mechanics*, 30(1):329–364, 1998.

[12] N Curle. The influence of solid boundaries upon aerodynamic sound. *Proceedings of the Royal Society of London. Series A. Mathematical and Physical Sciences*, 231(1187):505–514, 1955.

[13] Paolo Di Francescantonio. A new boundary integral formulation for the prediction of sound radiation. *Journal of Sound and Vibration*, 202(4):491–509, 1997.

[14] Fereidoun Farassat and George P Succi. The prediction of helicopter rotor discrete frequency noise. In *In: American Helicopter Society, Annual Forum, 38th, Anaheim, CA, May 4-7, 1982, Proceedings.(A82-40505 20-01) Washington, DC, American Helicopter Society, 1982, p. 497-507.*, pages 497–507, 1982.

[15] John E Ffowcs Williams and David L Hawkings. Sound generation by turbulence and surfaces in arbitrary motion. *Philosophical Transactions of the Royal Society of London. Series A, Mathematical and Physical Sciences*, 264(1151):321–342, 1969.

[16] APC Slow Flyer. Available online: https://www. apcprop. com/articles. asp.

[17] Stewart Glegg and William Devenport. *Aeroacoustics of low Mach number flows: fundamentals, analysis, and measurement*. Academic Press, 2017.

[18] Frank Hitchens. *Propeller aerodynamics: the history, aerodynamics & operation of aircraft propellers*. Andrews UK Limited, 2015.

[19] Andrew Knesnik. *Feasibility Study of an Axially-Stacked, Subsonic Propeller System*. PhD thesis, University of Cincinnati, 2012.

[20] Anton J Landgrebe and E Dean Bellinger. Experimental investigation of model variable-geometry and ogee tip rotors.[aerodynamic characteristics of variable geometry rotary wings]. 1974.

[21] Gordon J Leishman. *Principles of helicopter aerodynamics with CD extra*. Cambridge university press, 2006.

[22] Michael James Lighthill. On sound generated aerodynamically i. general theory. *Proceedings of the Royal Society of London. Series A. Mathematical and Physical Sciences*, 211(1107):564–587, 1952.

[23] Michael James Lighthill. On sound generated aerodynamically ii. turbulence as a source of sound. *Proceedings of the Royal Society of London. Series A. Mathematical and Physical Sciences*, 222(1148):1–32, 1954.

[24] Jack E Made and Donald W Kurtz. A review of aerodynamic noise from propellers rotors and lift fans. *NASA Technical Report 32-7462*, 1970.

[25] Simon Marié, Denis Ricot, and Pierre Sagaut. Comparison between lattice boltzmann method and navier–stokes high order schemes for computational aeroacoustics. *Journal of Computational Physics*, 228(4):1056–1070, 2009.

[26] Renwei Mei, Wei Shyy, Dazhi Yu, and Li-Shi Luo. Force evaluation in the lattice boltzmann method. In *APS Division of Fluid Dynamics Meeting Abstracts*, 1999.

[27] Clément Nardari, Damiano Casalino, Francesco Polidoro, Vedran Coralic, Phoi-Tack Lew, and John Brodie. Numerical and experimental investigation of flow confinement effects on uav rotor noise. In *25th AIAA/CEAS Aeroacoustics Conference*, page 2497, 2019.

[28] Schuyler R Nichols. *Experimental Approach to the Feasibility of an Axially-Stacked Propeller System*. PhD thesis, University of Cincinnati, 2014.

[29] AM O. Smith. High-lift aerodynamics. *Journal of Aircraft*, 12(6):501–530, 1975.

[30] CFD Online. *https://www.cfd-online.com/Wiki/Y_plus_wall_distance_estimation*.

[31] Manikandan Ramasamy. Hover performance measurements toward understanding aerodynamic interference in coaxial, tandem, and tilt rotors. *Journal of the American Helicopter Society*, 60(3):1–17, 2015.

[32] James B Rorke. Hover performance tests of full scale variable geometry rotors. 1976.

[33] Thomas Rossing. *Springer handbook of acoustics*. Springer Science & Business Media, 2007.

[34] Sauro Succi. *The lattice Boltzmann equation: for fluid dynamics and beyond*. Oxford university press, 2001.

[35] Dassault Systèmes. *SIMULIA PowerCASE User's Guide*. 6-2019.

[36] Dassault Systèmes. *SIMULIA PowerFLOW User's Guide*. 6-2019.

[37] Charles E Tinney and John Valdez. Thrust and acoustic performance of small-scale, coaxial, corotating rotors in hover. *AIAA Journal*, pages 1–11, 2019.

[38] Daiju Uehara and Jayant Sirohi. Quantification of swirl recovery in a coaxial rotor system. In *Proceedings of the 73rd Annual Forum*, 2017.

[39] Wouter CP van der Velden. Computational aeroacoustic approaches for wind turbine blade noise prediction. 2017.

[40] Siena Whiteside, Nikolas Zawodny, Xiaofan Fei, Nicole A Pettingill, Michael D Patterson, and Paul Rothhaar. An exploration of the performance and acoustic characteristics of uav-scale stacked rotor configurations. In *AIAA Scitech 2019 Forum*, page 1071, 2019.

[41] Qisu Zou and Xiaoyi He. On pressure and velocity boundary conditions for the lattice boltzmann bgk model. *Physics of fluids*, 9(6):1591–1598, 1997.